ABSTRACT

Title of Dissertation:	PHENOMENOLOGY OF ULTRALIGHT FIELDS
	Dawid Brzeminski Doctor of Philosophy, 2024
Dissertation Directed by:	Professor Anson Hook Department of Physics

Standard Model is an amazing success of particle physics, a success further cemented by the discovery of the Higgs boson. While its picture is incredibly satisfying, there are still a few mysteries it cannot address, one of which is the nature of dark matter. While we have overwhelming evidence for its existence, we still do not know its basic properties such as mass or spin. Ultralight fields are among the most exciting dark matter candidates. Their large occupation number allows us to treat them as classical fields, while their non-relativistic velocities ensure that the field oscillates at an angular frequency equal to its mass with a long coherence time. In this dissertation, we discuss some challenges associated with constructing successful models of ultralight dark matter and discuss new detection strategies.

In the first part of this dissertation, we address the underlying issue with ultralight scalars, namely the naturalness problem. Generally, requiring the scalar to couple to the Standard Model introduces radiative corrections to its mass, which conflicts with the requirement of a small mass. We present an ultraviolet-complete model that avoids this issue by employing Z_N symmetry,

which suppresses corrections to the mass while retaining relatively large couplings to photons, making the model testable by current and future experiments looking for the time-variation of the fine structure constant.

In the second part of this dissertation, we focus on the experimental aspects of ultralight scalars. The general experimental landscape is divided into two categories: experiments assuming a dark matter background, and experiments measuring the fifth force associated with the new scalar. The former provides strong constraints for the lightest scalars due to their large abundance, while the latter provides more conservative but robust limits on scalar interactions across many decades in scalar mass. We propose a novel approach based on measuring scalar potential using atomic and nuclear clocks, which complements fifth force measurements and offers significant improvements over current bounds.

In the third part of the dissertation, we shift our attention to vector dark matter. Specifically, we consider a scenario where some of the lepton generations are charged under a new gauge field. In this case, neutrino decays in the early universe impose strong constraints on their couplings, particularly for the lightest vectors. At higher masses, neutrino oscillations become a leading constraint due to the sourcing of the field by electrons affecting their oscillations. We demonstrate that in the presence of vector dark matter, the influence of the background field on neutrinos is even more pronounced, significantly enhancing constraints on the lightest vectors by several orders of magnitude.

PHENOMENOLOGY OF ULTRALIGHT FIELDS

by

Dawid Brzeminski

Dissertation submitted to the Faculty of the Graduate School of the
University of Maryland, College Park in partial fulfillment
of the requirements for the degree of
Doctor of Philosophy
2024

Advisory Committee:
Professor Anson Hook, Chair/Advisor
Professor Zackaria Chacko
Professor Raman Sundrum
Professor Peter Shawhan
Professor Richard Wentworth

Dedication

To Aneta, Bernardyna and Piotr.

Acknowledgments

First of all, I would like to thank my advisor, Anson Hook. It has been a privilege to be his student and learn from him. Witnessing his breadth of physics knowledge, combined with his superpower to transform complex problems into textbook ones, has been truly inspiring.

Physics is a group effort, and this journey would have been bland without my collaborators. I want to thank Zackaria Chacko for his insightful comments and guidance. Also, I would like to thank Junwu Huang, Gustavo Marques-Tavares, Abhishek Banerjee, Saurav Das, Abhish Dev, Ina Flood, and Clayton Ristow.

Over the years, I have seen time and time again how special the Maryland Center for Fundamental Physics is. I am incredibly grateful to be part of this family and would like to thank all the members for creating such a friendly and supportive environment.

I want to thank current and past MCFP members, including Raman Sundrum, Kaustubh Agashe, Tom Cohen, postdocs Manuel Buen-Abad, Jae Hyeok Chang, Zhen Liu, Lorenzo Ricci, Yuhsin Tsai, and students Sagar Airen, Arushi Bodas, Ed Broadberry, Kaustubh Deshpande, Sanket Doshi, Reza Ebadi, Majid Ekhterachian, Saurabh Kadam, Soubhik Kumar, Deepak Sathayan, and Jeremy Shuler. Last but not least, I would like to thank Melanie Cline, who was an instrumental figure at MCFP.

I also would like to thank Peter Shawhan and Richard Wentworth for agreeing to be part of my dissertation committee and committing their time to study my dissertation.

I want to thank the Physics administrators, Josiland Chambers, Jessica Crosby, and Donna Hammer, who ensured that my PhD experience was very smooth.

Most importantly, it is difficult to give justice to how much I owe to my soulmate, Aneta, and my parents, Bernardyna and Piotr. My life would be boring without them. Their love and support have kept me sane through the highs and lows of my PhD.

Table of Contents

List of Tables

List of Figures

Chapter 1: Introduction

1.1 Motivation

Particle physics has reached an interesting point in its history. On the one hand, with the discovery of the Higgs boson [29, 30], we have completed the Standard Model puzzle, achieving a consistent description of experimentally measured phenomena up to energies on the order of TeV. On the other hand, there are indications that this picture is incomplete. For example, the Standard Model does not account for the fact that neutrinos have mass. Additionally, baryons constitute only 5% of the universe's energy budget, while Dark Matter (DM) is more than five times more abundant [31]. The Standard Model also lacks a symmetry that would protect the mass of the Higgs boson from radiative corrections, leading to the unresolved hierarchy problem. Furthermore, CP-violation in the strong sector appears to be finely tuned to a value close to zero.

Addressing all of these problems simultaneously poses a great challenge, and it is likely that the answers require multiple ingredients. The QCD axion is an example of a modest approach, as it attempts to explain the Strong CP problem and can even account for dark matter in some instances. It arises as a pseudo-Goldstone boson of the broken global $U(1)_{PQ}$ symmetry, effectively replacing the QCD θ angle,

$$\frac{\theta}{32\pi^2}G\tilde{G} \quad \rightarrow \quad \frac{a}{32\pi^2 f}G\tilde{G}. \tag{1.1}$$

Here, f is the decay constant of axion a. The minimum of its potential lies at $a = 0$, which does not break CP. However, after $U(1)_{PQ}$ breaking, the expectation is that $a \sim f$, which is far from the current bound $a/f \lesssim 10^{-10}$. Its value is dynamically tuned close to $a = 0$ as the field starts oscillating around the QCD phase transition when its mass is generated. The amplitude of these oscillations dilutes away due to Hubble friction, explaining why a/f is so small today. Interestingly, if the mass of the axion is $m_a \sim 10^{-5}$ eV[1], it would not only solve the Strong CP puzzle but could also naturally constitute the majority of dark matter [32].

1.2 Ultralight Dark Matter and its properties

This mass falls into an exciting regime named ultralight dark matter (ULDM). To understand its significance, let us compare the volume occupied by a wave packet of a single DM particle, $V_{\rm DM} = \lambda_{\rm dB}^3 = \left(\frac{2\pi}{m_{\rm DM} v_{\rm DM}}\right)^3$, to its number density $n_{\rm DM} = \frac{\rho_{\rm DM}}{m_{\rm DM}}$ in our galaxy,

$$V_{\rm DM} n_{\rm DM} \sim 1 \left(\frac{30 \text{ eV}}{m_{\rm DM}}\right)^4 . \tag{1.2}$$

Therefore, if DM has a mass $m \lesssim 10$ eV, the wave packets of DM particles overlap, and the field can be treated as classical. Such a scenario can only be realized by bosons, as fermions are limited by the Pauli exclusion principle.

The most popular way to produce axions or other scalar fields is to treat them as pseudo-Goldstone bosons of a $U(1)$ global symmetry that undergoes spontaneous breaking at some high scale f. Depending on whether the $U(1)$ breaking occurs after or before inflation, we observe two distinct types of field evolution. In the first scenario, large spatial fluctuations lead to the

[1]Throughout this dissertation, we use natural units, where $\hbar = c = 1$.

formation of topological defects, necessitating numerical simulations to understand the cosmological history of the field. The second scenario, known as the misalignment mechanism [33], is qualitatively simpler: scalar fluctuations are homogenized over superhorizon scales, and the field gets a random value $\phi \sim f$. Its evolution is then described by the following equation of motion

$$\ddot{\phi}(t) + 3H\dot{\phi}(t) + V'(\phi(t)) = 0. \tag{1.3}$$

The damping term $3H\dot{\phi}(t)$ is called Hubble friction. In the typical scenario, where $V''(\phi(t)) \ll H^2$ after the reheating, the field value is "frozen" until $V''(\phi(t)) \gtrsim H^2$. Provided that there are no sudden changes in the mass m_ϕ, i.e. the WKB approximation holds $m_\phi^2 \gg \dot{m}_\phi$, the field amplitude evolves so that the adiabatic invariant $n_\phi a^3 = m_\phi \phi^2 a^3 = \text{const}$ does not change with the scale factor a. Eventually, if the field is DM it reaches the amplitude $\phi_0 = \sqrt{\rho_\phi}/m_\phi$ that is consistent with the current energy density of dark matter ρ_ϕ.

While the QCD axion is a well-motivated example of ULDM, it is not the only possibility. Moduli are another class of exciting dark matter candidates [34–38], which can also be produced via the misalignment mechanism. They are typically present in ultraviolet-complete theories such as string theory, where they control the fundamental constants via their vacuum expectation values. Specifically, in the low-energy effective theory, we expect such couplings to look like [39, 40]

$$\mathcal{L} \supset \kappa\phi\Big[\frac{d_e}{4e^2}F_{\mu\nu}F^{\mu\nu} - \frac{d_g\beta_3}{2g_3}G^A_{\mu\nu}G^{A\mu\nu} - d_{m_e}m_e\bar{\psi}_e\psi_e - \sum_{i=u,d}(d_{m_i} + \gamma_{m_i}d_g)m_i\bar{\psi}_i\psi_i\Big] \quad . \tag{1.4}$$

Here, $\kappa = \sqrt{4\pi G}$, where G is Newton's constant, e represents the charge of the electron,

g_3 is the coupling constant of quantum chromodynamics (QCD), and $\beta_3 \equiv \partial g_3/\partial \log \mu$ is its beta function. The parameters m_i denote the masses of the fermions and $\gamma_m \equiv -\partial \log m/\partial \log \mu$. The parameters d_x with $x \in \{e, g, m_i\}$ represent the couplings of the scalar to the corresponding gauge bosons and fermions.

For such a DM candidate to be experimentally accessible, these couplings need to be strong enough to produce a significant signal. However, this inevitably leads to radiative corrections that increase the mass of the scalar. Conversely, the period of the signal, inversely proportional to the mass, needs to be sufficiently long to avoid being averaged out. These two requirements are inherently in tension, giving rise to the naturalness problem. To address the naturalness problem, we need to ensure that the couplings and mass required from the dark matter candidate are self-consistent.

To highlight the severity of the challenge, let us consider the correction to the scalar mass coming from its interaction with photons, i.e., $d_e \neq 0$. The leading correction to the mass of the scalar occurs at the two-loop level

$$\delta m^2 \sim \frac{e^2 d_e^2 \kappa^2}{\left(16\pi^2\right)^2} \Lambda^4 \tag{1.5}$$

where Λ is a UV cutoff. As an example, let us consider a scalar of mass $m = 10^{-18}\,\mathrm{eV}$. Current constraints on its coupling to photons require $d_e \lesssim 10^{-3}$. Then, the correction to its mass from the loops involving top quarks yields $\delta m \sim 10^{-11}\,\mathrm{eV}$. We see that $\delta m \gg m$, which requires some spectacular cancellation to ensure consistency in these assumptions. In Chapter 2, which is based on [41], we discuss a model of an ultralight modulus that achieves such cancellation by incorporating Z_n symmetry.

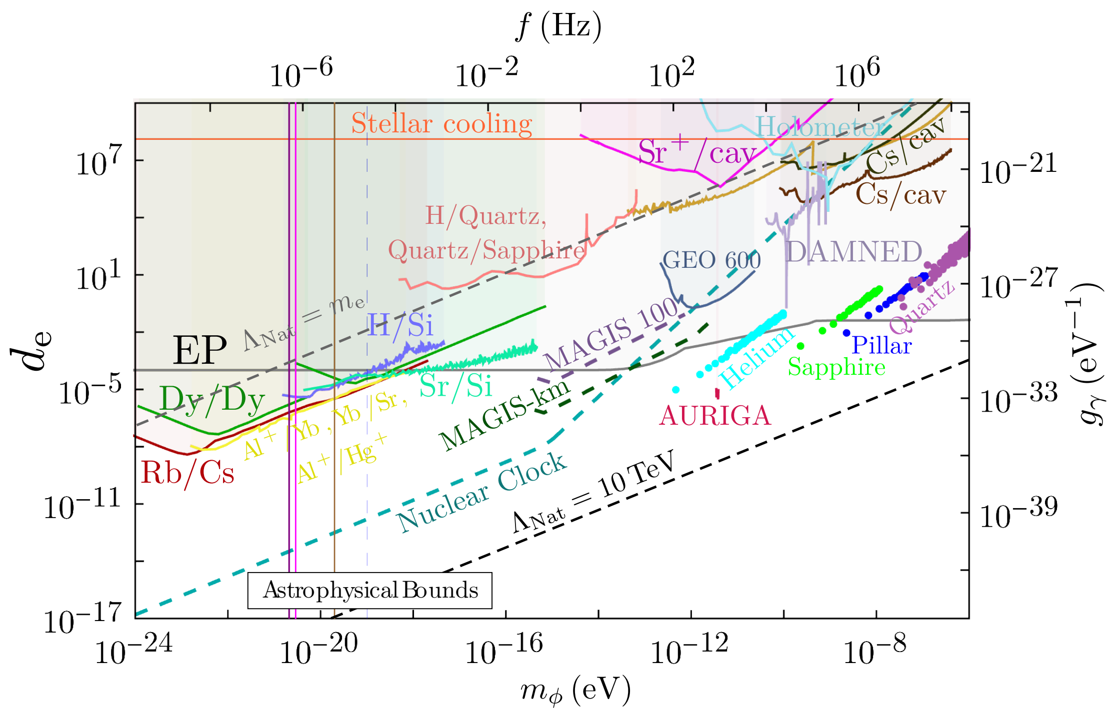

Figure 1.1: Landscape of current and proposed experiments probing the coupling of the scalar to photons d_e. The figure is adapted from [1].

1.3 Experimental landscape

ULDM has a rich phenomenology, which has led to significant interest in detecting such fields, as shown in Fig. 1.1 and discussed in various references [39,40,42–77]. Two main avenues to look for these fields include searching for time- or spatially-varying observables related to their DM background or looking for a new force mediated by them.

The first approach relies on the fact that ULDM is non-relativistic. As the local DM field has an average velocity of $v \sim 10^{-3}$, its frequency band is very narrow, $\Delta\omega/\omega = \Delta E/E = v^2/2 \sim 10^{-6}$. This means that, to a good approximation, the field oscillates at an angular frequency equal to its mass, $\phi(t) = \phi_0 \cos(m_{\rm DM} t)$. The narrow band also means that the signal has a long coherence time $t_{\rm coh} \sim (mv^2)^{-1} = 10^6 m^{-1}$, allowing us to observe the signal for about 10^6 periods before its amplitude and phase randomly change.

In the case of moduli DM with couplings to the SM as described in Eq.(1.4), the signature is the oscillation of fundamental parameters, such as the fine structure constant, and the masses of baryons, electrons, and light quarks. Assuming the scalar saturates the energy budget of DM, $\phi_0 = \sqrt{\rho_{\rm DM}}/m_{\rm DM}$, the bound is set on the coupling d_x. A successful measurement of the time variation of these parameters requires that the mass of the DM is small enough that the effect is not averaged away.

One of the most exciting ways to detect such changes in parameters involves using atomic clocks, which are ideal devices for this task. The main principle is to tune a laser to a specific atomic transition and use this frequency as a unit of time. The change in fundamental parameters due to the oscillation of the scalar field will affect the transition frequency of the atom. However, different transitions generally have different sensitivities to variations in fundamental parameters. Therefore, by comparing two clocks based on different transitions and periodically re-calibrating them, it is possible to look for variations due to DM oscillation.

The main limitation of this approach is its reliance on being in the DM background of the scalar field. The second approach takes advantage of the fact that the couplings in Eq. (1.4) give rise to a new force with a range $\lambda_\phi = 1/m_\phi$, which generally depends on the chemical composition of the test masses.

The standard way to look for such forces is by comparing the accelerations of two bodies of different compositions towards a third body that sources the gravitational field. Different realizations of this type of experiment include: suspended masses in the laboratory [11,13,26,78], free-falling objects in the field of the earth [2,12], the moon and earth in the gravitational field of the sun [79,80], gravitationally bound systems composed of three celestial bodies [81,82], and free falling atoms [83–87].

In Chapter 3, based on [88], we present an alternative way to search for the fifth force, which relies on measuring its potential rather than acceleration. This method is feasible because a macroscopic body can source the scalar field, making the scalar value proportional to the gravitational potential. Consequently, this results in a spatial dependence of fundamental parameters that varies with the distance from the source.

The simplest realization of this approach involves measuring seasonal changes in the fundamental parameters due to the eccentricity of the earth's orbit around the sun. We show that atomic and nuclear clocks can be successfully used to detect a fifth force using this strategy.

1.4 Vector dark matter and neutrino oscillations

While we have primarily focused on scalar fields, Vector Dark Matter (VDM) presents another intriguing possibility for ULDM, offering interesting phenomenology [89–91]. The same argument applies to their oscillation frequency and the coherence time of the signal they produce. The main differentiating factor between these types of fields is the polarization of vector fields. Similar to the amplitude, the polarization remains unchanged over the timescale of $t_{\rm coh}$. Thus, for coherence times longer than a day, there is a preferred direction that experiments could investigate. In the Earth's frame, as the Earth rotates on its axis, this vector rotates with a period of one day, introducing an additional modulation to the measured signal.

Examples of interactions with the Standard Model include photon-dark photon kinetic mixing or gauging anomaly-free symmetries, such as $B-L$, L_e-L_μ, $L_\mu-L_\tau$, or their linear combinations [28, 59, 92, 93]. For instance, the existence of $B-L$ dark photons would result in all atoms being charged under this mediator. Consequently, a new force would arise between all atoms with a range $\lambda_A = 1/m_A$, where m_A is the gauge boson's mass. If this field constituted the majority of dark matter, its background would generate a driving force in the direction of the polarization, a signal detectable by gravitational wave experiments.

Another interesting possibility is related to $L_e - L_\mu$ and $L_\mu - L_\tau$ dark photons. These, in turn, couple only to certain generations of leptons. As $L_e - L_\mu$ couples to electrons, it couples to atoms in the same way as $B - L$ and thus is subject to the same constraints. However, $L_e - L_\mu$ also couples to neutrinos, which opens new ways to test these gauge bosons. For instance, they would allow neutrinos to decay, which sets strong limits [20].

Another consequence is that any $L_e - L_\mu$ or $L_\mu - L_\tau$ dark photon background affects neutrino mass eigenstates and imprints itself on neutrino oscillations. This leads to a correction to the potential of the order $g\vec{v} \cdot \vec{A}_d$. As the neutrino mass eigenstates are sensitive to changes in the potential of the order $\Delta m_\nu^2/E_\nu$, the effect of the background becomes stronger as neutrinos are more energetic, making atmospheric neutrinos most sensitive to this signal. Since $L_e - L_\mu$ is already sourced by electrons, even this contribution is strong enough to place leading constraints in some regions of the parameter space [22, 23].

In Chapter 4, which is based on [94], we consider a similar effect but caused by a DM background. As $A_d \sim \sqrt{\rho_{\rm DM}}/m_A$, the bound gets stronger with a lower mass of the dark photon, significantly improving existing bounds.

Chapter 2: A Time-Varying Fine Structure Constant from Naturally Ultralight Dark Matter

2.1 Introduction

In this chapter, we present a framework in which the modulus that controls the fine structure constant can naturally remain ultralight while constituting all of the observed dark matter in the universe. In order to make the modulus naturally light, we employ the mechanism proposed in Ref. [95]. Accordingly, we introduce N copies of the SM, where N is a number of order a few. If the same modulus controls the fundamental parameters of all the N copies of the SM while nonlinearly realizing the $\mathbb{Z}_N$ symmetry, then the sum of the contributions to the potential of the modulus from each of the copies of the SM cancels to a very high degree of accuracy. The end result is then a modulus with a parametrically smaller mass than naively expected.

A very attractive feature of this framework is that, for certain ranges of the modulus mass and couplings, the misalignment mechanism naturally allows the modulus to constitute all of the observed dark matter. For a given mass and couplings of the modulus, we can determine the thermal corrections to its potential in the early universe. The simplest region of parameter space is that in which the Hubble friction holds the modulus in place and oscillations only begin after thermal effects have become subdominant to the zero temperature potential. Even in this most simple of scenarios, there exists a vast region of parameter space in which the modulus can constitute all of dark matter. In general, finite temperature effects can drastically alter the behavior of the modulus at early times. They can act either to reduce or increase the abundance of dark matter by relaxing the modulus to the minimum or maximum of its potential at high temperatures. Including these effects expands the region of parameter space in which the modulus can play the role of dark matter.

Prospects for probing the time variation of fundamental constants due to ultralight scalars are very promising [10,46,55,96]. In fact, existing data from experiments [2–6,97–99] is already sufficient to place constraints on the scenario we propose in the mass range 10^{-22}eV < m_ϕ < 10^{-5}eV. These limits can be significantly improved in the future by increasing the integration times in the optical-optical clocks and ultimately by taking advantage of the anticipated ^{229}Th nuclear-optical clock [10,100]. Further advancements can be achieved with the recently proposed earth and space based atomic gravitational wave detectors, which will rely on atom interferometry [7–9, 96]. The MAGIS and AION experiments [8, 9] will be earth based interferometers that are planned to gradually increase in size to finally reach a length of 1 km. MAGIS is currently building a 100 m interferometer [9], which should be able to probe the proposed model in the 10^{-16}eV < m_ϕ < 10^{-14}eV mass range. The 1 km stage should increase this range to 10^{-16}eV $\lesssim$ $m_\phi \lesssim 10^{-12}$eV. Once built, the AION experiment will be able to improve the bounds set by MAGIS at both the 100 m and 1 km scale for the same range of masses m_ϕ. The AEDGE experiment [7] is a proposed continuation of the AION experiment that will take advantage of satellites in order to increase the scale of the detector to thousands of kilometers. While it is a very distant prospect, it will have greatly improved sensitivity for masses in the range, 10^{-19}eV < m_ϕ < 10^{-13}eV.

The outline of this chapter is as follows. In Sec. 2.2, we discuss the framework and explain the mechanism that protects the mass of the ultralight modulus. In Sec. 2.3, we study the cosmological history of this class of models and show that the misalignment mechanism can allow the modulus to constitute all of the observed cold dark matter. In Sec. 2.4 we present our results. We determine the current bounds on this class of models and outline the region of parameter space that will be explored by current and future experiments. We conclude in Sec. 2.5

2.2 The Framework

In this section we construct a class of models in which the fine structure constant oscillates in time, and which are free of naturalness problems. We consider a complex scalar Φ that is charged under an approximate *global* U(1) symmetry. This field is assumed to acquire a vacuum expectation value, spontaneously breaking the global symmetry at a scale denoted by f. It is convenient to employ an exponential parametrization of Φ,

$$\Phi = \left(\frac{f+\rho}{\sqrt{2}}\right)\exp\left\{\frac{i\varphi}{f}\right\}. \tag{2.1}$$

Here ρ represents the radial mode in the potential for the scalar field after symmetry breaking, while φ denotes the pseudo-Nambu-Goldstone boson. We write $\varphi = \varphi_0 + \phi$, where φ_0 is the vacuum expectation value (VEV) of φ while ϕ represents the fluctuation about this expectation value. The field ϕ is assumed to couple to the electromagnetic field strength as shown in Eq. (1.4). Although this interaction is nonrenormalizable, it can be generated by coupling Φ to some heavy charged fermions that are integrated out. As a consequence of this coupling, changes in the background value of φ will cause variations in the fine structure constant. However, this coupling violates the U(1) global symmetry explicitly. We therefore expect that, in general, it will generate a potential for φ, leading to a quadratically divergent mass. Since the parameter d_e controls both the amplitude of the modulation as well as the magnitude of the potential, we require some mechanism that protects the potential against large radiative corrections while still admitting an observable signal. As we now explain, this can be done by employing a discrete $\mathbb{Z}_N$ symmetry under which the pseudo-Nambu-Goldstone boson φ transforms nonlinearly [95].

We introduce N copies of the SM, each with its own matter content and gauge groups. We label each of these different copies by an index i, where i runs from 1 to N. The N copies of the SM are related by a discrete $\mathbb{Z}_N$ symmetry under which $i \to (i+1)$. To each copy of the SM we add a heavy Dirac fermion Ψ_i that carries unit charge under the corresponding $U(1)_Y$ hypercharge gauge symmetry, but not under any of the other gauge groups. Each of the N fermions Ψ_i is assumed to have a Yukawa coupling to the scalar Φ. Under the $\mathbb{Z}_N$ symmetry these fields transform as,

$$\Psi_k \to \Psi_{k+1},\; F_k \to F_{k+1},\; \Phi \to \Phi \exp\left\{ i\frac{2\pi}{N} \right\}. \tag{2.2}$$

The discrete symmetry forces the Yukawa couplings, gauge couplings and masses to be same across all the N sectors. The Lagrangian for the Ψ_i is restricted to have the form,

$$\mathcal{L} \supset \sum_{k}^{N} \left\{ \bar{\Psi}_k i \not{D}_k \Psi_k - (M - y\Phi e^{i\frac{2\pi k}{N}} - y\Phi^\dagger e^{-i\frac{2\pi k}{N}})\bar{\Psi}_k\Psi_k \right\}. \tag{2.3}$$

Here the Yukawa coupling y can be chosen to be real without loss of generality as any phase of complex y can be absorbed into the definition of the complex scalar Φ.

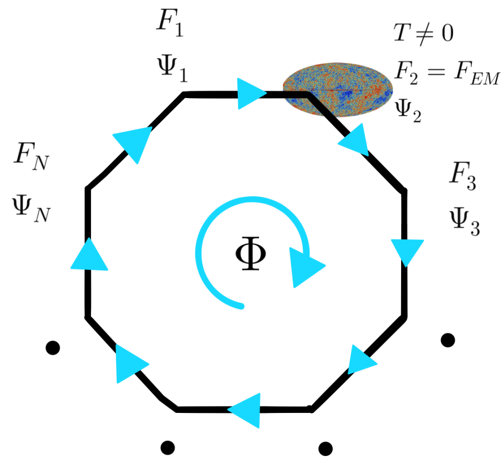

Figure 2.1: A cartoon picture of the $\mathbb{Z}_N$ model. There are N copies of the Standard Model and N copies of a heavy hypercharged vector-like fermion Ψ that are cyclically exchanged under the $\mathbb{Z}_N$ symmetry. A complex scalar Φ transforms linearly under the $\mathbb{Z}_N$ and has a Yukawa coupling to the fermions Ψ_k.

After symmetry breaking, the relevant part of the Lagrangian becomes

$$\mathcal{L} \supset \sum_k^N \bar{\Psi}_k (i\not{D}_k - M_k)\Psi_k, \tag{2.4}$$

where the effective mass of each fermion depends on the VEV of the pseudo-Nambu-Goldstone boson φ

$$M_k = M\left(1 - \epsilon\cos\left(\frac{\varphi}{f} + \frac{2\pi k}{N}\right)\right)\,. \tag{2.5}$$

Here the parameter ϵ is defined as $\epsilon \equiv \sqrt{2}yf/M$. After integrating out the fermions Ψ_k we get a contribution at one loop to the effective potential for the pseudo-Nambu-Goldstone boson,

$$V(\varphi) = -\frac{1}{8\pi^2}\sum_{j=1}^N \int_0^{\Lambda^2} dk_E^2 k_E^2 \log\left[k_E^2 + M_j^2\right], \tag{2.6}$$

where Λ is an ultraviolet cutoff. This integral can be evaluated exactly.

After dropping terms that do not depend on φ and terms that vanish in the limit $M/\Lambda \to 0$, we obtain

$$V(\varphi) = \frac{1}{16\pi^2}\sum_{j=1}^{N}\Big[-2\Lambda^2 M^2(1-\epsilon_j)^2 + 2M^4(1-\epsilon_j)^4\log\frac{\Lambda}{M} + \frac{M^4}{2}(1-\epsilon_j)^4 - 2M^4(1-\epsilon_j)^4\log(1-\epsilon_j)\Big], \tag{2.7}$$

where $\epsilon_j \equiv \epsilon\cos(\varphi/f + 2\pi j/N)$. The first two terms in Eq. (2.7) are quadratically divergent and logarithmically divergent. However, they can be seen to be independent of φ as long as $N > 4$ by virtue of the following identity [95]

$$\sum_{j=1}^{N}\cos^m\left(\frac{\varphi}{f}+\frac{2\pi j}{N}\right) = \begin{cases} 0 & m = \text{ odd} < N \\ \frac{N}{2^m}\binom{m}{m/2} & m = \text{ even} < N \\ \frac{N}{2^{N-1}}\cos\left(\frac{N\varphi}{f}\right) + C & m = N \end{cases}, \tag{2.8}$$

where C is a constant. The finite contribution is, however, φ-dependent. It can be extracted by expanding the last term in Eq. (2.7) in the small parameter ϵ. To all orders in ϵ, we get contributions from each sector that only differ by the phase of the cosine. Due to the identity in Eq. (2.8), all the terms up to $\mathcal{O}(\epsilon^{N-1})$ cancel leaving the leading φ−dependence to appear at $\mathcal{O}(\epsilon^N)$. These cancellations are a direct consequence of the unbroken $\mathbb{Z}_N$ symmetry. After performing the integral in (2.6), the leading φ-dependent piece arises at order ϵ^N

$$V(\varphi) = \frac{M^4\epsilon^N}{8\pi^2}F(N)\cos\left(\frac{N\varphi}{f}\right)[1+\mathcal{O}(\epsilon)], \tag{2.9}$$

where $F(N)$ is given by

$$F(N) = 2^{1-N}N\sum_{l=0}^{4}\binom{4}{l}\frac{(-1)^l}{N-l}. \tag{2.10}$$

This potential has N minima at the locations $\varphi_m/f = (2m-1)\pi/N$ where m runs from 1 to N. Integrating out the fermions Ψ_i also leads to an effective coupling of φ to the gauge kinetic terms of each of the N hypercharge gauge fields at low energies,

$$\mathcal{L}_{eff} \supset -\sum_{j=1}^{N} \frac{\epsilon}{24\pi^2} \cos\left(\frac{\varphi}{f} + \frac{2\pi j}{N}\right) F_j^2. \tag{2.11}$$

One of these N copies corresponds to the hypercharge gauge boson of the SM. Since the effective potential Eq. (2.9) is invariant under $\varphi \to \varphi + 2\pi f/N$, we have freedom to shift φ so that the coupling to SM hypercharge gauge boson simplifies to

$$\mathcal{L}_{\varphi BB} = -\frac{\epsilon}{24\pi^2} \cos\left(\frac{\varphi}{f}\right) F_{\text{Y}}^2. \tag{2.12}$$

Since in our normalization $B_\mu = A_\mu - W_\mu^3$, the coupling to SM photons after spontaneous symmetry breaking takes the same form,

$$\mathcal{L}_{\varphi\gamma\gamma} = -\frac{\epsilon}{24\pi^2} \cos\left(\frac{\varphi}{f}\right) F_{\text{EM}}^2. \tag{2.13}$$

When φ performs small oscillations about one of the minima φ_m of (2.9), it gives rise to a linear term in the coupling to the photon,

$$\mathcal{L}_{\varphi\gamma\gamma} = \frac{\epsilon}{24\pi^2 f} \sin\left(\frac{\varphi_m}{f}\right) \phi F_{\text{EM}}^2, \tag{2.14}$$

where φ_m is the m-th minimum of the potential, Eq. (2.9), and $\varphi = \varphi_m + \phi$. Comparing to

Eq. (1.4), we see that in terms of the parameters of our model, d_e is given by,

$$d_e = \frac{2\epsilon\alpha|\sin(\varphi_m/f)|}{3\pi\kappa f}. \tag{2.15}$$

We are now at a stage where we can demonstrate the improvement in naturalness that our model affords. As discussed in the Introduction, the natural expectation is that the mass of ϕ scales as

$$m^2 \sim \frac{e^2 d_e^2 \kappa^2}{(16\pi^2)^2} M^4 , \tag{2.16}$$

which is just Eq. (1.5) with the divergence cut off by the mass of the new charged fermion, in this case M. To see how our model compares to this, we expand Eq. (2.9) about the minimum to obtain

$$m_\phi^2 = \frac{M^4 N^2 \epsilon^N}{8\pi^2 f^2} F(N) \approx \frac{e^2 d_e^2 \kappa^2}{(16\pi^2)^2} M^4 \left(\frac{1152\pi^6 N^2 F(N) \epsilon^{N-2}}{e^6 \sin^2\left(\frac{\varphi_m}{f}\right)} \right). \tag{2.17}$$

The term in brackets represents the improvement with respect to the naive estimate. In order for this expression to be valid, we had assumed that $N > 4$. Because this correction factor is proportional to ϵ^{N-2}, we see that as long as ϵ is small the mass is parametrically smaller than expected from naive considerations. This demonstrates that our construction can indeed solve the naturalness problem discussed in the Introduction. We note that the mass term for the modulus is generated at one-loop order rather than being given by the naive 2-loop estimate in Eq. (1.5). This is because both the mass of the modulus and its coupling to the hypercharge gauge boson arise at the same one-loop order when the heavy fermions Ψ_i are integrated out, rather than the mass being generated radiatively from the coupling.

At this stage, the new fermions Ψ_k are electrically charged stable fermions. If the reheat temperature is larger than their mass, then these particles obtain a thermal abundance and will tend to overclose the universe if their masses lie above the TeV scale. In order to avoid this, we allow each of the N Ψ_k to decay by introducing a small mixing with the right-handed τ lepton of the corresponding sector through the interaction

$$\mathcal{L} \supset \sum_{k}^{N} m \Psi_k \tau_k^c. \tag{2.18}$$

For $M = 10$ TeV, we require $m \gtrsim 100$ eV in order to have the Ψ particles decay prior to Big Bang nucleosynthesis (BBN) and not pose a cosmological problem.

2.3 Cosmological history

In this section, we will consider the cosmological history of this class of models. We work under the assumption that of the N sectors, ours is the only one that is reheated after inflation[1]. We further assume that φ is homogenized as a result of inflation. The scalar field evolution is governed by the equation

$$\ddot{\varphi} + 3H\dot{\varphi} + \frac{\partial V}{\partial \varphi} = 0 \ , \tag{2.19}$$

where the potential is given by

$$V = V_0(\varphi) + V_T(\varphi, T) \ . \tag{2.20}$$

[1]One way such a scenario can arise is if there are N separate inflatons, one for each sector. Each of the N inflatons is assumed to reheat only its own sector. Then the inflaton that slow rolls to its minimum last is associated with the sector that is identified with the SM, while the other $(N-1)$ sectors are not reheated.

Here V_0 is the zero temperature potential given in Eq. (2.9) while $V_T(\varphi, T)$ is the contribution to the potential from finite temperature effects. An explicit expression for V_T may be found in Appendix A.1. At temperatures $T \gg M$, the finite temperature contribution to the potential can be approximated as,

$$V_T(\varphi, T) \approx \frac{\epsilon}{6} T^2 M^2 \cos\left(\frac{\varphi}{f}\right) . \tag{2.21}$$

Once the temperature falls below its mass, the vector-like fermion Ψ begins to decouple the thermal bath. Accordingly the form of the thermal contribution to the potential undergoes a change. In the temperature range $M \gtrsim T \gtrsim 100$ GeV it is well approximated by the expression,

$$V_T(\varphi, T) \approx \left(\frac{61 \epsilon \alpha^2 q_F^2}{216 \cos^4 \theta_W} T^4 + \frac{4 \epsilon M^{\frac{5}{2}} T^{\frac{3}{2}}}{(2\pi)^{\frac{3}{2}}} e^{-\frac{M}{T}} \right) \cos\left(\frac{\varphi}{f}\right) . \tag{2.22}$$

For $T \lesssim M/20$, the exponential suppression of the second term in the bracket means that it can be neglected.

The evolution of the scalar field φ at early times is governed by the extent to which its oscillations are damped by Hubble friction. To keep track of whether the system is underdamped or overdamped at temperature T, we define the parameter

$$\eta(T) \equiv \frac{4 m^2(T)}{H^2(T)}, \tag{2.23}$$

where $m(T)$ represents the contribution to the mass of the modulus from finite temperature effects,

$$V_T(\varphi, T) \equiv m^2(T) f^2 \cos\left(\frac{\varphi}{f}\right) . \tag{2.24}$$

For $\eta(T) < 1$ the system is overdamped at temperature T, while for $\eta(T) > 1$ it is underdamped.

At early times $\eta(T)$ increases as the universe cools down. This can easily be seen from Eq. (2.21) by noting that when $T \gg M$, the mass scales linearly with temperature, $m(T) \propto T$, while the Hubble parameter decreases faster, $H \propto T^2$. Eventually, at temperatures T of order M, the growth of $\eta(T)$ slows down, reaching its maximal value η_p at a temperature $T_p = \frac{2M}{5}$. The value of η_p is given by

$$\eta_p \equiv \eta(T_p) = \frac{2250\sqrt{5}M_{pl}^2}{e^{\frac{5}{2}}\pi^{\frac{7}{2}}g_*}\frac{\epsilon}{f^2} \,. \tag{2.25}$$

Here M_{pl} is the reduced Planck mass and $g_* = 106.75$ is the effective number of degrees of freedom at $T \lesssim M$, consisting of just the SM fields. For $\eta_p \gtrsim 1$, the field oscillates about the minimum of the thermal potential at temperatures T of order M. The oscillations begin at a temperature T_{osc} such that $m(T_{osc}) = H(T_{osc})$, given by

$$T_{osc} = \sqrt{\frac{15\epsilon M_{pl}^2}{\pi^2 g_*^\Psi f^2}}M \,. \tag{2.26}$$

Here $g_*^\Psi = 110.25$ is the effective number of degrees of freedom at temperatures $T \gg M$, which consists of the SM fields and the associated fermion Ψ.

Below the temperature T_p, $\eta(T)$ decreases rapidly as the exponential suppression of the second term in Eq. (2.22) takes effect. Eventually at temperatures $T \lesssim M/20$, the contribution from the first term in Eq. (2.22) becomes dominant. In this temperature regime, the mass of the modulus and the Hubble parameter scale identically, $m(T) \propto H(T) \propto T^2$. As a result $\eta(T)$

reaches a terminal value η, given by

$$\eta \equiv \eta(T \lesssim M/20) = \frac{305\alpha^2 M_{pl}^2}{3\pi^2 g_* \cos^4\theta_W} \frac{\epsilon}{f^2}. \tag{2.27}$$

The parameters η_p and η play an important role in the description of the system. The value of η_p indicates whether the system undergoes oscillations when $T \gtrsim M$, while η determines the behavior of the system at temperatures $T \lesssim M/20$. These parameters are related as

$$\eta_p = \frac{1350\sqrt{5}\cos^4\theta_W}{61\alpha^2 e^{\frac{5}{2}}\pi^{\frac{3}{2}}}\eta \approx 8300\eta\,. \tag{2.28}$$

From this relation we can see that in the regime which is always overdamped at early times, $\eta \ll 10^{-4}$, the modulus field is effectively frozen until the temperature-independent part of the potential becomes dominant. In contrast, for $\eta > 1$ the oscillations of the field begin at the temperature $T_{osc} \gtrsim M$ and continue till the present time. In the intermediate regime $10^{-4} \lesssim \eta \lesssim 1$, the field oscillates at temperatures T of order M. However, these oscillations have ceased by the time the temperature falls below $M/20$ and only resume once the temperature-independent contribution to the potential begins to dominate.

In what follows below we obtain analytic expressions for the contribution of the modulus ϕ to the energy density of the universe. We focus on the limiting cases of $\eta \ll 10^{-4}$ and $\eta \gtrsim 1$, deferring the intermediate range of η to our numerical study.

2.3.1 $\eta \ll 10^{-4}$

For $\eta \ll 10^{-4}$ the early time evolution is especially simple as Hubble friction freezes the field in place at high temperatures, so that its evolution is independent of V_T. It follows that for sufficiently small η the field is effectively fixed until the mass approaches its zero temperature value, $m = m_\phi$. Oscillations begin when $3H \sim m_\phi$, corresponding to a temperature

$$T_s = \left(\frac{10}{\pi^2 g_*}\right)^{1/4} \sqrt{M_{pl} m_\phi}\,. \tag{2.29}$$

At this point, we make the standard approximation that φ transitions instantly from an over-damped harmonic oscillator to an underdamped one. At this stage the potential Eq. (2.20) is dominated by the zero temperature term,

$$V(\varphi) = \frac{M^4 \epsilon^N}{8\pi^2} F(N) \cos\left(\frac{N\varphi}{f}\right) \equiv \frac{m_\phi^2 f^2}{N^2} \cos\left(\frac{N\varphi}{f}\right). \tag{2.30}$$

The mass m_ϕ is constant so the field will oscillate as an underdamped harmonic oscillator around a minimum φ_m, with the amplitude decaying as

$$\phi \propto a(t)^{-3/2}. \tag{2.31}$$

Since the field is frozen, the value of φ when $3H \sim m_\phi$ can lie anywhere in the range $\varphi_s \in (0, 2\pi f)$. Therefore φ can fall into any of the N minima φ_m of the zero temperature potential, Eq. (2.30), with equal probability. Consequently the initial misalignment value of the excitation around that minimum φ_m can lie anywhere in the range $\phi_s \in (-\pi f/N, \pi f/N)$. Due to this

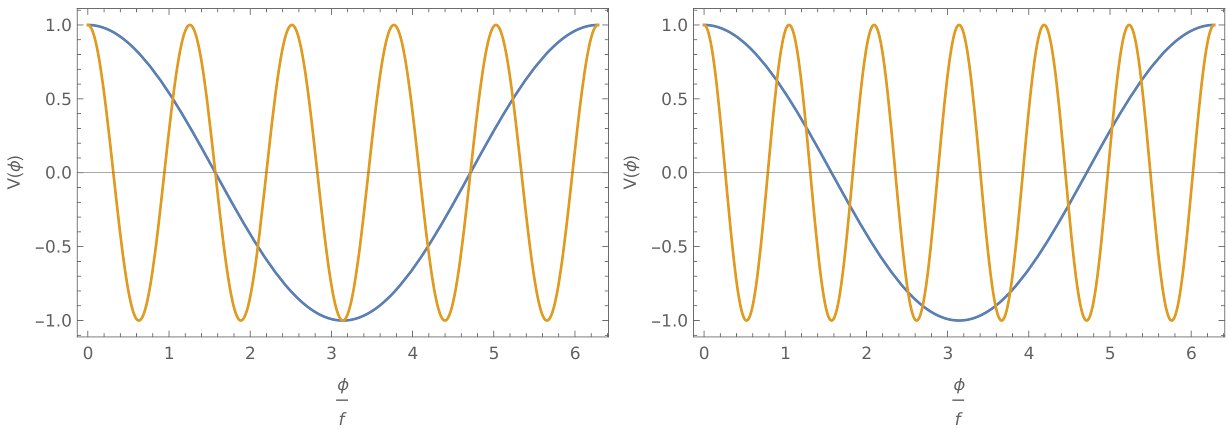

Figure 2.2: Example of thermal (blue) and zero temperature (orange) potentials for $N = 5$ (left) and $N = 6$ (right)

randomness in the initial condition and the homogeneity of ϕ, it is not possible to determine the exact value of the field today. However, what can be done instead is to average over all possible initial misalignment values, $\phi_s \in (-\pi f/N, \pi f/N)$, given that all are equally likely. The expectation value of the energy density $\bar{\rho}_\phi$ can be related to an effective initial amplitude of the field $\phi_{s,\text{eff}}$, where $\phi_{s,\text{eff}} = \sqrt{\langle\phi_s^2\rangle}$. The value of $\sqrt{\langle\phi_s^2\rangle}$ can be obtained by averaging over all values of the initial misalignment, leading to $\phi_{s,\text{eff}} = \frac{\pi f}{\sqrt{3}N}$. As a result the expected amplitude of the field today is given by

$$\phi_0 \approx \phi_{s,\text{eff}} \left(\frac{T_0}{T_s}\right)^{3/2} = \frac{\pi f}{\sqrt{3}N} \left(\frac{T_0}{T_s}\right)^{3/2}, \tag{2.32}$$

where T_0 represents the current temperature of the Universe. This leads to a final result for the energy density in ϕ today,

$$\bar{\rho}_\phi^o = \frac{1}{2} m_\phi^2 \phi_0^2 \approx \frac{\pi^2 f^2 m_\phi^2}{6N^2} \left(\frac{T_0}{T_s}\right)^3 \propto f^2 m_\phi^{1/2}. \tag{2.33}$$

2.3.2 $\eta \gtrsim 1$

In this subsection, we consider the range of parameter space in which the behaviour of φ in the early universe at temperatures $T \lesssim M/20$ is like that of a harmonic oscillator that is either underdamped or close to critically damped. When discussing finite temperature effects, it is necessary to distinguish between the cases when N is even and N is odd. The reason for this can be seen from Fig. 2.2. In the case of even N, the thermal potential pushes φ towards a maximum of the zero temperature potential. At late times, this results in an increase in the amplitude of oscillations, leading to enhanced abundance of dark matter and a larger signal. For odd N, the thermal potential pushes φ towards a minimum of the zero temperature potential, decreasing the amplitude of oscillations at late times resulting in a suppressed abundance. In this case the situation is even worse because the minimum that φ is pushed towards is the one in which there is no linear coupling to the photon, so that the signal under consideration is greatly suppressed. Rather than a linear coupling, this minimum leads to a quadratic coupling, which gives rise to different phenomenology [101, 102] that we do not consider here.

N **odd** In the early universe φ is driven towards the minimum of the finite temperature potential, $\varphi_m = \pi f$. From Fig. 2.2 we see that the minimum of the finite temperature potential is also a minimum of the zero temperature potential. Consequently the range of values of φ at the time when oscillations begin, $H = 3m_\phi$, is significantly smaller than initial $(0, 2\pi f)$.

It follows from this that for each m_ϕ, there is a minimal value of η above which this new range covers only the central minimum of the zero temperature potential, $\varphi_s \in ((\pi - \pi/N)f, (\pi + \pi/N)f)$. Above this critical value of η, which we denote by η_0, φ always ends up in the central minimum. Furthermore, from Eq. (2.14) we see that at this central minimum, $\varphi_m = \pi f$, the linear coupling of ϕ to photons vanishes, resulting in a greatly suppressed signal. The value of η_0 can be well approximated by considering evolution only in the regime $T \lesssim M/20$. The evolution at higher temperatures is less efficient at focusing the range of values of φ due to the sudden drop of the modulus mass $m(T)$ at $T \sim M$, which has the effect of regenerating the amplitude of the field. The subsequent evolution of φ in the regime when $T \lesssim M/20$ and $\eta < 1$ scales with temperature as

$$\varphi - \pi f \propto T^{(1-\sqrt{1-\eta})/2}. \tag{2.34}$$

It follows that η_0 satisfies the condition,

$$\left(\frac{T_s}{M/20}\right)^{(1-\sqrt{1-\eta_0})/2} = \frac{1}{N}. \tag{2.35}$$

From this we obtain an expression for η_0,

$$\eta_0 = 1 - \left(1 - \frac{2\ln N}{\ln \frac{M}{20T_s}}\right)^2 . \tag{2.36}$$

We see that in the case of odd N, for $\eta \geq \eta_0$, the field is pushed to the minimum in which ϕ does not have the coupling shown in Eq. (1.4), resulting in a greatly suppressed signal. The abundance of ϕ is also suppressed limiting its contribution to dark matter.

N **even** For even values of N the picture is completely different. The minimum of the finite temperature contribution to the potential, which is at $\varphi_m = \pi f$, now coincides with the maximum of the zero temperature potential, as can be seen in Fig. 2.2. Therefore, in the regime $\eta \gtrsim 1$ the initial value of the modulus φ at the time when oscillations begin will be close to π and the initial amplitude will be very close to

$$\phi_s = \frac{\pi f}{N}, \tag{2.37}$$

This is very different from the case when the system is overdamped.

The amplitude of the oscillations of ϕ today depends on how close the field is to the minimum of the finite temperature potential at the time that the oscillations begin. Given that the mass of the scalar changes as a function of temperature, the simplest way to determine the behavior of $\varphi(T)$ at these early times is to employ the conservation of the number density of φ. The comoving number density of φ is approximately conserved in the limit that φ is close enough to a minimum that its potential is quadratic and as long as the WKB approximation holds, $dm/dt \ll m^2$. The conserved comoving number density is given by

$$n = a^3 m(T)\left(\varphi - \pi f\right)^2. \tag{2.38}$$

Based on these considerations the effective initial value of the modulus $\phi_{s,eff}$ when the zero temperature potential begins to dominate can be obtained as

$$\left|\phi_{s,\text{eff}} - \frac{\pi f}{N}\right| = \left|\varphi_{s,\text{eff}} - \pi f\right| = \frac{\pi f}{\sqrt{3}}\sqrt{\frac{m(T_{osc})}{m_\phi}\left(\frac{T_s}{T_{osc}}\right)^{\frac{3}{2}}} \;. \tag{2.39}$$

We continue to track the evolution of the field after it rolls down to the new minimum, which happens at temperatures T of order T_s.

In contrast to the case when $\eta \ll 10^{-4}$, the position of φ when the zero temperature contribution to the potential begins to dominate is very close to $\varphi = \pi f$. Since this point corresponds to an extremum of both the finite temperature and zero temperature contributions to the potential, the gradient of the potential at $\varphi = \pi f$ vanishes independent of the temperature. The fact that the potential in the neighborhood of this point is very flat leads to a delayed onset of oscillations [103, 104] and interesting phenomenological signatures [105, 106]. As shown in Appendix A.2, for the parameters considered in this chapter this delay is long enough to ensure that when the oscillations about the new minimum begin, the contributions to the potential from finite temperature effects are already negligible. Therefore, to a good approximation we can assume that the potential has the zero temperature form in Eq. (2.9) from the time that the oscillations begin.

It is tempting to assume that oscillations about the true minimum occur in a harmonic potential, starting from the temperature T_s, defined in Eq. (2.29), with an initial amplitude $\phi_{s,\text{eff}} = \frac{\pi f}{N}$ and continuing till today. This leads to the following expression for the contribution of the oscillating field to the energy density today,

$$\bar{\rho}_\phi^{\text{naive}} \approx \frac{\pi^2 f^2 m_\phi^2}{2N^2}\left(\frac{T_0}{T_s}\right)^3 . \tag{2.40}$$

However, this expression does not give the correct result for the energy density as it fails to account for the the delay in the time at which the oscillations begin. To include this effect we employ the following empirical approximation [104],

$$\bar{\rho}_\phi^u = C\left(\sqrt{\frac{m_\phi}{m(T_{osc})}}\left(\frac{T_{osc}}{T_s}\right)^{\frac{3}{2}}\right) f^2 m_\phi^2 \left(\frac{T_0}{T_s}\right)^3 \propto f^2 m_\phi^{1/2}. \tag{2.41}$$

Here

$$C(y) = \frac{0.23}{N^2}\left(\beta(y) + 4\ln\beta(y)\right)^2 \tag{2.42}$$

and

$$\beta(y) = \ln y + \ln \frac{2^{1/4}\sqrt{3}}{\pi^{1/2}\Gamma(5/4)N} \,. \tag{2.43}$$

The coefficient $C(y)$ defined in Eq. (2.42) corresponds to the correction arising from the delayed onset of oscillations.

The difference between the energy density in Eq. (2.41) and the naive estimate in Eq. (2.40) turns out to be quite significant. For $M = 10$ TeV the correction factor is $\bar{\rho}^u_\phi/\bar{\rho}^{\text{naive}}_\phi \approx 9$ for $N = 6$ and $\bar{\rho}^u_\phi/\bar{\rho}^{\text{naive}}_\phi \approx 10$ for $N = 10$.

Since the field is pushed very close to the central maximum of $V_0(\varphi)$ potential, one could imagine that instead of the field homogeneously rolling down to a unique minimum, quantum fluctuations would push the field in some regions of space to the minimum on the other side of the hill, resulting in domain walls. However, just after inflation, quantum fluctuations are given by [103],

$$\sqrt{\langle(\delta\varphi_i)^2\rangle} \simeq \frac{H_{inf}}{2\pi}. \tag{2.44}$$

The ratio of fluctuations to the average value of the field is constrained by CMB observations,

$$\frac{\sqrt{\langle(\delta\varphi_i)^2\rangle}}{\varphi_{i,eff} - \pi f} \sim \frac{H_{inf}}{f} \lesssim 10^{-5}. \tag{2.45}$$

Because this quantity changes at most logarithmically between the end of inflation and now [107] and the emergence of domain walls requires $\delta\varphi_s \sim \varphi_{s,eff} - \pi f$, this scenario does not take place in our model.

2.4 Signal

In this section, we determine the region of parameter space populated by our model and explore the implications for experiment. Following the conventions employed in [10, 39, 40], we parametrize the changes to α in terms of the variable d_e defined in Eq. (1.4),

$$d_e = \frac{\Delta\alpha}{\alpha}\frac{1}{\kappa\phi_{local}} = \frac{\Delta\alpha}{\alpha}\frac{m_\phi}{\kappa\sqrt{2r\rho_{DM}^{local}}} \,. \tag{2.46}$$

Here $\Delta\alpha$ represents the amplitude of oscillations of the fine structure constant while ϕ_{local} denotes the amplitude of oscillations of the scalar field at the location of the earth. We introduce a parameter r that represents the fractional contribution of ϕ to the total energy density in dark matter,

$$\rho_\phi^{local} = \frac{1}{2}m_\phi^2\phi_{local}^2 = r\rho_{DM}^{local} \,. \tag{2.47}$$

Experiments place a bound on $\Delta\alpha/\alpha$ for a given frequency of oscillation m_ϕ. Then, for a given dark matter fraction r, this can be translated into a bound on d_e using Eq. (2.46).

As can be seen from Eq. (2.15), the value of d_e is a function of the parameters ϵ, f, M and N. From this equation we further see that the value of d_e also depends on the minimum φ_m that the field settles in, which is in turn determined by the initial conditions. In our analysis, we take $|\sin(\varphi_m/f)|$ to be the average of available values, e.g. for $N = 6$ we have $\langle|\sin(\varphi_m/f)|\rangle = 2/3$ in the regime $\eta \ll 10^{-4}$ and $\langle|\sin(\varphi_m/f)|\rangle = 1/2$ in the regime $\eta > 1$. Additionally for odd values of N we ignore the contribution of the central minimum ($\sin(\varphi_m/f) = 0$) to the average. This allows us to determine the expected value of d_e consistent with a given set of parameters.

In order to make contact with experiment it is convenient to eliminate the parameter ϵ in favor of m_ϕ. The expression for m_ϕ in terms of the other four variables is given in Eq. (2.30). The parameter space of our model can then be described in terms of the four variables f, m_ϕ, M and N. Using the results of Section 2.3, the expectation value of the dark matter abundance can also be expressed in terms of these parameters, after averaging over the initial conditions for the scalar field φ. The requirement that, after this averaging, the field ϕ constitutes all of the observed dark matter places a restriction on the allowed parameter space and allows us to fix the value of f in terms of the three other variables. Then d_e is determined in terms of m_ϕ, M and N. Taking advantage of the results of Section 2.3, we can obtain semi-analytical expressions for d_e as a function of these three remaining parameters in various regimes. These will prove helpful in illuminating the main features of the detailed numerical results, which we will present later.

2.4.1 Analytic Results for $\eta \ll 10^{-4}$

In the overdamped limit, we can use Eqs. (2.17), (2.33) and (2.15) to obtain an expression for d_e in terms of m_ϕ, M and N,

$$d_e = A_1(N)\left(\frac{m_\phi}{10^{-20}\text{ eV}}\right)^{\frac{N+6}{4N}}\left(\frac{M}{10\text{ TeV}}\right)^{-\frac{4}{N}}. \tag{2.48}$$

Here

$$A_1(N) = B_0\left(\frac{B_2^{N-2}}{B_1^2}\right)^{\frac{1}{2N}}\frac{(10^{-20}\text{ eV})^{\frac{N+6}{4N}}}{(10\text{ TeV})^{\frac{4}{N}}},$$

$$B_0 = \frac{2\alpha\langle|\sin\varphi_m|\rangle}{3\pi\kappa}, \quad B_1 = \frac{N^2F(N)}{8\pi^2}, \tag{2.49}$$

N	A_1^N	A_2^N	A_3^N	$\eta_{\rm ref}$
5	1.8×10^{-9}	7.5×10^{-4}	N/A	0.58
6	3.9×10^{-8}	N/A	2.7×10^{-3}	N/A
10	1.4×10^{-5}	N/A	1.0×10^{-1}	N/A
11	3.2×10^{-5}	3.2×10^{-2}	N/A	0.77

Table 2.1: Scaling coefficients for Eq. (2.48), Eq. (2.50) and Eq. (2.52) evaluated for a few values of N. A_1^N corresponds to regime where $\eta \ll 10^{-4}$, A_2^N and $\eta_{\rm ref}$ correspond to $\eta \gtrsim 1$ for odd values of N, while A_3^N corresponds to $\eta \gtrsim 1$ for even values of N.

and

$$B_2 = \frac{\pi^2}{6N^2}\left(\frac{\pi^2 g_*}{10}\right)^{3/4} \frac{T_0^3}{\rho_0 M_{pl}^{3/2}}.$$

For convenience, a few values of $A_1(N)$ are given in Table 2.1. This analytic approximation reproduces our detailed numerical results up to an accuracy of around 10%. From Eq. (2.48) we can see that d_e decreases as we raise the mass M of the fermions Ψ. Then, by setting this mass to the lowest value allowed by experiment, we can place an upper bound on d_e as a function of m_ϕ for any given value of N.

2.4.2 Analytic Results for $\eta \gtrsim 1$

f [GeV]	y	M [TeV]	N	m_ϕ [eV]	d_e	ϵ
2.0×10^{16}	3.2×10^{-21}	10	5	10^{-20}	1.8×10^{-9}	9.1×10^{-9}
4.3×10^{14}	2.5×10^{-16}	10	6	10^{-13}	1.2×10^{-4}	1.5×10^{-5}
7.2×10^{15}	4.6×10^{-16}	10	10	10^{-17}	2.2×10^{-4}	4.7×10^{-4}
1.4×10^{16}	3.7×10^{-16}	10	11	10^{-18}	1.9×10^{-4}	7.3×10^{-4}

Table 2.2: Typical values of parameters in our model for a few data points.

As η increases, the scalar field eventually enters the regime $\eta \gtrsim 1$. In this regime, the case of odd N is very different from that of even N. For odd values of N, the region where $\eta \gtrsim 1$ does not give rise to an observable signal because the field is trapped in the wrong vacuum as discussed in Section 2.3. The boundary of this region is marked by η_0, defined in Eq. (2.36).

The condition $\eta < \eta_0$ translates into a restriction on the allowed range of m_ϕ, M and N. From Eqs. (2.17), (2.27) and (2.15) we can determine the value of d_e at the boundary of this region $\eta = \eta_0$ to be

$$d_e = A_2(N)\left(\frac{\eta_0}{\eta_{\rm ref}}\right)^{\frac{N-2}{2(N-1)}}\left(\frac{m_\phi}{10^{-11}\ {\rm eV}}\right)^{\frac{1}{N-1}}\left(\frac{M}{10\ {\rm TeV}}\right)^{-\frac{2}{N-1}}, \tag{2.50}$$

where

$$\begin{aligned} A_2(N) &= B_0 B_1^{-\frac{1}{2(N-1)}}\left(\frac{\eta_{\rm ref}}{B_3}\right)^{\frac{N-2}{2(N-1)}}\frac{(10^{-11}\ {\rm eV})^{\frac{1}{N-1}}}{(10\ {\rm TeV})^{\frac{2}{N-1}}}\,, \\ B_3 &= \frac{305\alpha^2 M_{pl}^2}{3\pi^2 g_* \cos^4\theta_W}\,, \\ \eta_{\rm ref} &= \eta_0(m_\phi = 10^{-11}\ {\rm eV}, M = 10\ {\rm TeV}, N)\,. \end{aligned} \tag{2.51}$$

The numerical values of $A_2(N)$ for a few sample points were given in Table 2.1. The allowed parameter space is restricted to values of d_e lower than Eq. (2.50). The line obtained from Eq. (2.50) is found to reproduce our numerical results up to a factor of 2.

We now turn our attention to the case of even N. The expressions for the energy density in the case $\eta \gtrsim 1$, Eq. (2.41), and the case $\eta \lesssim 10^{-4}$, Eq. (2.33), differ only by their proportionality constant. It follows from this that d_e scales with m_ϕ and M in the same way in both regimes,

$$d_e = A_3(N)\left(\frac{m_\phi}{10^{-11}\ {\rm eV}}\right)^{\frac{N+6}{4N}}\left(\frac{M}{10\ {\rm TeV}}\right)^{\frac{-4}{N}}, \tag{2.52}$$

where

$$
\begin{aligned}
A_3(N) &= B_0 \left(\frac{B_4^{N-2}}{B_2^2} \right)^{\frac{1}{2N}} \frac{(10^{-11}\ \mathrm{eV})^{\frac{N+6}{4N}}}{(10\ \mathrm{TeV})^{\frac{4}{N}}}, \\
B_4 &= C(y_0) \left(\frac{\pi^2 g_*}{10} \right)^{3/4} \frac{T_0^3}{\rho_0 M_{pl}^{3/2}}, \\
y_0 &= \left(\frac{81\pi}{61\sqrt{10}} \right)^{1/4} \sqrt{\frac{\cos^2\theta_W g_*^{5/4} M}{\alpha g_*^{\Psi} \sqrt{m_1 M_{pl}}}}, \\
\frac{m_1}{1\ \mathrm{eV}} &= \left(B_1^2 B_2^{-2(N-1)} B_3^{-2N} M^8 \right)^{\frac{1}{N+3}}.
\end{aligned}
\tag{2.53}
$$

Here m_1, obtained from Eqs. (2.33), (2.17) and (2.27), corresponds to the mass of the modulus for which $\eta = 1$ and $\rho_\phi = \rho_{DM}$. The numerical values of $A_3(N)$ are given in Table 2.1 for a few reference points. Equation (2.52) reproduces the detailed numerical solution up to an accuracy of about 20%.

2.4.3 Numerical Results

The analytic solutions found in the subsection above are valid in the limiting cases when the scalar field is either highly overdamped or highly underdamped. In order to determine the solution in the region of parameter space $10^{-4} \lesssim \eta \lesssim 1$ where the system transitions between these two regimes, we find it necessary to solve Eq. (2.19) numerically. We parametrize the model in terms of the four parameters f, m_ϕ, N and M. As explained earlier, lighter fermion masses are associated with larger values of d_e. In our study, we therefore consider two different values of the fermion mass, $M = 10$ TeV and $M = 1$ TeV, which are close to the current lower bound from collider experiments. In addition, we consider four different values of N, the odd values $N = 5$ and 11 and the even values $N = 6$ and 10. We then scan over f for different values of m_ϕ. For each (f, m_ϕ) pair, the field was evolved from $T_i = f$ to $T = T_0$ starting from 1000 random initial conditions. In the case of odd N, we discard any (f, m_ϕ) pair such that, for more than 90% of initial conditions, the theory ends up in the vacuum with a vanishing signal. For each point, we obtain the contribution of ϕ to the dark matter density. We also determine the value of $\langle|\sin(\varphi_m/f)|\rangle$, which is obtained by averaging over solutions with $\sin(\varphi_m/f) \neq 0$, and use this to find the value of d_e at each point from Eqs. (2.15) and (2.17).

The results of our numerical study are shown in Figs. 2.3 and 2.4, where we have plotted d_e as a function of m_ϕ for these theories, along with the current limits and the projected reach of future experiments. Our goal is to identify the region of parameter space that is naturally populated by these models. To this end, for each m_ϕ we have singled out the value of d_e such that, for any d_e larger than this, more than 90% of points will lead to less than the observed abundance of dark matter, $\rho_\phi < \rho_{DM}$. Separately, for each m_ϕ we have singled out the value of d_e such that, for any d_e smaller than this, more than 90% of points will lead to more than the observed abundance of dark matter, $\rho_\phi > \rho_{DM}$. These values have been plotted in Figs. 2.3 and 2.4 as the two light blue ($M = 1$ TeV) lines. The region between these lines, which corresponds to the natural parameter space for $M = 1$ TeV, has been shaded in. The natural parameter space for $M = 10$ TeV has also been shown, shaded in dark blue. We explicitly show the values of the parameters for a few reference points in Table 2.2.

In order to simplify the numerical computation, the number of effective degrees of freedom in the thermal bath has been held fixed at $g_* = 106.75$. The coefficient of the thermal contribution to the potential from the first term in Eq. (2.22), which also decreases as heavier species go out of the bath, has also been held fixed. These simplifications have an effect on the temperature at which the final oscillations begin, resulting in an overestimate of d_e in the case of the lowest values of m_ϕ by a factor close to two. The error is smaller for larger values of m_ϕ since the

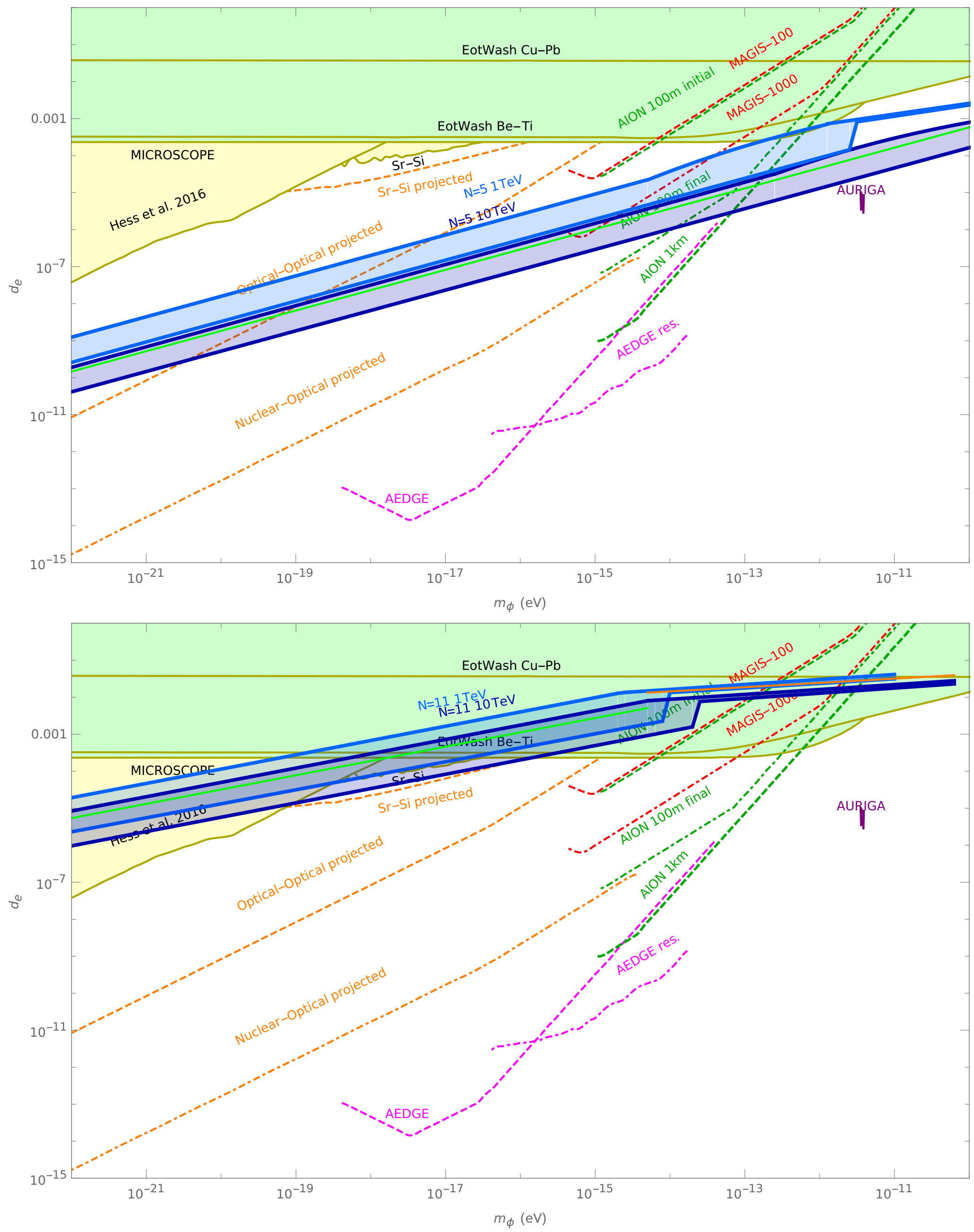

Figure 2.3: d_e vs. m_ϕ for N=5 (left) and N=11 (right). Light ($M = 1$ TeV) and dark ($M = 10$ TeV) blue bands represent a region where no more than 90% of random initial conditions result in either $\rho_\phi > \rho_{DM}$ or $\rho_\phi < \rho_{DM}$. The green line within the dark blue band is a semi-analytic approximation valid in the regime $\eta \ll 10^{-4}$ and the orange line (present in the $N = 11$ plot only) is a semi-analytic approximation of the line above which the signal vanishes, both drawn only for $M = 10$ TeV. Explicit expressions for both lines were given in Eq. (2.48) (green) and Eq. (2.50) (orange). The green band gives current constraints from the Equivalence Principle experiments [2–4], the yellow band presents the current constraints from atomic clock experiments [5, 6] while dashed lines give the potential reach of the future proposed experiments [7–10].

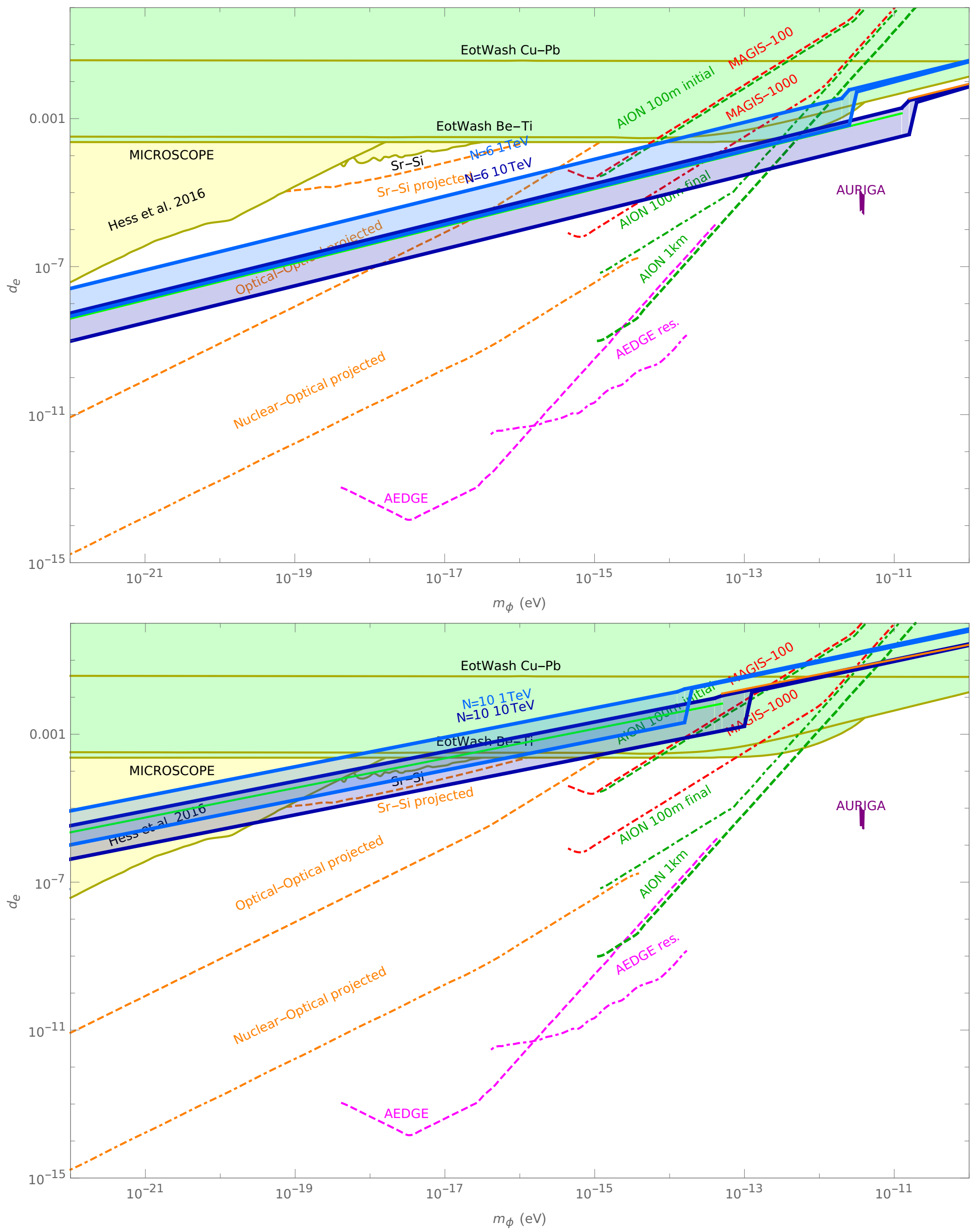

Figure 2.4: d_e vs. m_ϕ for N=6 (left) and N=10 (right). Light (M = 1 TeV) and dark (M = 10 TeV) blue bands represent a region where no more than 90% of random initial conditions result in either $\rho_\phi > \rho_{DM}$ or $\rho_\phi < \rho_{DM}$. The green line within the dark blue band is a semi-analytic approximation valid in the regime $\eta \ll 10^{-4}$ and the orange line is a semi-analytic approximation in the regime $\eta \gtrsim 1$, both drawn only for M = 10 TeV. Explicit expressions for both lines were given in Eq. (2.48) (green) and Eq. (2.52) (orange). The green band gives current constraints from Equivalence Principle experiments [2–4], the yellow band presents the current constraints from atomic clock experiments [5, 6] while dashed lines give potential reach of the future proposed experiments [7–10].

oscillations begin earlier, and so there are a greater number of degrees of freedom in the bath at the corresponding T_s.

In Figs. 2.3 and 2.4, we have also shown the analytic results obtained in subsections 2.4.1 and 2.4.2 for the case of a fermion mass $M = 10$ TeV. For the case of odd N, shown in Fig. 2.3, we have plotted the analytic results obtained from Eqs. (2.48) and (2.50), represented by the green and orange lines respectively. We see that there is good agreement between the analytic formulae and our numerical results. For the lightest moduli, the $d_e(m_\phi)$ lines are in the overdamped regime and the slope closely follows the one predicted by Eq. (2.48) (green line). As the mass increases, the line eventually approaches the region where all solutions fall into the central minimum. In this regime the $d_e(m_\phi)$ line tracks Eq. (2.50) (orange line), as expected.

For the plots in Fig. 2.4 where N is even, the behavior for the lowest masses m_ϕ again follows Eq. (2.48). According to Eq. (2.48) and Eq. (2.52), when $\eta \sim 1$ we should expect that the $d_e(m_\phi)$ line jumps while maintaining the same slope. This is exactly what occurs. For larger values of m_ϕ the lower $d_e(m_\phi)$ line merges with upper one. This occurs because in the ($\eta > 1$) region, as mentioned earlier, essentially all initial conditions lead to $\phi_s = \pi f/N$ as an initial condition. Therefore the parameter space populated by the model is essentially independent of the initial misalignment angle.

In Figs. 2.3 and 2.4, we see the preferred parameter space of our model for various choices of M and N. From these figures, it is clear that our models span a wide range of d_e and m_ϕ. Larger values of N are currently being probed by ongoing experiments while smaller values of N are within reach of future experiments. Much as how the QCD axion line provides a goalpost for axion experiments, our small N models constitute a well-motivated scenario that future experiments should aim to reach.

2.5 Conclusions

Light moduli are one of the most attractive dark matter candidates. Not only are they ubiquitous in ultraviolet-complete models such as string theory, but the misalignment mechanism provides a simple explanation for their abundance. Despite these appealing features, detecting modulus dark matter remains a challenge. The problem is that the large coupling required to find them tends to be at odds with their very light mass, resulting in a hierarchy problem. In this chapter, we have shown that a nonlinearly realized $\mathbb{Z}_N$ symmetry can naturally protect the mass of a modulus against radiative corrections, provided the modulus itself transforms nonlinearly under the $\mathbb{Z}_N$. It remains an intriguing open question whether a model that exhibits these features can be constructed within a string theory framework.

Much like the QCD axion, these models have a region of parameter space in which they naturally reproduce the observed dark matter abundance via the misalignment mechanism. The regions of parameter space populated by these models were shown in Figs. 2.3 and 2.4 for a few values of N. We see from these figures that future experiments searching for time variation of the fine structure constant are expected to probe a large part of the preferred parameter space. This class of models is both simple and testable and provides additional theory motivation for exciting new quantum limited experiments.

Chapter 3: Searching for a Fifth Force with Atomic and Nuclear Clocks

3.1 Introduction

In this chapter we explore a different approach to detecting long-range forces that violate the EP, based on the rapidly-improving sensitivity of atomic and nuclear clocks [108–111]. Using precision clock experiments to search for new physics is a rapidly growing field, see Ref. [112] for a review. We limit our attention to the case when the fifth force is mediated by an ultralight scalar field. In general, the sun and the earth act as sources for any such scalar field. Then, since the values of fundamental parameters such as the fine structure constant α depend on the value of the scalar field, there are corrections to atomic and nuclear spectra that depend on the distance from these sources [113–115]. Atomic and nuclear clocks are sensitive to the frequencies of these transitions, and can therefore be used to search for position dependence of fundamental parameters. Since this effect is associated with EP violation [116, 117], this offers an alternative method of searching for EP violating fifth forces. Clock experiments also offer a new approach to detecting more exotic fifth forces such as chameleon models [118–121] that is distinct from the existing search methods [122–124].

Clock searches for EP violation are based on comparing two atomic or nuclear transition frequencies against each other. These frequencies could be those of two different clocks at the same physical location, or alternatively, two clocks at separate locations. In the case of two clocks at the same location, as long as their transition frequencies scale differently with fundamental parameters such as α, the ratio of their frequencies will change as the distance from the source changes. For example, since the orbit of the earth around the sun is not a perfect circle, this results in an annual modulation in the frequencies of atomic and nuclear clocks [113–115]. We determine the sensitivities of current and next-generation atomic and nuclear clocks to this effect and compare the results against the existing laboratory and astrophysical constraints on EP violating fifth forces. We show that in the future, the annual modulation in the frequencies of atomic and nuclear clocks in the laboratory caused by the eccentricity of the earth's orbit around the sun may offer the most sensitive probe of this general class of EP violating theories.

Even greater sensitivity can be obtained by comparing clocks at different locations. Comparing the frequency difference between a precision clock placed on a satellite in an eccentric orbit around the earth and a similar clock on earth would offer an extremely sensitive probe of this class of models. Experiments of this type have already been performed to test the general relativistic prediction for the gravitational redshift [125, 126], and new ones proposed [14, 16, 127]. Importantly, we find that such an experiment that employs current clock technology would already have a sensitivity to fifth forces that couple primarily to electrons at the about the same level as the existing limits. The reason for this is that direct fifth force searches are inherently less sensitive to forces acting on electrons, since electrons comprise less than 0.1% of the mass of an atom. In contrast, atomic transition frequencies are extremely sensitive to the properties of the electron. Our analysis provides well-defined sensitivity targets to aim for when designing future versions of these experiments.

The outline of this chapter is as follows. In the section 3.2 we consider the interactions of an ultralight scalar with the SM and discuss the current constraints on this framework from direct searches for EP violation and from recasting existing clock experiments. In Section 3.3 we study the sensitivity of next-generation atomic and nuclear clocks to this class of models, and show that they can explore new parameter space. We conclude in Section 3.4.

3.2 Ultralight Scalar Fields and Equivalence Principle Violation

In this section, we present a general framework for studying the effects of an ultralight scalar coupled to the SM. We show how direct fifth force, gravitational redshift, and differential redshift measurements can be used to place bounds on the parameters in the Lagrangian. This allows a concrete comparison of the sensitivities of these different experiments.

Consider an ultralight light scalar field ϕ that couples to the particles in the SM. At energies well below the weak scale, the interactions of ϕ with the stable matter fields and the light force carriers of the SM can be conveniently parametrized as [39, 40]

$$\mathcal{L} \supset \kappa\phi\Big[\frac{d_e}{4e^2}F_{\mu\nu}F^{\mu\nu} - \frac{d_g\beta_3}{2g_3}G^A_{\mu\nu}G^{A\mu\nu} - d_{m_e}m_e\bar{\psi}_e\psi_e - \sum_{i=u,d}(d_{m_i}+\gamma_{m_i}d_g)m_i\bar{\psi}_i\psi_i\Big] \; . \quad (3.1)$$

Here the parameter κ is defined as $\kappa = \sqrt{4\pi G}$, where G is Newton's constant. This parametrization allows a straightforward comparison between the force mediated by the ultralight scalar and gravitational effects. In this expression e represents the charge of the electron, g_3 the coupling constant of quantum chromodynamics (QCD) and $\beta_3 \equiv \partial g_3/\partial \log\mu$ its beta function. The parameters m_i denote the masses of the fermions and $\gamma_m \equiv -\partial \log m/\partial \log\mu$. The parameters d_x with $x \in \{e, g, m_i\}$ represent the couplings of the scalar to the corresponding gauge bosons and fermions. The couplings of the scalar have been parametrized such that the limit $d_g = d_{m_e} = d_{m_i}$ with $d_e = 0$ corresponds to the interactions of a dilaton that respects the equivalence principle.

At these energies the SM has an approximate parity symmetry under which ϕ has been taken to be even. This represents the most general form of the interaction consistent with the symmetries up to terms of dimension 5 and linear order in ϕ. In order to isolate the EP violating effects, it is conventional to parameterize the Lagrangian in Eq. (3.1) in terms of the average light quark mass $\hat{m} \equiv (m_u + m_d)/2$ and the mass difference $\delta m \equiv (m_d - m_u)$ rather than the light quark masses m_u and m_d. The corresponding couplings of the modulus take the form,

$$\mathcal{L} \supset -\kappa\phi\left[d_{\hat{m}}\hat{m}(\bar{d}d + \bar{u}u) + \frac{d_{\delta m}}{2}\delta m(\bar{d}d - \bar{u}u)\right], \tag{3.2}$$

where

$$d_{\hat{m}} = \frac{d_{m_d}m_d + d_{m_u}m_u}{m_d + m_u}, \qquad d_{\delta m} = \frac{d_{m_d}m_d - d_{m_u}m_u}{m_d - m_u}.$$

As a result of the interactions in Eq. (3.1), the scalar field gives rise to a force between any two macroscopic bodies [40]. By convention, this new force is parametrized in terms of its strength relative to the gravitational force. Accordingly, the potential energy V, which includes the effects of both the gravitational force and the new force, now takes the form,

$$V = -G\frac{m_{\mathbf{A}}m_{\mathbf{B}}}{r_{\mathbf{AB}}}(1 + \alpha_{\mathbf{A}}\alpha_{\mathbf{B}}e^{-\frac{r_{\mathbf{AB}}}{\lambda}}) \,. \tag{3.3}$$

Here $m_{\mathbf{A}}$ and $m_{\mathbf{B}}$ are the masses of the two bodies **A** and **B**, $r_{\mathbf{AB}}$ is the distance between them, and $\lambda \equiv 1/m_\phi$ sets the range of the interaction. The parameters $\alpha_{\mathbf{A}}$ and $\alpha_{\mathbf{B}}$, which are functions of d_e, d_g, d_{m_e} and d_{m_i}, depend on the compositions of **A** and **B**. Therefore, in general, the force mediated by ϕ violates the EP. The parameters $\alpha_{\mathbf{A}}$ and $\alpha_{\mathbf{B}}$ can be approximated as,

$$\alpha_{\mathbf{X}} \simeq d_g^* + \quad \left[(d_{\hat{m}} - d_g)Q_{\hat{m}} + (d_{\delta m} - d_g)Q_{\delta m} + (d_{m_e} - d_g)Q_{m_e} + d_e Q_e\right]_{\mathbf{X}} \ , \tag{3.4}$$

where the composition-independent part d_g^* is given by

$$d_g^* \equiv d_g + 0.093(d_{\hat{m}} - d_g) + 10^{-4}[2.7 d_e + 2.75(d_{m_e} - d_g)]. \tag{3.5}$$

The remaining composition-dependent part of $\alpha_{\mathbf{X}}$ in Eq. (3.4) is parameterized in terms of the variables $Q_{\hat{m}}$, $Q_{\delta m}$, Q_e and Q_{m_e} that depend on the mass number A and atomic number Z of the atomic nuclei of which the body is composed[1],

$$Q_{\hat{m}} \equiv -\frac{0.036}{A^{1/3}} - 1.4 \times 10^{-4} \frac{Z(Z-1)}{A^{4/3}} - 0.02 \frac{(A-2Z)^2}{A^2}, \tag{3.6}$$

$$Q_{\delta m} \equiv 1.7 \times 10^{-3} \frac{A-2Z}{A}, \tag{3.7}$$

$$Q_e \equiv 7.7 \times 10^{-4} \frac{Z(Z-1)}{A^{4/3}} + 8.2 \times 10^{-4} \left(\frac{Z}{A} - \frac{1}{2}\right), \tag{3.8}$$

$$Q_{m_e} \equiv 5.5 \times 10^{-4} \left(\frac{Z}{A} - \frac{1}{2}\right). \tag{3.9}$$

We see from this that $\alpha_{\mathbf{X}}$ naturally splits up into a composition-independent term d_g^* and a composition-dependent term that is contained in the square bracket in Eq. (3.4). For a general choice of modulus couplings the term in the square brackets does not vanish, so the contribution to the potential from the ultralight scalar depends on the compositions of the test bodies. Therefore the resulting force violates the weak EP. The existing limits on EP violating forces can be

[1]Our parametrization of $\alpha_{\mathbf{X}}$ differs from that in Ref. [40], and so our expressions for $Q_{\hat{m}}$, $Q_{\delta m}$, Q_e and Q_{m_e} are also different.

translated into bounds on the couplings of the scalar ϕ.

We see from Eq. (3.6) that $|Q_{\delta m}| \ll |Q_{\hat{m}}|$. We therefore expect that, in general, experiments searching for EP violation will be much more sensitive to the coupling $d_{\hat{m}}$ than to $d_{\delta m}$. For simplicity, we will therefore neglect the coupling $d_{\delta m}$ in the discussion that follows.

Apart from generating an EP violating force, the interactions in Eq. (3.1) imply that the effective values of fundamental constants such as α and m_e at any given location depend on the value of ϕ at that location. For example, for these two parameters we have,

$$\alpha(x) = \bar{\alpha}[1 + d_e \kappa \phi(x)] \quad m_e(x) = \bar{m}_e[1 + d_{m_e} \kappa \phi(x)] \, . \tag{3.10}$$

Here $\bar{\alpha}$ ($\bar{m}_e$) denotes the value of the fine structure constant (electron mass) in the absence of the terms in Eq. (3.1). Consequently the sourcing of ϕ by massive objects such as the sun and the earth causes the value of fundamental constants such as α and m_e to depend on the distance from these sources. This offers an alternative method of probing this class of models using atomic and nuclear clocks, which is the focus of this chapter.

3.2.1 Direct Fifth Force Measurements

In this subsection we review how to map the limits from direct fifth force searches onto bounds on the parameters in Eq. (3.1). The results are summarized in Eqs. (3.15), (3.16), (3.17) and (3.18).

At present, the most precise tests of EP violation are based on measurements of how two test bodies **A** and **B** composed of different materials accelerate towards a third body **C**, which is usually the earth or the sun. If the EP holds, the two accelerations should be identical. By convention, the experimental limits on EP violation are expressed in terms of the Eotvos parameter,

$$\eta \equiv 2\frac{|\vec{a}_{\mathbf{A}} - \vec{a}_{\mathbf{B}}|}{|\vec{a}_{\mathbf{A}} + \vec{a}_{\mathbf{B}}|} \tag{3.11}$$

where $a_{\mathbf{A}}$ and $a_{\mathbf{B}}$ represent the accelerations of the test bodies **A** and **B**. Since the interactions in Eq. (3.1) give rise to an EP violating force between any two macroscopic bodies, the experimental limits on η can be translated into bounds on the couplings of the ultralight scalar to matter.

In the limit that the distances between the bodies **A**,**B** and **C** are all much smaller than λ, so that the mass of the modulus can be neglected, we can estimate the Eotvos parameter in this class of models from Eq. (3.3) as,

$$\eta \approx (\alpha_{\mathbf{A}} - \alpha_{\mathbf{B}})\alpha_{\mathbf{C}} \quad \approx \left[\Delta Q_{\hat{m}}(d_{\hat{m}} - d_g) + \Delta Q_e d_e + \Delta Q_{m_e}(d_{m_e} - d_g)\right]\alpha_{\mathbf{C}} \,. \tag{3.12}$$

In most simple models the composition independent part of $\alpha_{\mathbf{C}}$ will dominate over composition dependent part. In this case we can make the approximation $\alpha_{\mathbf{C}} \approx d_g^*$ so that

$$\eta \quad \approx \left[\Delta Q_{\hat{m}}(d_{\hat{m}} - d_g) + \Delta Q_e d_e + \Delta Q_{m_e}(d_{m_e} - d_g)\right] d_g^* \tag{3.13}$$

$$\approx \Delta Q_{\hat{m}} D_{\hat{m}} + \Delta Q_e D_e + \Delta Q_{m_e} D_{m_e} \,. \tag{3.14}$$

Here we have defined $D_e \equiv d_g^* d_e$, $D_{\hat{m}} \equiv d_g^*(d_{\hat{m}} - d_g)$ and $D_{m_e} \equiv d_g^*(d_{m_e} - d_g)$. Since typically $\Delta Q_{m_e} \ll \Delta Q_e\,, \Delta Q_{\hat{m}}$, using the experimental bound on η for two given test bodies of known compositions, the allowed $(D_{\hat{m}}, D_e)$ parameter space can be constrained to a band as shown in Fig. 3.1. The most accurate measurement of η, performed by the MICROSCOPE mission [2,12],

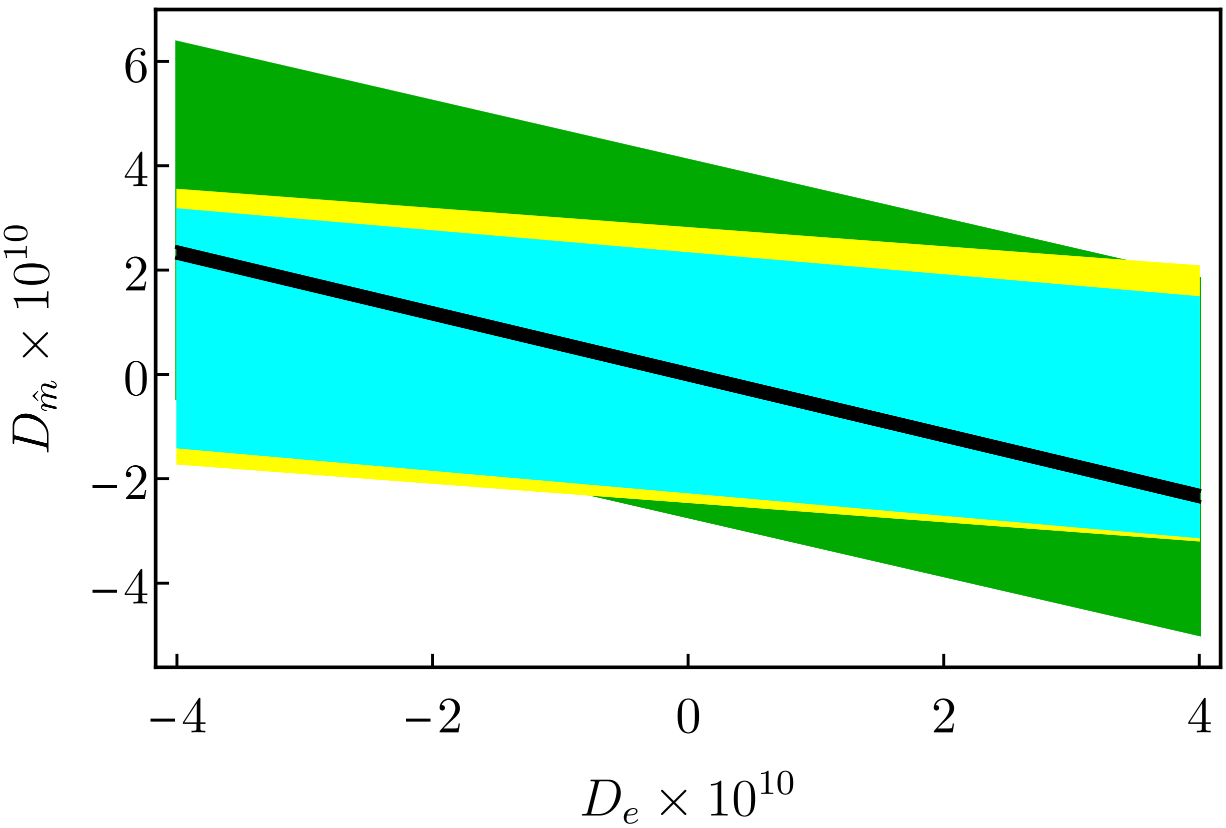

Figure 3.1: Current bounds on D_e vs. $D_{\hat{m}}$ set by fifth force experiments [2, 11–13]. The black band represents the bound set by MICROSCOPE [2, 12], the blue and yellow bands are the constraints set by the EotWash group with Be-Ti and Be-Al masses [11], and the green band is the Moscow group's result obtained with Al-Pt masses [13].

sets constraints at the 10^{-14} level and is represented by the black band in Fig. 3.1.

In addition to constraining the $D_{\hat{m}}$ and D_e parameters, we can translate the bounds on the Eotvos parameter η into limits on the individual modulus couplings d_x. For example, using Eq. (3.12) we can set an upper bound on d_g assuming that all the other couplings vanish,

$$\eta \approx \Delta Q_{\hat{m}} d_g^2 \quad \Rightarrow \quad d_g = \sqrt{\frac{\eta}{\Delta Q_{\hat{m}}}}\,, d_{\hat{m}} = d_{m_e} = d_e = 0. \tag{3.15}$$

The analogous bounds on d_e, $d_{\hat{m}}$ and d_{m_e} are given by,

$$d_e = \sqrt{\frac{\eta}{\Delta Q_e(2.7\times 10^{-4} + Q_{e,\mathbf{C}})}}\ ,\ d_{\hat{m}} = d_{m_e} = d_g = 0, \tag{3.16}$$

$$d_{\hat{m}} = \sqrt{\frac{\eta}{\Delta Q_{\hat{m}}(9.3\times 10^{-2} + Q_{\hat{m},\mathbf{C}})}}\ ,\ d_{m_e} = d_e = d_g = 0, \tag{3.17}$$

$$d_{m_e} = \sqrt{\frac{\eta}{\Delta Q_{m_e}(2.75\times 10^{-4} + Q_{m_e,\mathbf{C}})}}\ ,\ d_{\hat{m}} = d_e = d_g = 0. \tag{3.18}$$

By performing multiple measurements on bodies of different compositions, it is in principle possible to set independent constraints on all of the D_x and d_x parameters.

Although these bounds have been obtained under the assumption that the distances between the bodies **A**, **B** and **C** are all much smaller than λ, the extension of these limits to the more general case is straightforward [2, 128],

$$d_x = \frac{d_x^{\text{massless}}}{\sqrt{\Phi(\frac{R_{\mathbf{C}}}{\lambda})(1+\frac{r}{\lambda})e^{-\frac{r}{\lambda}}}}\ . \tag{3.19}$$

Here $\Phi(x) \equiv 3(x\cosh x - \sinh x)/x^3$, $R_{\mathbf{C}}$ is the radius of the body **C**, and d_x^{massless} represents the corresponding bound in the limit that $m_\phi = 0$, given by Eqs. (3.15), (3.16), (3.17) and (3.18).

3.2.2 Clock Experiments

In this subsection, we show how to map the results of clock experiments onto the parameter space shown in Eq. (3.1). This allows for a direct comparison between clock experiments and direct fifth force measurements.

While direct measurement of the fifth force currently provides the most stringent constraints on the couplings d_x of the ultralight scalar, there is an alternative method to constrain the new force. Recall that the couplings introduced in Eq. (3.1) modify the potential energy between two masses as shown in Eq. (3.3). The correction to the potential energy can be rewritten in the familiar form,

$$\delta V = -G\frac{m_{\mathbf{A}}m_{\mathbf{B}}}{r_{\mathbf{AB}}}\alpha_{\mathbf{A}}\alpha_{\mathbf{B}}e^{-\frac{r_{\mathbf{AB}}}{\lambda}} = -\frac{q_{\mathbf{A}}q_{\mathbf{B}}}{4\pi r_{\mathbf{AB}}}e^{-\frac{r_{\mathbf{AB}}}{\lambda}}\ , \tag{3.20}$$

where $q_{\mathbf{X}} = \kappa\alpha_{\mathbf{X}}m_{\mathbf{X}}$ represents the charge of the body under the new Yukawa force. From the above expression we see that each massive body $\mathbf{X}$ sources the scalar field ϕ as,

$$\phi_{\mathbf{X}} = -\frac{q_{\mathbf{X}}}{4\pi r}e^{-\frac{r}{\lambda}}. \tag{3.21}$$

As can be seen from Eq. (3.10), the scalar field ϕ affects the values of fundamental constants. This results in a spatial variation in the values of fundamental constants in the vicinity of a source body $\mathbf{X}$. For example, in the case of the fine structure constant we have,

$$\frac{\Delta\alpha}{\alpha} = d_e\kappa\phi_{\mathbf{X}} = -\frac{d_e\alpha_{\mathbf{X}}Gm_{\mathbf{X}}}{r}e^{-\frac{r}{\lambda}} = d_e\alpha_{\mathbf{X}}U_{\mathbf{X}}e^{-\frac{r}{\lambda}}\ . \tag{3.22}$$

Here $U_{\mathbf{X}}$ represents the gravitational potential sourced by the body $\mathbf{X}$. From the above equation, we see that measuring the variation of fundamental constants in the neighborhood of a massive body such as the earth or sun allows us to probe the same couplings that direct fifth force searches are sensitive to. We now discuss the sensitivity of atomic and nuclear clocks to this variation.

The principle of Local Position Invariance (LPI) states that the frequency of any given clock in its local frame is independent of its position in space. This can be expressed as

$$f_A^{local}(x) = f_A^{local}(\infty), \tag{3.23}$$

where $f_A^{local}(\infty)$ denotes the frequency of the clock A at infinity, where the gravitational potential U vanishes. It follows from Eq. (3.22) that in the class of theories we are considering the values of the fundamental constants are not the same at different points in space. Then the frequencies of clocks depend on their location in space and so the principle of LPI is no longer valid. Therefore Eq. (3.23) will receive corrections whose magnitude will, in general, depend on the type of the clock used in the experiment. This violation of LPI can be parametrized in terms of the anomalous redshift parameter β_A as

$$\frac{f_A^{local}(x) - f_A^{local}(\infty)}{f_A^{local}(\infty)} = \beta_A U(x) \ , \tag{3.24}$$

where values of β_A different from zero are the result of new physics. The subscript A indicates the type of clock being employed. In practice, when comparing two clocks, one typically measures frequencies in the rest frame of one of the clocks, which we identify with the lab frame. This leads to the relation [2]

$$\frac{f_A^{\text{lab}}(x) - f_A^{\text{lab}}(x_{\text{lab}})}{f_A^{\text{lab}}(x_{\text{lab}})} = (1 + \beta_A)[U(x) - U(x_{\text{lab}})] \ . \tag{3.25}$$

Here, the term 1 in the parentheses represents the standard prediction from general relativity and x_{lab} denotes the position of the lab.

[2] In the literature, the anomalous redshift parameter β is conventionally defined as $\frac{f_A^{\infty}(x) - f_A^{\infty}(\infty)}{f_A^{\infty}(\infty)} = (1+\beta)U(x)$, as seen by the observer at infinity. This definition implicitly assumes that the anomalous scaling is independent of the clock used and is therefore not suitable for our purposes.

The dependence of a clock transition on fundamental parameters is conventionally expressed as

$$f_A \propto R\,\alpha^{K_\alpha^A}\mu^{K_\mu^A}X_q^{K_q^A} \propto m_e\,\alpha^{K_\alpha^A+2}\mu^{K_\mu^A}X_q^{K_q^A}, \tag{3.26}$$

where α is the fine structure constant, $\mu \equiv m_p/m_e$ is the proton-to-electron mass ratio, $X_q \equiv m_q/\Lambda_{QCD}$ is the ratio of the average light quark mass to the QCD scale and $R \propto m_e\alpha^2$ denotes the Rydberg constant. The coefficients $K^A_{\alpha,\mu,q}$ characterize the sensitivity of a given transition to variations of the corresponding parameters. Typically, $K_\mu^A = -1$ for hyperfine transitions, $K_\mu^A = 0$ for optical and $K_\mu^A = 1$ for nuclear transitions. The $K^A_{\alpha,q}$ have to be determined numerically for each transition.

From Eqs. (3.24) and (3.26) we find

$$\beta_A U(x) = \frac{\Delta m_e}{m_e} + (K_\alpha^A + 2)\frac{\Delta\alpha}{\alpha} + K_\mu^A\frac{\Delta\mu}{\mu} + K_q^A\frac{\Delta X_q}{X_q}\ , \tag{3.27}$$

where $\frac{\Delta X}{X} = \frac{X(x)-X(\infty)}{X(\infty)}$ with $X \in \{\alpha, \mu, X_q, m_e\}$. Using this equation, constraints on β_A can be turned into bounds on the variation of various fundamental constants.

In order to compare these bounds with those from fifth force experiments we need to express the variation of the fundamental parameters in terms of the couplings shown in Eq. (3.1)[3].

[3]The following discussion implicitly assumes that the gravitational potential can be independently determined in the presence of the fifth force. We study this potential complication in Appendix B.1 and show that it has only a small effect on the results of this section.

A brief calculation yields

$$\frac{\Delta\alpha}{\alpha} = d_e\alpha_{\mathbf{X}}U \simeq D_eU, \tag{3.28}$$
$$\frac{\Delta\mu}{\mu} = -(d_{m_e} - d_g)\alpha_{\mathbf{X}}U \simeq -D_{m_e}U, \tag{3.29}$$
$$\frac{\Delta X_q}{X_q} = (d_{\hat{m}} - d_g)\alpha_{\mathbf{X}}U \simeq D_{\hat{m}}U, \tag{3.30}$$
$$\frac{\Delta m_e}{m_e} = d_{m_e}\alpha_{\mathbf{X}}U \simeq (D_{m_e} + D_g)U\ , \tag{3.31}$$

where in the second step we have approximated $\alpha_{\mathbf{X}} \approx d_g^*$ and defined $D_g \equiv d_g d_g^*$. These expressions are valid for $r \ll \lambda$. Experiments that constrain the variation of fundamental constants sometimes employ the alternative parameterization, $\Delta X/X = k_X U$. From Eq. (3.28), we see that $k_\alpha = D_e$, $k_\mu = -D_{m_e}$, and $k_q = D_{\hat{m}}$. The translation of bounds between the two different parametrizations is therefore straightforward.

From Eqs. (3.27) and (3.28) we can express β_A in terms of the couplings of the modulus,

$$\beta_A = \left[(K_\alpha^A + 2)d_e - K_\mu^A(d_{m_e} - d_g) + K_q^A(d_{\hat{m}} - d_g) + d_{m_e}\right]\alpha_{\mathbf{X}} \tag{3.32}$$
$$\approx (K_\alpha^A + 2)D_e + (1 - K_\mu^A)D_{m_e} + K_q^A D_{\hat{m}} + D_g\ . \tag{3.33}$$

Since direct fifth force measurements are also sensitive to the D_x, the relation above allows for a direct comparison between these experiments and clock experiments.

We can translate the bounds on β_A into bounds on the modulus couplings d_x under the assumption that only one coupling has a non-zero value,

$$d_g = \sqrt{\frac{\beta_A}{|K_\mu^A - K_q^A|}}\ ,\ d_{\hat{m}} = d_e = d_{m_e} = 0, \tag{3.34}$$

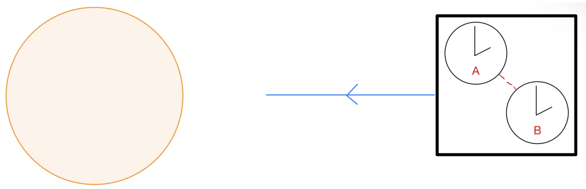

Figure 3.2: A schematic picture of an experiment involving two different clocks that travel together and experience the same change in the gravitational potential. The location dependence of the ratio of the two transition frequencies is a sensitive probe of EP violation.

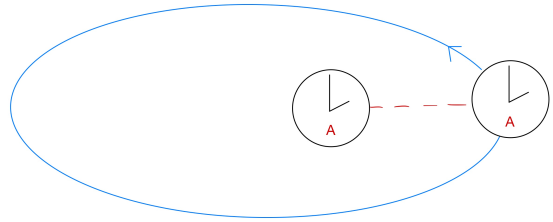

Figure 3.3: A schematic picture of an experiment involving two identical clocks that are spatially separated. The dependence of the difference in frequencies between the two clocks on the difference in the gravitational potential between their locations is a sensitive probe of EP violation.

$$d_e = \sqrt{\frac{\beta_A}{|K_\alpha^A + 2|(2.7\times 10^{-4} + Q_{e,X})}}\,,\ d_{\hat{m}} = d_g = d_{m_e} = 0, \tag{3.35}$$

$$d_{\hat{m}} = \sqrt{\frac{\beta_A}{|K_q^A|(9.3\times 10^{-2} + Q_{\hat{m},X})}}\,,\ d_e = d_g = d_{m_e} = 0. \tag{3.36}$$

$$d_{m_e} = \sqrt{\frac{\beta_A}{|1-K_\mu^A|\,(2.75\times 10^{-4} + Q_{m_e,X})}}\,,\ d_e = d_g = d_{\hat{m}} = 0. \tag{3.37}$$

By employing multiple clocks, each of a different composition, it is in principle possible to set independent constraints on all of the D_x and d_x parameters.

Our results have been derived under the assumption that the experiments were performed at distances such that $r \ll \lambda$. When we relax this assumption, the above formulas generalize to [128]

$$d_x = \frac{d_x^{\text{massless}}}{\sqrt{\Phi(\frac{R_{\mathbf{X}}}{\lambda})e^{-\frac{r}{\lambda}}}}, \tag{3.38}$$

where d_x^{massless} is the corresponding parameter given in Eqs. (3.34), (3.35), (3.36) and (3.37).

The clock experiments that search for fifth forces fall into two distinct classes, differential redshift measurements and gravitational redshift measurements, illustrated in Figs. 3.2 and

3.3 respectively. Differential redshift measurements involve comparing two clocks composed of different materials at the same location as they orbit another body. Gravitational redshift measurements involve comparing the frequencies of a clock in orbit around the earth with a clock on earth. This class of experiments is sensitive to the redshift predicted by general relativity and bounds are placed on any additional source of redshift. We now consider the existing limits from these two classes of experiments in turn.

We first consider differential redshift measurements. A comparison of two different clocks A and B that experience the same change in the potential allows a measurement of the difference $(\beta_A - \beta_B)$. Then, using Eq. (3.32), we can easily recover information about the couplings of the modulus,

$$\begin{aligned}\beta_{AB} &= [\Delta K_\alpha^{AB} d_e - \Delta K_\mu^{AB}(d_{m_e} - d_g) + \Delta K_q^{AB}(d_{\hat{m}} - d_g)]\alpha_{\mathbf{X}} && (3.39)\\ &\approx \Delta K_\alpha^{AB} D_e - \Delta K_\mu^{AB} D_{m_e} + \Delta K_q^{AB} D_{\hat{m}} \,. && (3.40)\end{aligned}$$

Here we have defined, $\beta_{AB} \equiv \beta_A - \beta_B$ and $\Delta K_X^{AB} \equiv K_X^A - K_X^B$.

A natural realization of the experiment involves comparing the frequencies of two different clocks in the laboratory over the course of a year [15, 129, 130]. As the distance between earth and the sun changes due to the eccentricity of the orbit, the frequencies of the clocks change accordingly. The ratio of the frequencies of the two clocks, $\tilde{f}(x) \equiv f_A^{local}(x)/f_B^{local}(x)$ changes as

$$\frac{\tilde{f}(x(t)) - \tilde{f}(x(t_0))}{\tilde{f}(x(t_0))} = (\beta_A - \beta_B)\,[U(x(t)) - U(x(t_0))] \,. \tag{3.41}$$

Therefore, by comparing the frequencies of the clocks over the course of a year, we can obtain a measurement of $(\beta_A - \beta_B)$. Currently, state-of-the-art experiments constrain this ratio at the 10^{-7} level [15], which results in the following limits,

$$D_e \lesssim 10^{-8}, \quad D_{m_e} \lesssim 10^{-6}, \quad D_{\hat{m}} \lesssim 10^{-6} \,. \tag{3.42}$$

From Fig. 3.1, we see that the limits from this class of atomic clock experiments are currently at least 3 orders of magnitude weaker than the direct limits from fifth force measurements in the $(D_e, D_{\hat{m}})$ parameter space.

We now turn our attention to gravitational redshift measurements. As Eq. (3.25) suggests, β_A can be determined by comparing two identical spatially separated clocks, as illustrated in Fig. 3.3. This approach is also not new. The first successful realization of this method was achieved by Gravity Probe - A [125], where the frequency of a microwave clock on a satellite was compared with the frequency of an identical clock on earth via microwave link as the satellite was changing altitude. After accounting for special and general relativistic effects, the measured frequency was transformed to the local frame of satellite leading to a constraint on the anomalous redshift via the relation,

$$\frac{f_A^{local}(x) - f_A^{local}(x_\oplus)}{f_A^{local}(x_\oplus)} = \beta_A \left[U(x) - U(x_\oplus) \right] , \tag{3.43}$$

where $x_\oplus$ denotes the position of the clock on earth.

This experiment constrained β_A at the level of 10^{-4}. Although this bound was later improved by an order of magnitude by the Galileo satellite [126], it remains many orders of magnitude below the strongest limits from direct fifth force searches.

3.3 Experimental prospects

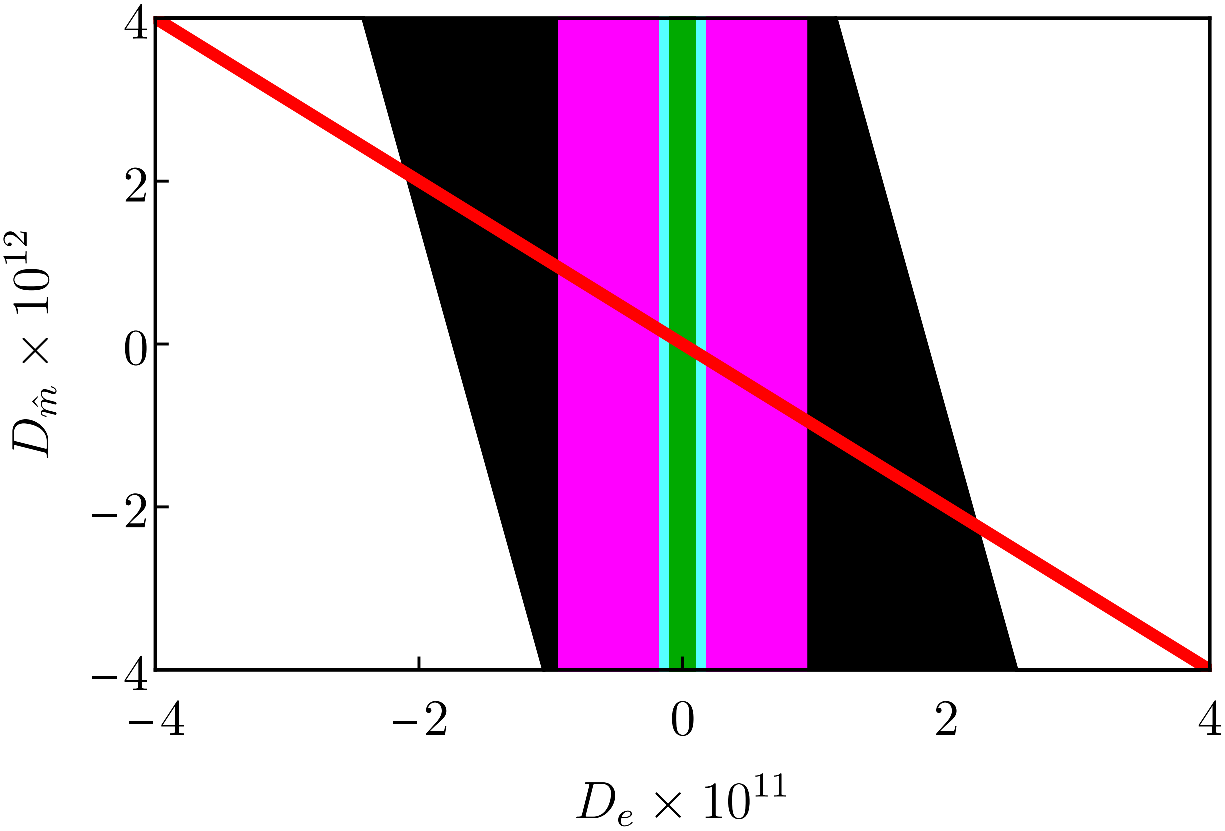

Figure 3.4: In the $D_{\hat{m}}$ vs. D_e plane, we show how the projected limits from future earth and space based differential redshift experiments compare against the current bounds from direct fifth force searches. The black region represents the current bound set by MICROSCOPE [2, 12]. The magenta and light cyan lines show the projected sensitivity of the SpaceQ experiment [14] while traveling towards the $r = 0.39$ AU and $r = 0.1$ AU orbits respectively, assuming that the satellite is equipped with two optical clocks with $\Delta K_\alpha = 7$ and $\Delta\tilde{f}/\tilde{f} = 10^{-18}$. The green band shows the projected sensitivity of an earth based experiment based on two optical clocks with $\Delta K_\alpha = 7$, $\Delta K_q = 0$ and $\Delta\tilde{f}/\tilde{f} = 10^{-21}$. The red line shows the bound that could be set by an earth based nuclear clock - optical clock system, with $\Delta K_\alpha = 10^4$, $\Delta K_q = 10^5$ and $\Delta\tilde{f}/\tilde{f} = 10^{-18}$.

3.3.1 Two Different Clocks at the Same Location

In order to match the sensitivity of the direct fifth force searches by the MICROSCOPE experiment [2, 12], the uncertainty in the frequency of optical clocks located on earth needs to be of order $\Delta\tilde{f}/\tilde{f} \sim 10^{-21}$ for $\Delta K_\alpha = 7$. This requires an improvement by about 3 orders of magnitude over the best precision available at this time, which is expected to occur within the next two decades [16].

However, improved precision is not the only option. Clocks based on nuclear transitions offer the exciting prospect of measuring the variation of fundamental constants with unprecedented sensitivity [131]. The nuclear clock based on the ^{229}Th nucleus is expected to have sensitivity to the variation of the fine structure constant about 3 orders of magnitude better than the best optical clock, $K_\alpha \sim 10^4$, while the sensitivity to the masses of the quarks is expected to be even greater, $K_q \sim 10^5$ [132]. Because of the large K_q, nuclear clocks of this type with an uncertainty of $\Delta\tilde{f}/\tilde{f} \sim 10^{-18}$ would be sufficient to improve on the current bounds set by the MICROSCOPE experiment. This is shown in Figs. 3.4, 3.5, 3.6 , and 3.7.

Another possibility is to conduct an experiment in space. By sending the two clocks closer to the sun we can take advantage of the larger gravitational potential to increase the sensitivity to $(\beta_A - \beta_B)$. SpaceQ is a recent proposal based on this strategy [14]. The satellite would be equipped with a two-clock system, and the frequency ratio between the clocks as the satellite orbits the sun would be measured. The first stage of the experiment proposes to send a satellite to Mercury's orbit, which is at $r = 0.39$ AU. The second stage could reach down to $r = 0.1$ AU. In both these stages the satellite's orbit is designed to be circular, which means that during the main stage of the experiment EP violating effects would not be measurable. However, as pointed out in the proposal, data can also be taken as the satellite transits towards its final orbit, allowing us to measure EP violating effects. In reaching the $r = 0.1$ AU orbit, the satellite would experience a change in the gravitational potential of the order of $\Delta U \sim 10^{-7}$, which is greater than the annual modulation of the gravitational potential on earth by a factor of nearly 300. In Fig.

3.6 we illustrate the sensitivity of this proposal to d_e in four different scenarios. In the first case a satellite is sent out to Mercury's orbit containing two optical clocks. In the second case, one of the optical clocks is replaced by a nuclear clock. In the third and fourth cases a satellite is sent to orbit the sun at $r = 0.1$ AU with an optical-optical and a nuclear-optical clock system respectively. In all versions of the experiment we assume a fractional uncertainty of $\Delta\tilde{f}/\tilde{f} \sim 10^{-18}$. We see that the use of nuclear clocks leads to great improvements over the current sensitivity.

3.3.2 Identical Spatially Separated Clocks

The FOCOS experiment [16] proposes to place a satellite carrying an optical clock in an elliptical orbit around the earth. The clock on the satellite will communicate with an identical clock on earth via optical links as the satellite approaches its apogee and perigee. Since the distance between the surface of the earth and the satellite will vary between 5000 km and 22500 km, the satellite will experience a large variation in the earth's gravitational potential, allowing for an accurate determination of β_A. The optical clock offers more stability and precision than the microwave clocks that were used in earlier satellites. Instead of continuous monitoring of the frequency ratio, the experiment would monitor the phase difference between the clocks which can be translated into a frequency difference. This ultimately can be transformed into a limit on β_A using Eq. (3.43). The experiment aims to measure β_A with an accuracy of 10^{-9}.

As explained in Sec. 3.2.2, the bound on the anomalous redshift can be translated into bounds on the parameters D_x and d_x through Eq. (3.32). Since the proposal did not specify the clocks that would be used on the mission, we will consider two scenarios. In the first scenario, the satellite is equipped with an optical clock based on the electric octopole transition (E3) of

$^{171}Yb^+$, which has the highest realized sensitivity to the variation of the fine structure constant, $K_\alpha = -6$ [132]. In the second scenario, we consider a satellite with a nuclear clock that has a sensitivity of $K_\alpha \sim 10^4$. The expected experimental reach of these two versions of the FOCOS experiment for the couplings d_e, d_g, d_{m_e} and $d_{\hat{m}}$ is presented in Figs. 3.6, 3.7, 3.8 and 3.9. Remarkably, we see from Fig. 3.8 that with even with existing clock technology the FOCOS experiment would be competitive with the currents bounds on d_{m_e} from direct fifth force searches. However, to improve on the current limits on d_e, d_g and $d_{\hat{m}}$ would require the use of nuclear clocks.

It follows from this discussion that, when it comes to fifth forces mediated by scalars that couple primarily to electrons, satellite-based clock experiments can already compete with direct fifth force searches. The reason why this particular coupling is where clocks first start to gain ground is because the frequencies associated with most atomic transitions are directly proportional to m_e, and so they are very sensitive to changes in the electron mass. In contrast, in direct fifth force searches, the electron only contributes a small amount to the mass of any given atom and so these experiments are inherently less sensitive to forces that act primarily on electrons.

3.4 Conclusions

In this chapter, we have explored how clock based experiments offer an alternative approach to probing EP violating fifth forces mediated by ultralight scalars. The same scalar field that mediates the fifth force will, in general, also give rise to position dependence in the fundamental parameters. Clocks on the earth as it orbits the sun or clocks on satellites orbiting the earth are sensitive to this effect, and therefore provide an excellent opportunity to test this class of models. The sensitivity of clock based experiments can be compared against the limits from direct fifth force searches, providing a benchmark to aim for when designing these experiments.

We have considered two classes of experiments utilizing clocks. The first class of experiments we studied were differential measurements where two different clock transitions were being compared at the same location. These experiments, performed on earth or in space, have the potential to probe beyond the current limits but require clocks more sensitive than currently available. The second class of experiments are anomalous redshift measurements where a clock in an elliptical orbit around the earth is compared to a clock on earth. Experiments along these lines utilizing current clock technology can place constraints on fifth forces that act primarily on electrons that are competitive with current constraints. Future nuclear clocks in elliptical orbits would offer a significant improvement in sensitivity to several different couplings.

The rapid experimental progress in clock technology has been quite remarkable. Their sensitivity has been consistently improving by an order of magnitude every few years for the past several decades. Our analysis shows that if this rate of improvement is maintained, clock experiments may soon offer the greatest sensitivity to EP violating fifth forces mediated by ultralight scalar fields.

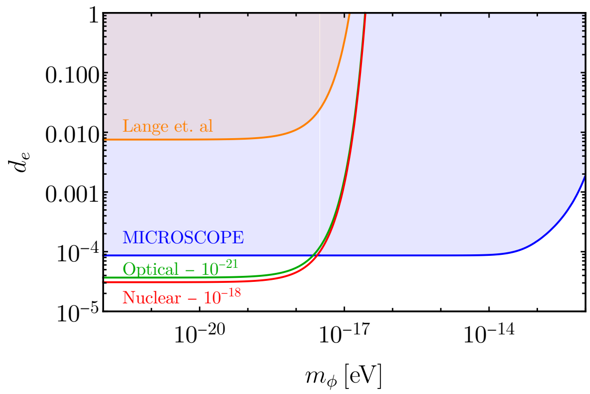

Figure 3.5: In the d_e vs. m_ϕ plane, we show how the projected limits from future earth based two-clock experiments compare against the current bounds from direct fifth force searches. The orange region represents the current bounds from atomic clock experiments [15]. The blue region shows the parameter space excluded by the MICROSCOPE experiment [2, 12]. The green line depicts the projected limit from a future Earth based experiment involving two optical clocks with $\Delta K_\alpha = 7$ and $\Delta\tilde{f}/\tilde{f} = 10^{-21}$. The red line shows the projected sensitivity of an Earth based two-clock experiment involving a nuclear clock with $\Delta K_\alpha = 10^4$ and $\Delta\tilde{f}/\tilde{f} = 10^{-18}$.

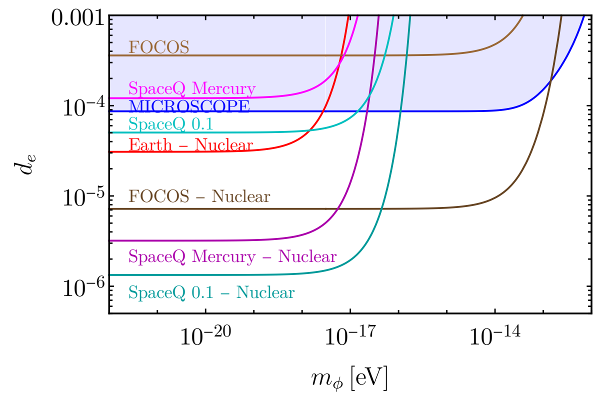

Figure 3.6: In the d_e vs. m_ϕ plane we show how the projected limits from future experiments compare against the current bound from direct fifth force searches. The blue region shows the parameter space excluded by the MICROSCOPE experiment [2, 12]. The red line shows the sensitivity of an Earth based two-clock experiment involving a nuclear clock with $\Delta K_\alpha = 10^4$ and $\Delta\tilde{f}/\tilde{f} = 10^{-18}$. The brown and dark brown lines show the potential reach of the FOCOS experiment [16], assuming that the satellite is equipped with an optical clock with $K_\alpha = -6$ or a nuclear clock with $K_\alpha = 10^4$ respectively and measures the redshift with the accuracy of $\beta = 10^{-9}$. The magenta and cyan lines depict the sensitivity of the SpaceQ mission [14] while traveling towards the $r = 0.39$ AU and $r = 0.1$ AU orbits respectively, assuming that the satellite is equipped with two optical clocks with $\Delta K_\alpha = 7$ and $\Delta\tilde{f}/\tilde{f} = 10^{-18}$. The dark magenta and dark cyan lines depict the ultimate sensitivities of the SpaceQ experiment while traveling towards the $r = 0.39$ AU and $r = 0.1$ AU orbits respectively, when the satellite is equipped with a nuclear-optical clock system with $\Delta K_\alpha = 10^4$ and $\Delta\tilde{f}/\tilde{f} = 10^{-18}$.

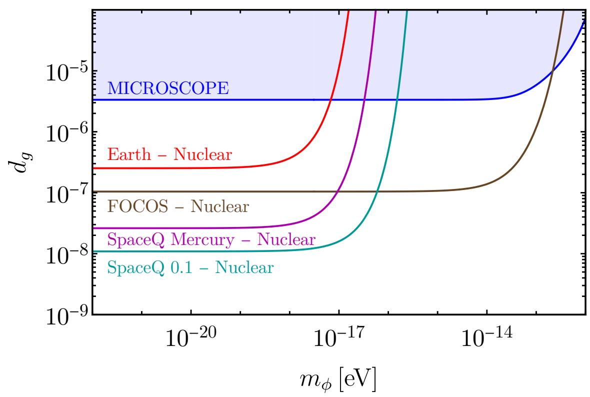

Figure 3.7: In the d_g vs. m_ϕ plane we show how the projected limits from future clock based experiments compare against the current bounds on fifth forces. The blue region shows the parameter space excluded by the MICROSCOPE experiment [2, 12]. The red line depicts the projected sensitivity of an Earth based two-clock experiment involving a nuclear clock, the dark brown line shows the projected reach of the space based FOCOS experiment equipped with a nuclear clock, while the dark magenta and dark cyan lines project the sensitivities of the SpaceQ experiment assuming that the satellite reaches $r = 0.39$AU and $r = 0.1$AU respectively and is equipped with nuclear clocks. We take $\Delta K_q = 10^5$ and $\Delta\tilde{f}/\tilde{f} = 10^{-18}$ for all clock pairs except for the FOCOS experiment where we assume $\beta = 10^{-9}$.

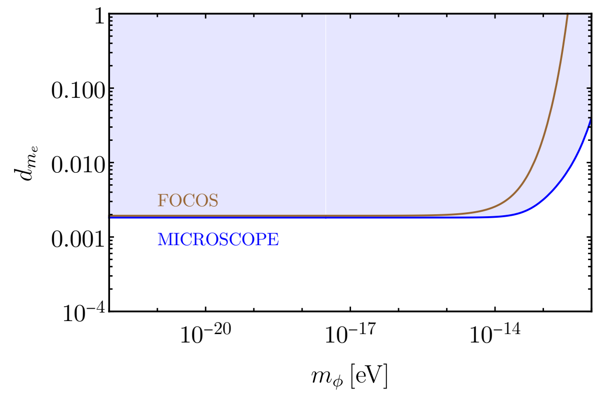

Figure 3.8: In the d_{m_e} vs. m_ϕ plane we show how the projected limit from the future space based FOCOS experiment compares against the current bound. The blue region shows the parameter space excluded by the MICROSCOPE experiment [2, 12] while the brown line shows the reach of the FOCOS experiment [16] assuming that the satellite is equipped with an optical clock with $K_\alpha = -6$ and the redshift is measured with the accuracy of $\beta = 10^{-9}$.

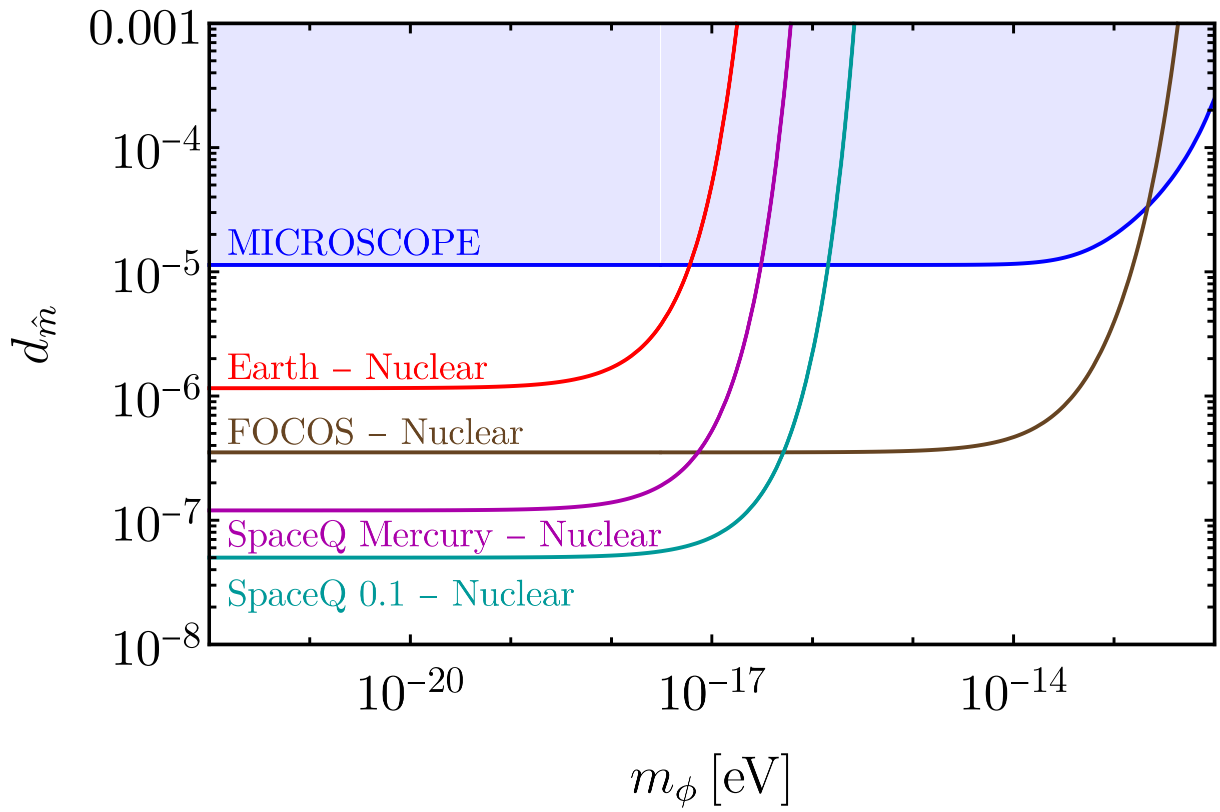

Figure 3.9: In the $d_{\hat{m}}$ vs. m_ϕ plane, we show how the projected limits from future clock based experiments compare against the current bounds from direct fifth force searches. The blue region shows the parameter space excluded by the MICROSCOPE experiment [2, 12]. The red line gives the sensitivity of an Earth based two-clock experiment involving a nuclear clock, the dark brown line depicts the reach of the space based FOCOS experiment equipped with a nuclear clock while the dark magenta and dark cyan lines project the sensitivities of the space based SpaceQ experiment assuming that the satellite reaches $r = 0.39$AU and $r = 0.1$AU respectively and is equipped with a nuclear clock. We assume $\Delta K_q = 10^5$ and $\Delta\tilde{f}/\tilde{f} = 10^{-18}$ for all clock pairs except for the FOCOS experiment where we assume $\beta = 10^{-9}$.

Chapter 4: Constraining Vector Dark Matter with Neutrino experiments

4.1 Introduction

In this chapter, we move on from scalar fields to vector dark matter and discuss experimental prospects of measuring vector dark matter with neutrino experiments.

A background of $U(1)_{L_\mu-L_\tau}$ ($U(1)_{L_e-L_\mu}$) gauge bosons acts as a time-dependent potential that is flavor non-universal. As neutrinos and antineutrinos have opposite charges, the potential is opposite for matter and antimatter. Additionally, the effect is proportional to the dot product of the neutrino velocity with the polarization of dark matter resulting in a directionally dependent chemical potential. If the dark matter oscillations are slow compared to the neutrino propagation timescale, the effect on neutrino oscillations is similar to the MSW matter effect [133–135]. Therefore, the main signature of these models are time-dependent neutrino oscillation parameters, e.g. $\Delta m^2_{31}(t)$ and $\sin\theta_{13}(t)$. Measurement of these signatures might be challenging due to a low neutrino event rate. However, we show that even after averaging over the duration of the experiment, the effect is strong enough to place bounds several orders of magnitude better than the leading bounds on $U(1)_{L_e-L_\mu}$ and $U(1)_{L_\mu-L_\tau}$ dark matter. Similar bounds on $U(1)_{L_\mu-L_\tau}$ from neutrino oscillation experiments were estimated in [66] and [136]. The former studied the effect of neutrino-DM scattering, while the latter considered the scenario where the vector field is a relic field used to facilitate the production of sterile neutrino dark matter in the early universe.

If the dark matter oscillations are fast compared to the neutrino propagation timescale, the neutrinos experience a rapidly oscillating effective chemical potential. Because this potential oscillates rapidly, to the lowest order the effective potential averages to zero over the neutrino propagation time. Thus, the leading effects are suppressed by an additional factor of m^{-1}, where m is the oscillation rate of the background dark matter field. The fact that our bounds on $U(1)_{L_e-L_\mu}$ and $U(1)_{L_\mu-L_\tau}$ scale by an additional factor of m^{-1} in the high mass regime reflects this chemical potential washout effect.

The goal of this chapter is to explore the sensitivity of various neutrino oscillation experiments to VDM with flavor non-universal couplings to leptons. In section 4.2, we review the phenomenology of neutrino oscillations and introduce the effect of vector DM on neutrino oscillations. In section 4.3, we constrain the model using existing and planned neutrino experiments. We conclude with section 4.4 and propose further avenues of research.

4.2 Model

We start with a brief description of gauging lepton flavor and its effect on neutrinos. The three individual lepton flavor numbers $L_\alpha,\ \alpha = e, \mu, \tau$, can be equivalently described in a different basis comprising the total lepton number $\sum_\alpha L_\alpha = L$ and two lepton number differences, which we choose to be $L_e - L_\mu$ and $L_\mu - L_\tau$ without any loss of generality. The total lepton number charge L is the identity in the flavor space and gives an equal phase to neutrinos of all flavors and hence is unobservable in neutrino oscillations. Therefore we restrict our discussion to $L_e - L_\mu$ and $L_\mu - L_\tau$.

To the Standard Model, we add a single gauge boson $A_{d\mu}$ which gauges either of the two flavor lepton number differences.

$$\begin{aligned}
&\mathcal{L} \subset -\frac{1}{4}F_{d\,\mu\nu}F_{d}^{\mu\nu} - \frac{1}{2}m_A^2 A_{d\,\mu}A_d^{\mu} + \mathcal{L}_{int,e-\mu} + \mathcal{L}_{int,\mu-\tau} \\
&\mathcal{L}_{int,e-\mu} = -gA_{d\,\sigma}\left(\overline{l_e}\gamma^{\sigma}l_e - \overline{l_\mu}\gamma^{\sigma}l_\mu\right) \\
&\mathcal{L}_{int,\mu-\tau} = -g'A_{d\,\sigma}\left(\overline{l_\mu}\gamma^{\sigma}l_\mu - \overline{l_\tau}\gamma^{\sigma}l_\tau\right)
\end{aligned} \tag{4.1}$$

where m_A is the mass of the gauge field, g and g' denote coupling to the $L_e - L_\mu$ and $L_\mu - L_\tau$ charges respectively and $l_{e,\mu,\tau}$ denotes leptons with e, μ, τ charges. For example, l_e denotes electrons, electron neutrinos and their anti-particles.

We now consider the consequences of the vector boson $A_{d\,\mu}$ being dark matter. The three polarizations of a massive gauge field satisfy $p_\mu \epsilon^\mu = 0$. If the gauge bosons were at rest, the three polarizations would simply be unit vectors in the x, y, and z directions. Including a non-zero velocity along the z-axis and considering the longitudinal polarization $\epsilon_L = \frac{1}{m_A}(p, 0, 0, E)$ we see that the temporal component of the vector field $A_{d\,0}$ is subdominant to the spatial components $A_{d\,i}$ by a factor of DM velocity $v_{DM} \sim 10^{-3}$. To leading order the galactic DM field can be written as an oscillating three vector with frequency $\omega \sim m_A + \mathcal{O}(v_{DM}^2)$

$$\vec{A}_d = \vec{A}_0 \cos\left(m_A(t + \vec{v}_{DM}\cdot\vec{x}) + \phi\right) + \mathcal{O}(v_{DM}^2), \tag{4.2}$$

where $|\vec{A}_0| = \sqrt{2\rho_{DM}/m_A^2}$ and m_A is the mass of the DM. Since the neutrinos are relativistic, the interactions in Eq. 4.1 can be written for neutrinos as

$$H_{\text{int}} = \vec{A}_d \cdot \vec{v}_\nu \begin{pmatrix} g & 0 & 0 \\ 0 & g' - g & 0 \\ 0 & 0 & -g' \end{pmatrix} + \mathcal{O}(v_{DM}) \tag{4.3}$$

where $\vec{v}_\nu$ is the neutrino velocity. The dark matter shifts the relative energies of different neutrino flavor eigenstates. For example, in the case where the dark matter is the gauge boson of $L_e - L_\mu$, the dark matter creates an energy difference between the electron neutrino ν_e and muon neutrino ν_μ. The vector nature of the interaction means it has opposite signs for neutrinos and anti-neutrinos. The dark matter thus acts as a chemical potential for the neutrinos. This can be contrasted with the effect of a scalar field which does not distinguish between particles and antiparticles.

It is important to note the directional dependence of the interaction. The interaction picks the polarization of the DM along the neutrino velocity. In neutrino beam experiments, where the neutrino velocity has a fixed orientation with respect to the earth's frame, the direction of the neutrino velocity rotates with the earth over the course of a day. This produces a daily modulation of the DM effect. This is in contrast with the effect produced by a scalar field where no such directional dependence exists and can be used to distinguish between the two. We explore this effect in more detail in Sec. 4.2.3

4.2.1 Neutrino Oscillations

Within the Standard Model, neutrino oscillations are controlled by two contributions, the vacuum Hamiltonian H_{vac} and the MSW effect [133, 134]. In absence of any matter, the neutrino oscillation is set by the neutrino energy, the mass squared difference and the rotation matrix between the mass and the flavor eigenstates, U_{PMNS}. In the relativistic limit, we can expand the Hamiltonian in powers of m_ν/E_ν where m_ν denotes the mass of a generic mass eigenstate and E_ν is the neutrino energy. The non-identity piece of the vacuum Hamiltonian can be written as

$$H_{\text{vac}} = U_{PMNS}\left[\frac{1}{2E_\nu}\begin{pmatrix}0 & 0 & 0\\ 0 & \Delta m^2_{21} & 0\\ 0 & 0 & \Delta m^2_{31}\end{pmatrix}\right]U^\dagger_{PMNS} \tag{4.4}$$

where $\Delta m^2_{ij} = m^2_i - m^2_j$ are the neutrino mass differences and we have removed the pieces proportional to the identity that do not contribute to oscillations.

On the other hand, in the presence of matter, for example while propagating through the earth, the interaction of the neutrinos with matter creates a chemical potential for the neutrinos. In the presence of protons, neutrons and electrons, the only non-identity interaction in flavor space is a chemical potential for the electron neutrinos.

$$H_{\text{MSW}} = \pm\sqrt{2}G_F n_e(x)\begin{pmatrix}1 & 0 & 0\\ 0 & 0 & 0\\ 0 & 0 & 0\end{pmatrix} \tag{4.5}$$

where G_F is the Fermi constant, $n_e(x)$ is the number density of electrons and the + (−) sign is for neutrinos (anti-neutrinos). The neutrino oscillations we observe in neutrino experiments are an interplay between the vacuum oscillation and the effect of matter. Experiments that are sensitive to this effect work in the regime $L\Delta m_{21}^2/E_\nu \ll 1$, despite the long distance traveled by neutrinos $L \sim 10^3 - 10^4$ km. As a result, the relevant mixing parameters are reduced to Δm_{31}^2, θ_{13} and θ_{23}. When there is a non-zero number density of electrons, Δm_{31}^2 and θ_{13} are replaced by their effective counterparts [135]

$$\Delta m_{31,M}^2 = \Delta m_{31}^2 \sqrt{(\cos 2\theta_{13} - \Gamma)^2 + \sin^2 2\theta_{13}} \tag{4.6}$$

$$\sin^2 2\theta_{13,M} = \frac{\sin^2 2\theta_{13}}{(\cos 2\theta_{13} - \Gamma)^2 + \sin^2 2\theta_{13}} \tag{4.7}$$

where $\Gamma = \sqrt{2} G_F n_e E_\nu / \Delta m_{31}^2$. When $\Gamma = \cos 2\theta_{13}$, magnitudes of H_{vac} and H_{MSW} are comparable, which significantly changes mass eigenstates. This leads to enhanced oscillations into electron neutrinos at distances of order $\frac{E\nu}{\Delta m_{31,M}^2}$, which we call resonance.

The effect has important phenomenological consequences. The sign of Γ changes between neutrinos and antineutrinos, and also depends on mass ordering. In the normal ordering, the resonance can only happen for neutrinos, while in the inverted ordering it can only occur for antineutrinos. Therefore, the resonance can be used to solve the mass ordering problem [135].

In the presence of vector dark matter, neutrino oscillations are modified in a similar way.

The dark matter contribution (Eq. 4.1) to the neutrino oscillation can be written as[1]

$$H_{\text{int}} = \pm\frac{\sqrt{2\rho}}{m_A}\cos(m_A t+\phi)\cos\alpha(t)\begin{pmatrix} g & 0 & 0 \\ 0 & g'-g & 0 \\ 0 & 0 & -g' \end{pmatrix} \tag{4.8}$$

where g and g' denote coupling to the $L_e - L_\mu$ and $L_\mu - L_\tau$ charges respectively, ρ is the DM energy density, m_A is the mass of the vector DM and $\alpha(t)$ is the angle between DM polarization and the neutrino velocity. The total Hamiltonian governing neutrino oscillations is the sum of the parts

$$H = H_{\text{vac}} + H_{\text{MSW}} + H_{\text{int}}. \tag{4.9}$$

In order to see the effect of the VDM is similar to the matter effect, let us set $g = 2g'$. Then, the non-identity piece of H_{int} has the same matrix structure as Eq. (4.5). In the $L\Delta m^2_{21}/E_\nu \ll 1$ limit this leads to a time-dependence of the effective Δm^2_{31} and θ_{13}

$$\Delta m^2_{31,DM} = \Delta m^2_{31}\sqrt{(\cos 2\theta_{13} - \Gamma - \Gamma_{DM}(t))^2 + \sin^2 2\theta_{13}} \tag{4.10}$$

$$\sin^2 2\theta_{13,DM} = \frac{\sin^2 2\theta_{13}}{(\cos 2\theta_{13} - \Gamma - \Gamma_{DM}(t))^2 + \sin^2 2\theta_{13}} \tag{4.11}$$

where $\Gamma_{DM}(t) = \frac{3g\sqrt{\rho}E_\nu}{\sqrt{2}m\Delta m^2_{31}}\cos(mt+\phi)\cos\alpha(t)$. Therefore, we can see that experiments which are sensitive to the matter effect should also be able to measure the effect caused by DM. The only

[1]Although the DM phase changes both in space and time, as in Eq. 4.2, the neutrino baseline is much smaller than the coherence length so that the change in phase is suppressed by the small DM velocity. Hence we only keep the leading time-dependent piece.

qualitative difference is that in this scenario the time-averaged effect is the same for neutrinos and anti-neutrinos, which is a feature that could be used to differentiate the DM-induced effect from the matter effect.

4.2.2 Simplified model with two flavors

To gain some insight into the effect of vector dark matter on neutrino oscillation, we consider a toy model of two neutrino flavors. For clarity, we ignore the matter effect as it does not affect our conclusions. The model is characterized by a single neutrino mass squared difference, which we denote by Δm^2, the neutrino energy E_ν and the dark matter mass and coupling, m_A and g.

$$\begin{aligned} H &= U\frac{\Delta m^2}{4E_\nu}\sigma_z U^\dagger + \frac{g\sqrt{2\rho}}{m_A}\sigma_z\cos(m_A(t-t_0)+\phi(t_0)) + \mathcal{O}(v_{\rm DM}) \\ &= U\Delta_\nu\sigma_z U^\dagger + gA_0\sigma_z\cos(m_A(t-t_0)+\phi(t_0))\,, \end{aligned} \tag{4.12}$$

where σ_z is the third Pauli Matrix, U is the PMNS matrix for two flavors, $\Delta_\nu \equiv \frac{\Delta m^2}{4E_\nu}$ controls the neutrino vacuum Hamiltonian, $A_0 = \frac{\sqrt{2\rho}}{m_A}$ is the vector amplitude, $\phi(t_0) = m_A t_0 + \phi_0$ is the DM phase at the point of neutrino production and t_0 denotes the time of neutrino production. We have also neglected the dot product of the polarization and the neutrino velocity which changes due to earth's rotation. We discuss this effect in detail in Sec. 4.2.3.

Let us first consider the time dependence of the DM effect. Due to stringent constraints, the DM effect is subdominant to the vacuum oscillation and can be treated using perturbation theory.

The transition probability between the flavor states can be written as

$$P_{\nu_e \to \nu_\mu} = P^{(0)} + P^{(1)} + P^{(2)} + \cdots, \tag{4.13}$$

where we have labeled the two flavor states as ν_e and ν_μ, $P^{(1)}$ and $P^{(2)}$ are the first and second order correction to the oscillation probability due to dark matter, $P^{(n)} \propto g^n$. The first order correction, $P^{(1)}$, only contains contributions as $\sin(m_A L + \phi(t_0))$, where L denotes the baseline of the experiment. This term oscillates as the initial phase $\phi(t_0)$ changes as a function of neutrino production time t_0. If an experiment has sufficient statistics, they can look for the oscillating first-order correction. On the other hand, if the experiment only observes time-averaged quantities, we will instead be sensitive to the second order correction, $P^{(2)}$, which includes terms like $\sin^2(m_A L + \phi(t_0))$. These do not average to zero in contrast with the first-order correction. Then,

$$\langle P_{\nu_e \to \nu_\mu} \rangle = P^{(0)} + \langle P^{(2)} \rangle + \cdots, \tag{4.14}$$

where $\langle \rangle$ denotes averaging over the lifetime of the experiment. We compute $\langle P^{(2)} \rangle$ using time-dependent perturbation theory.

$$
\begin{aligned}
\langle P^{(2)} \rangle &= -\frac{g^2 A_0^2 \sin^2(2\theta)}{\left(m_A^3 - 4m_A\Delta_\nu^2\right)^2} f(m_A, \Delta_\nu, L) \\
f(m_A, \Delta_\nu, L) &= 8\Delta_\nu^4 \cos^2(2\theta) \left(\cos\left(L\left(m_A + 2\Delta_\nu\right)\right) + \cos\left(L\left(m_A - 2\Delta_\nu\right)\right) - 2\cos\left(2L\Delta_\nu\right)\right) \\
&+ m_A^4 \left(L\Delta_\nu \sin^2(2\theta) \sin\left(2L\Delta_\nu\right) + 2\cos^2(2\theta)\sin^2\left(L\Delta_\nu\right)\right) + 16 m_A \Delta_\nu^3 \cos^2(2\theta) \sin\left(L m_A\right) \sin\left(2L\Delta_\nu\right) \\
&+ m_A^2 \Delta_\nu^2 \left(\cos(4\theta)\left(\cos\left(L\left(m_A + 2\Delta_\nu\right)\right) + \cos\left(L\left(m_A - 2\Delta_\nu\right)\right) - 2\cos\left(L m_A\right) + 6\cos\left(2L\Delta_\nu\right) - 6\right)\right) \\
&+ m_A^2 \Delta_\nu^2 \left(\cos\left(L\left(m_A + 2\Delta_\nu\right)\right) + \cos\left(L\left(m_A - 2\Delta_\nu\right)\right) + 2\cos\left(L m_A\right)\right) \\
&+ m_A^2 \Delta_\nu^2 \left(-4L\Delta_\nu \sin^2(2\theta)\sin\left(2L\Delta_\nu\right) + 2\cos\left(2L\Delta_\nu\right) - 6\right),
\end{aligned}
\tag{4.15}
$$

where θ characterizes the two flavor PNMS matrix U.

This very complicated expression can be greatly simplified in the large or small m_A limits. In the small mass limit, where $m_A \ll 1/L \sim \Delta_\nu$, the effect of dark matter is roughly constant as the neutrinos fly from the point of production to the point of detection. In this limit, the leading correction to the vacuum oscillation is given by

$$
\begin{aligned}
\langle P^{(2)} \rangle &= g^2 \frac{A_0^2 \sin^2 2\theta}{8\Delta_\nu^2} \qquad (4.16) \\
&\left(4\cos 4\theta + 2\cos(2\Delta_\nu L)\left(\cos 4\theta(\Delta_\nu^2 L^2 - 2) + \Delta_\nu^2 L^2 - 1\right) - \Delta_\nu L(5\cos(4\theta) + 3)\sin(2\Delta_\nu L) + 2\right).
\end{aligned}
$$

On the other hand in the large mass limit, where $m_A \gg 1/L \sim \Delta_\nu$, the dark matter is oscillating rapidly over the flight of the neutrinos and much of its effect is averaged away. In this limit, the same second-order correction reads

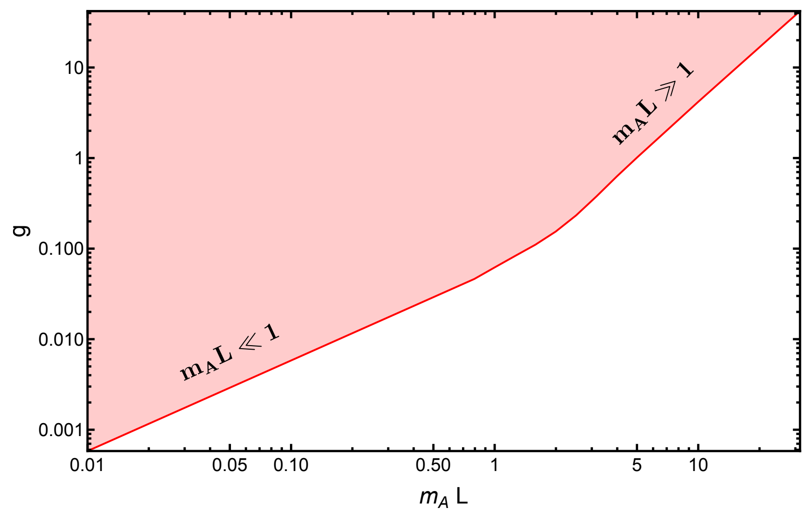

Figure 4.1: We show how the bound on the dark matter gauge coupling as a function of mass is expected to behave for hypothetical neutrino oscillation experiments. For $m_A L \ll 1$, for a fixed experimental uncertainty, the coupling scales linearly with m_A whereas for $m_A L \gg 1$, the same scaling is quadratic.

$$\langle P^{(2)} \rangle = -g^2 \frac{A_0^2 \sin^2 2\theta}{m_A^2} \left(\Delta_\nu L \sin^2(2\theta) \sin(2\Delta_\nu L) + 2\cos^2(2\theta) \sin^2(\Delta_\nu L) \right) \tag{4.17}$$

From Eq. 4.16 and 4.17, it is easy to see how the bound on the dark matter coupling constant g scales with the mass of dark matter. In the low mass regime, $\sqrt{P^{(2)}} \sim gA_0 \sim \frac{g}{m_A}$, so we expect the constraint to scale as $g \propto m_A$. On the other hand, in the high mass regime, $\sqrt{P^{(2)}} \sim \frac{gA_0}{m_A} \sim \frac{g}{m_A^2}$. Hence the constraint is expected to scale as $g \propto m_A^2$. This scaling behavior can be seen in Fig. 4.1 where we have plotted the bound obtained from a hypothetical neutrino experiment using two neutrino flavors in the perturbative regime. In making this plot, we have assumed $\Delta_\nu \in [1., 2.]$, a fixed experimental uncertainty and considered 10 bins with equal energy spacing (motivated by the DUNE experiment [19, 137, 138]). The difference in the scaling of the bound on the coupling constant is clearly different in the small and large mass ranges. In the low mass regime, $m_A L \ll 1$, the bound increases slowly $g \propto m_A$. On the other hand, in the high mass regime $m_A L \gg 1$ it weakens faster, $g \propto m_A^2$ and smoothly transitions between the two at $m_A L \sim 1$.

In Section 4.3.3, we will use these perturbative results to scale numerically obtained bounds at one mass to other masses. To do this, we will need to be sure that we are in the perturbative regime. We will look at experiments with neutrino energies $E_\nu \sim \mathcal{O}(1-10\,\mathrm{GeV})$ at which scale Δm_{13}^2 dominates the oscillation dynamics. By demanding $P^{(2)} \ll 1$, Eq. 4.16 gives a bound on the coupling below which we are working in the perturbative regime.

$$g < 2.5 \cdot 10^{-30} \left(\frac{m_A}{10^{-20}\mathrm{eV}}\right)\left(\frac{\mathrm{GeV}}{E_\nu}\right) \tag{4.18}$$

4.2.3 Daily Modulation

In this section, we discuss the effects of the earth's rotation on our DM signal. In particular, we show that the effect of daily modulation does not erase the DM signal even after time-averaging, which motivates the search for time-independent signatures of the signal.

As the DM-induced potential is the dot product between the DM polarization and neutrino velocity, the DM-induced potential undergoes an oscillation due to the earth's rotation. The equatorial component oscillates whereas the polar components remain unchanged due to the earth's rotation. This directional dependence is a crucial difference between vector and scalar DM.

For a neutrino beam type experiment, the neutrino beam has a fixed direction in the lab frame. Figure 4.2 shows this in the lab frame. In general, the neutrino beam has a direction

$$\hat{v}_\nu = (v_{||},\ \ v_\perp) \tag{4.19}$$

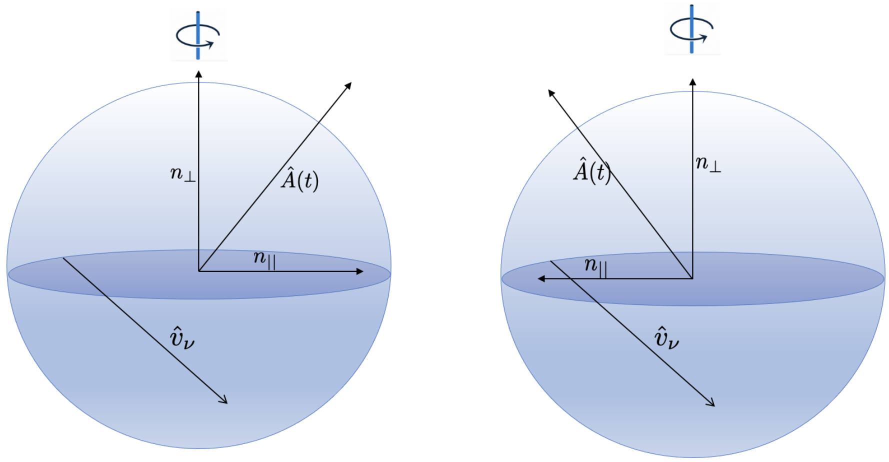

Figure 4.2: The equatorial component of the vector polarization $n_{||}$ rotates in the lab frame due to the earth's rotation whereas the polar component $n_\perp$ remains unchanged. For experiments like DUNE, the neutrino velocity has a fixed direction. Hence the angle between the vector polarization and the neutrino velocity oscillates with the frequency of a day.

where $v_{||}$ and $v_\perp$ are the equatorial and polar components of the neutrino velocity respectively. We can similarly write the dark matter polarization unit vector in the lab frame as

$$\hat{A}(t) = (n_{||}\cos(\omega_d t),\ \ n_\perp), \tag{4.20}$$

where $n_{||}$ and $n_\perp$ are the equatorial and polar components of the vector polarization and ω_d is the daily frequency. We can write the vector DM potential, Eq. 4.8,

$$H_{\text{int}} = \frac{\sqrt{2\rho}}{m_A}\cos(m_A t + \phi)\cos\alpha(t)\begin{pmatrix} g & 0 & 0 \\ 0 & g' - g & 0 \\ 0 & 0 & -g' \end{pmatrix} \tag{4.21}$$

$$\cos\alpha(t) = \hat{A}(t)\cdot\hat{v}_\nu. \tag{4.22}$$

In an experiment with high statistics, we can make out the daily modulation of the signal. In absence of such opportunity, we can observe the time averaged effect of the daily modulation.

The daily average removes the first order correction $\langle P^{(1)} \rangle = 0$ and only the higher order effects remain observable. In the case of sufficiently light DM, $m_A \ll \omega_d$, averaging over a day does not average over a full oscillation of DM. In that case, the oscillation of the DM effect is observable even after taking the daily average. On the other hand, if one averages over the lifetime of the experiment, as is typically done, the dark matter oscillations are also averaged over.

After averaging over the lifetime of the experiment, the oscillation probability is given by

$$\langle P_{\nu_e \to \nu_\mu} \rangle \quad = \quad P^{(0)} + \left(\frac{1}{2} n_{\parallel}^2 v_{\parallel}^2 + n_{\perp}^2 v_{\perp}^2 \right) \langle P^{(2)} \rangle + \cdots \tag{4.23}$$

where $P^{(0)}, P^{(2)}$ is same as in Eq. 4.13. Here we have assumed that the DM is light enough so that the coherence time of the DM is longer than the experiment lifetime, hence the vector polarization $(n_{\parallel}, n_{\perp})$ can be treated as constant. We see that the effect of the daily average is a correction of the DM effect which is dependent on the DM polarization and the beam direction. Given a global network of neutrino beam experiments, we can not only observe but also map out the DM polarization in the solar neighborhood.

If the DM coherence time is longer than a day but much smaller than the lifetime of the experiment, we have to average over all possible DM polarization.

$$\langle P_{\nu_e \to \nu_\mu} \rangle \quad = \quad P^{(0)} + \frac{1}{2} \left(\frac{1}{2} v_{\parallel}^2 + v_{\perp}^2 \right) \langle P^{(2)} \rangle + \cdots \tag{4.24}$$

For a neutrino beam experiment like DUNE, we can compare Eq. 4.14 to Eq. 4.24 to per-

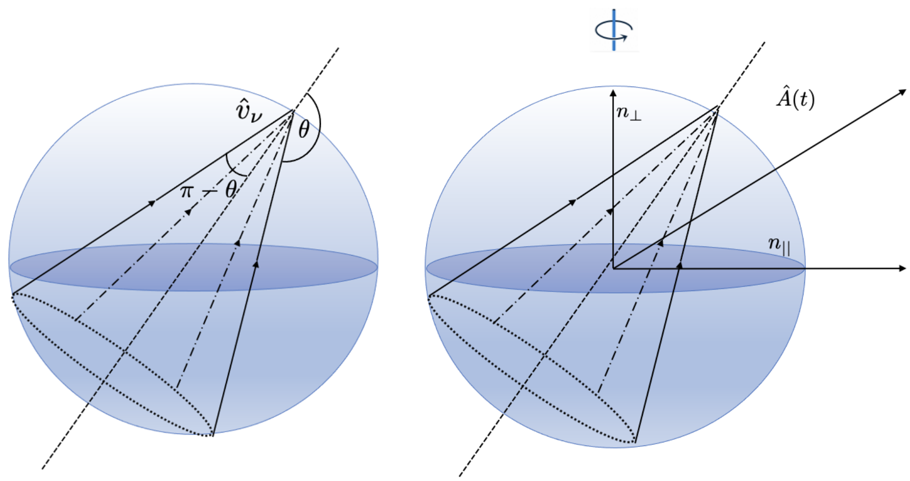

Figure 4.3: Schematic diagram showing the two different averages over atmospheric neutrino velocity. For atmospheric neutrinos, the neutrino velocity does not have a fixed direction. On the left, we have shown the averaging of the neutrino velocity over the same zenith angle θ (it is conventional to assign $\theta = 0$ to down-going neutrinos). Paths with the same zenith angle have equal lengths which form a cone. This is standard for atmospheric neutrino experiments, as discussed in 4.3.1. We also have to average over the daily modulation, which we have shown on the right.

ceive the effect of the earth's rotation. The difference depends upon the latitude and longitude of both the points of neutrino production and detection. On the other hand, for atmospheric neutrino experiment, shown in Fig. 4.3, there are a whole host of neutrino velocities distributed on a two sphere. It is customary to bin events by zenith angle θ, as shown in Fig. 4.3. Then each bin corresponds to atmospheric neutrinos with the same path length from production to detection. For an experiment located near the earth's rotation axis, like IceCube [139, 140], this corresponds to averaging over $v_{||}$. However, for an experiment located elsewhere, like Super-Kamiokande [17, 18, 135], the constant zenith angle averaging will correspond to different averages over the neutrino velocity depending on the particular location. To get an estimate of the impact of the velocity average on the vector DM effect, we can look at average over both neutrino velocity and DM polarization,

$$\langle P_{\nu_e \to \nu_\mu} \rangle = P^{(0)} + \frac{3}{8} \langle P^{(2)} \rangle + \cdots \tag{4.25}$$

The effect of daily average and the angular average is clear once we compare Eq. 4.14 to Eq. 4.25.

4.3 Experiments

In order to get a qualitative understanding of which experiments are the most efficient at detecting Vector DM, we can compare the relative strengths of various terms in the Hamiltonian

$$H_{\text{vac}} \sim \frac{\Delta m^2}{E_\nu}, \qquad H_{\text{int}} \sim g \frac{\sqrt{2\rho}}{m_A}. \tag{4.26}$$

Here, we can make a simplifying assumption that a given experiment is sensitive to DM when both terms in the Hamiltonian are comparable

$$H_{int} \lesssim H_{vac} \qquad \to \qquad g \lesssim \frac{m_A}{E_\nu} \frac{\Delta m^2}{\sqrt{2\rho}} \sim 10^{-30} \left(\frac{m_A}{10^{-20}\ \text{eV}} \right) \left(\frac{10\ \text{GeV}}{E_\nu} \right). \tag{4.27}$$

As the vacuum term gets smaller with higher neutrino energies, we can see that experiments that operate at higher energies have greater discovery potential.

Naively, one could use the most energetic neutrinos to set the most stringent constraints. However, as the energy of neutrinos increases so does the oscillation length. Since the longest baseline we can probe is of the size of the earth, this limits the most efficient energies to $E \sim 10$ GeV. Experiments that operate or will operate at these energies are Super-Kamiokande [17, 18, 135], IceCube [139, 140], DUNE [19, 137, 138] and Hyper-Kamiokande [141]. We can divide these experiments into two categories: atmospheric neutrino experiments (Super-Kamiokande, IceCube, DUNE and Hyper-Kamiokande) and beam experiments (DUNE). Below, we consider one experiment of each type, with Super-Kamiokande as an example of an atmospheric neutrino experiment and DUNE as an example of a neutrino beam experiment. We focus on time-independent signatures of VDM, leaving the time-dependent analysis to future work. [2]

4.3.1 Super-Kamiokande

Super-Kamiokande is a water-Cherenkov detector that is designed to measure neutrinos of astrophysical, atmospheric and accelerator origins. In this work, we focus on atmospheric neutrinos detected by Super-Kamiokande. In this type of experiment we can reconstruct neutrino direction and their energy. As neutrinos are produced in the atmosphere, the distance they travel before reaching the detector is related to the zenith angle θ shown in Fig. 4.3. When $\cos\theta = 1$, the distance covered by neutrinos is of order $O(10\text{ km})$, while $\cos\theta = -1$ corresponds to distances of order $O(10^4\text{ km})$. In our analysis, we focus on neutrinos coming from underground ($\cos\theta < 0$) as the longer effective baseline allows the effect of DM to accumulate, leading to stronger sensitivity.

Super-Kamiokande divides neutrino events into three main categories, fully contained (FC), partially contained (PC) and up-going muons (Up-μ). Both FC and PC categories include neutrinos that convert into electrons/muons inside the detector. However, leptons produced during

[2] By arguments around Eq. (4.27) we expect constraints from time-dependent and time-independent analysis to be comparable. It is important to note that the time-dependent analysis will be effective if the DM coherence time is at least as long as the duration of the experiment.

FC neutrino events deposit all energy inside the inner detector whereas leptons produced during PC events stop at the outer detector or deposit only a fraction of their energy before leaving the detector. The final type of event, Up-μ, includes muons that were produced outside the detector but stopped inside it or passed through it leaving a trace.

As we are interested in the neutrinos that have energies of order 10 GeV and whose angular direction can be resolved, there are two event sub-categories that meet this criterion, PC through-going and Up-μ stopping. Both samples have similar energy distributions that peak around 10 GeV [17]. The first sub-category includes mostly muons and antimuons that were produced inside the detector but managed to escape it. These events are binned over zenith angle $\cos\theta \in [-1, 1]$ with a bin size of $\Delta\cos\theta = 0.2$. The second sub-category contains the muons and antimuons that were produced outside the detector but stopped inside. Here, events are binned over a shorter range of zenith angle $\cos\theta \in [-1, 0]$, with a smaller bin size of $\Delta\cos\theta = 0.1$.

In the analysis, we use two data sets for each sub-category. The first one contains the number of observed events [18] as a function of the zenith angle $\cos\theta$, as shown in the Fig. 4.3. The second data set has the ratio of observed neutrino events to the expectation in the case of standard neutrino oscillations as a function of zenith angle $\cos\theta$ [17]. For Up-μ stopping sub-category both data sets are binned over $\cos\theta \in [-1, 0]$ into 10 bins of size $\Delta\cos\theta = 0.1$. For PC through-going sub-category we use the first 5 bins which correspond to $\cos\theta \in [-1, 0]$ as they are the most sensitive to the effect of VDM. We use these data sets as an experimental input to the χ^2 test

$$\chi^2(N_i, O_i) = 2\sum_{i=1}^{bins}\left(N_i - O_i + O_i \ln\frac{O_i}{N_i}\right) = 2\sum_{i=1}^{bins} O_i\left(\left(\frac{N_i}{N_i^0}x_i^{-1}\right) - 1 + \ln x_i \frac{N_i^0}{N_i}\right) \tag{4.28}$$

where O_i is the number of observed events, N_i is the number of expected events, N_i^0 is the number of expected events assuming standard neutrino oscillations [17] and $x_i = O_i/N_i^0$. The subscript i refers to the bin.

The input from our model is contained in the ratio $\frac{N_i}{N_i^0}$. In our work, we make a simplifying assumption that the energy of neutrinos is 10 GeV. We also assume that the detector response is identical for all neutrinos collected in a single bin. As a result, we can write the ratio $\frac{N_i}{N_i^0}$ as

$$\frac{N_i}{N_i^0} = \frac{\sum\limits_{a=e,\mu} \left\langle P_{a\to\mu} \right\rangle_i \Phi_{a,i} + \sum\limits_{a=\bar{e},\bar{\mu}} \left\langle P_{a\to\bar{\mu}} \right\rangle_i \Phi_{a,i}}{\sum\limits_{a=e,\mu} \left\langle P^0_{a\to\mu} \right\rangle_i \Phi_{a,i} + \sum\limits_{a=\bar{e},\bar{\mu}} \left\langle P^0_{a\to\bar{\mu}} \right\rangle_i \Phi_{a,i}} \tag{4.29}$$

where $\Phi_{a,i}$ is the atmospheric neutrino flux from [142]. $\langle P_{a\to\mu}\rangle_i$ is the probability averaged over bin i, where we average over azimuthal and zenith angles as well as DM oscillation and rotation of the earth. The probability is calculated in the low mass limit where we assume that the DM phase is approximately constant as the neutrino passes through the Earth. Following [17, 18] we include the effect of changing electron density by employing the PREM model [143]. Taking the same 3-flavor neutrino oscillation parameters as in [17] we get the following bounds at the 2σ level

$$g < 2 \cdot 10^{-31} \left(\frac{m_A}{10^{-20}\ \text{eV}}\right) \qquad g' < 1 \cdot 10^{-31} \left(\frac{m_A}{10^{-20}\ \text{eV}}\right). \tag{4.30}$$

These bounds are only valid in the low mass limit. The treatment of the high mass limit is explained in Sec. 4.3.3. The projected bounds are shown in Fig. 4.4 and 4.5.

In order to validate the above result we performed cross-checks by reproducing the results of Ref. [17]. Ref. [17] examined the bounds coming from Lorentz symmetry violation in the form of chemical potentials and thus resembles our signal up to the time and direction dependence. The reproduced results differed by up to a factor of two, which we can use as an estimate of the accuracy of our method.

4.3.2 DUNE

As mentioned before, sensitivity is best for an experiment with a long baseline and high energy. As an example of a neutrino beam experiment with these properties, we consider the Deep Underground Neutrino Experiment (DUNE). DUNE produces a beam of primarily muon neutrinos at Fermilab at energies between 0.5 and 10 GeV. These neutrinos are then sent along a 1285 km path to a detector in Lead, SD. There, they measure the number of muon neutrinos that have disappeared (N^{dis}) and the number of electron neutrinos that have appeared (N^{app}). Figures 10 and 11 in Ref. [138] present a prediction for $N^{dis,app}$ using standard neutrino oscillations with the number of disappearance/appearance events. This data is presented in energy bins of width 0.25 GeV from $0.5 - 8$ GeV.

We can use these measurements to place bounds on our vector dark matter interaction. An exact treatment would involve a full simulation of the detector using the GLoBES framework [144, 145] as was done in Ref. [138] for standard oscillations and for a variety of BSM extensions to standard oscillations in Ref. [19]. However, we take a simplified approach by assuming that the detector response is the same for all neutrinos in a single energy bin. In this approximation, we can write $N_i^{app}(N_i^{dis})$, the number of electron-neutrino appearance events (muon-neutrino disappearance events) in the i^{th} energy bin, as

$$N_i^{dis} = N_i^{dis,0} \frac{1 - \langle P_{\mu\to\mu} \rangle_i}{1 - \langle P^0_{\mu\to\mu} \rangle_i} \qquad N_i^{app} = N_i^{app,0} \frac{\langle P_{\mu\to e} \rangle_i}{\langle P^0_{\mu\to e} \rangle_i} \tag{4.31}$$

Here the superscript 0 represents quantities taken without dark matter interactions and $\langle\rangle_i$ represents averaging over the i^{th} energy bin. We numerically compute the oscillation probabilities using three flavor oscillations in the low mass limit. We vary the dark matter coupling, g or g', while three-flavor oscillation parameters are kept fixed at the central values of the global fit [146] used by the DUNE collaboration in their simulated data for appearance/disappearance events [19]. Placing projected bounds from DUNE is complicated by the fact that we only have predicted data for N_i^{app} and N_i^{dis} and not any actual data. If we did have an observed number of events in each bin O_i we could simply compute the χ^2 for our theory using Eq 4.28. If we wanted to compare our vector dark matter theory to standard oscillations, we would look at the difference in χ^2 between the two theories

$$\Delta\chi^2(N_i, N_i^0, O_i) = \chi^2(N_i, O_i) - \chi^2(N_i^0, O_i) = 2\sum_i N_i - N_i^0 + O_i \ln\left(\frac{N_i^0}{N_i}\right) \tag{4.32}$$

Here the sum over bins sums over the bins for both muon-neutrino disappearance and electron-neutrino appearance to give the total χ^2. However, since we do not have any real data to compare to, we imagine drawing O_i from the distribution for appearance/disappearance events for standard oscillations given by N_i^0. Since $\Delta\chi^2$ is linear in O_i this amounts to replacing O_i with N_i^0 in Eq 4.32.

$$\left\langle \Delta\chi^2(N_i, N_i^0, O_i)\right\rangle_{O_i} = \chi^2(N_i, N_i^0) \tag{4.33}$$

If $\Delta\chi^2 > 4$ we would then be able to distinguish standard oscillations from standard oscillations with our vector dark matter interaction at the 2σ level. We can then place a predicted bound on our coupling, assuming that DUNE will not find disagreement with standard oscillations, by demanding

$$\Delta\chi^2(g) < 4 \tag{4.34}$$

where g is the coupling of interest. As a cross-check, we were able to use this method to reproduce the bounds on the flavor-diagonal piece of the non-standard neutrino interactions from Ref. [19] to within 20%. These flavor-diagonal non-standard neutrino interactions are very similar to our dark matter interaction. In fact, they are equivalent if we send $\cos(m_A t + \phi)\cos(\alpha) \to 1$ in Eq. 4.8. It is likely that our bounds have similar error bars.

As seen from Eq. 4.8, the strength of our interaction depends not only on the strength of the coupling g and g' but also on the relative direction of the neutrino velocity to the dark matter polarization and the phase of the dark matter. All of these quantities vary on different timescales. The phase of the dark matter, $m_A t + \phi$ in Eq. 4.8, changes on the time scale m_A^{-1}. The direction of the neutrinos' velocity changes on a daily time scale due to the earth's rotation. Finally, the direction and amplitude of the dark matter background and changes on the scale of the coherence time of the dark matter background which scales with $t_{coh} \sim 10^6\, m_A^{-1}$. For time scales that are shorter than the total data collection time of DUNE, around 3-7 years, we should average the probabilities $P_{\mu\to\mu}$ and $P_{\mu\to e}$ over these time scales before placing the bound from Eq. 4.34. This is true for all three of our relevant time scales except for the coherence time for masses $m_A < 3\cdot 10^{-18}$ eV. For masses below this limit, the dark photon field is coherent during the 3-7 year duration of the experiment so we must first compute bounds for each direction of the dark photon polarization. Then, in order to capture the fact we do not know in which direction the dark matter points, we should average these bounds over all dark photon polarizations. However, we find that whether or not we average over dark matter polarizations before or after computing the bounds leads to an $\mathcal{O}(10\%)$ change in the resulting average bound in the end. We, therefore, ignore this subtlety and average over all time scales before computing the bound. We find the bounds on $g(g')$ to be

$$g < 10^{-30}\left(\frac{m_A}{10^{-20}\text{ eV}}\right) \qquad g' < 7\cdot 10^{-31}\left(\frac{m_A}{10^{-20}\text{ eV}}\right). \tag{4.35}$$

These bounds are shown plotted below in Fig. 4.4 and 4.5.

As mentioned before, we are using DUNE as an example of the sensitivity of a neutrino beam experiment. DUNE expects to detect oscillations from the background atmospheric neutrinos as described in Ref. [137] where they argue DUNE will have a sensitivity similar to Hyper-Kamiokande. If one were to use this aspect of DUNE, then the bounds in Eq. 4.35 and Eq. 4.30 would be improved upon significantly.

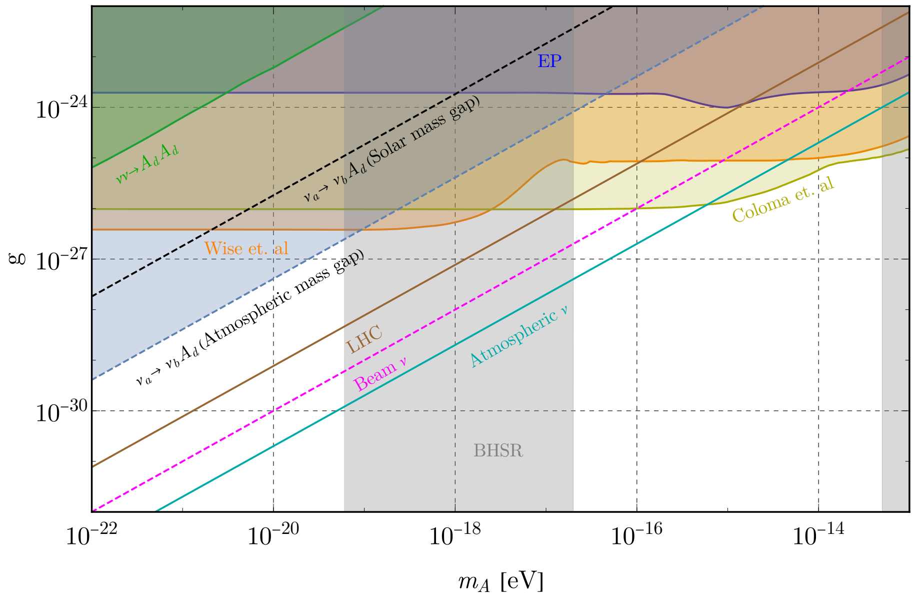

Figure 4.4: Constraints on the $L_e - L_\mu$ coupling from atmospheric and beam neutrino experiments. The curves show upper limits on the coupling g. The atmospheric neutrino bound is represented by the cyan line, which is derived using Super-Kamiokande data [17, 18]. The dashed magenta line gives the projected sensitivity of neutrino beam experiments, which is obtained assuming DUNE operating in the beam mode [19]. Our constraints are several orders of magnitude stronger than the cosmological ν-decay bound (light blue and black dashed lines) [20] and five orders of magnitude stronger than other terrestrial bounds at the lower end of the allowed mass range. It is expected that time dependent analysis will improve these bounds. Other constraints are from BH superradiance (gray band) [21], neutrino oscillations modified by a fifth force (orange and yellow lines) [22, 23], ΔN_{eff} through $\nu\nu \to A_d A_d$ (green line) [24, 25], EP violating forces (dark blue line) [22, 26] and a model dependent bound coming from a mono-lepton plus missing energy search at LHC (brown line) [27].

4.3.3 Results

We numerically find the DUNE and Super-Kamiokande bound for a DM mass in the small mass limit using the methods described before. To obtain a bound for an arbitrary mass, we rescale the bound using the full second-order correction to the oscillation probability, $\langle P^{(2)} \rangle$, given in Eq. 4.15. In Eq. 4.15, L is the neutrino baseline, $\Delta_\nu = \frac{\Delta m^2_{13}}{4E_\nu}$, A_0 is the field strength $A_0 = \frac{\sqrt{2\rho_{DM}}}{m_A}$, and g is the coupling we are interested in (either g or g'). For each of the experiments, we insert different values of L and E_ν. For DUNE [138], we use the baseline $L \approx 1300$ km and $E_\nu = 2$ GeV, roughly the energy at which detection events peak. For Super-Kamiokande we use $E_\nu = 10$ GeV. The length for Super-Kamiokande is complicated since, for atmospheric neutrinos, L varies depending on the zenith angle θ. In principle, we should use an effective length, weighted over the bins. For simplicity, we use $L \approx 12000$ km, roughly the diameter of the earth. A different choice of L does not alter our constraint in the low mass regime or its qualitative feature over the whole of the parameter space.

In order to use Eq. 4.15 to rescale our bounds, perturbation theory in g (g') must be valid. Using Eq. 4.18 with $E_\nu = 10$ GeV for Super-Kamiokande and $E_\nu = 2$ GeV for DUNE to obtain the perturbative limit for both experiments and comparing these limits to the bounds placed in Eq. 4.30 and 4.35, we find that our bounds are soundly in the perturbative limit.

As an additional cross-check of this extrapolation, we solved for the transition probabilities numerically for a few values of m_A in the high mass regime for both DUNE and Super-Kamiokande. While doing this for all points in our parameters space is too computationally expensive, we find good agreement between our perturbation extrapolation to high masses and the exact numerical results.

4.4 Conclusions

In this chapter, we studied the effects of ultra-light vector dark matter consisting of a dark photon. We consider our dark photon to be the gauge boson of gauged lepton flavor number with different couplings for each flavor. We showed the effect of such a coupling in the context of neutrino oscillations is to give each neutrino flavor an effective chemical potential proportional to the background dark matter field and the coupling. Because the couplings are flavor asymmetric,

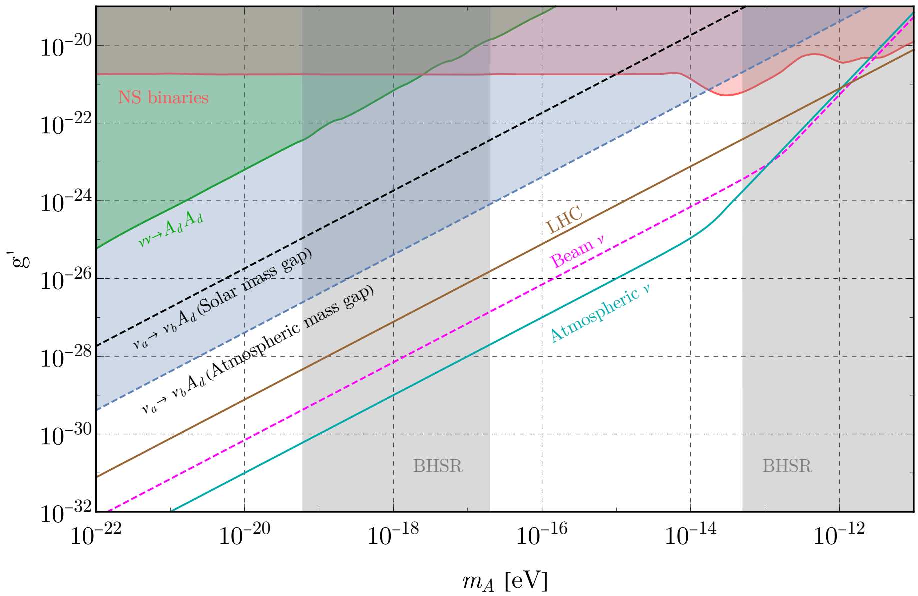

Figure 4.5: Constraints on the $L_\mu - L_\tau$ coupling from atmospheric and beam neutrino experiments. The curves show upper limits on the coupling g'. The atmospheric neutrino bound is derived using Super-Kamiokande data [17,18]. The projected sensitivity of beam neutrino experiments is obtained assuming DUNE operating in the beam mode [19]. Our constraints are several orders of magnitude stronger than the cosmological ν-decay bound (light blue and black dashed lines) [20] and eight orders of magnitude stronger than other existing constraints at the lower end of the allowed mass range. It is expected that time-dependent analysis will improve these bounds. Previous constraints are from BH superradiance (gray band) [21], ΔN_{eff} through $\nu\nu \to A_dA_d$ (green line) [24, 25], NS binaries (red line) [28] and a model-dependent bound coming from a mono-lepton plus missing energy search at LHC (brown line) [27].

these chemical potentials are different for each neutrino flavor and thus will have some effect on neutrino oscillations. Because this interaction is diagonal in flavor space, we saw that the net effect of these couplings is to dampen the mixing, and thus dampen oscillations between neutrino flavor eigenstates.

Using this effect, we are able to place bounds on the flavor asymmetric couplings g $(U(1)_{L_e-L_\mu})$ and g' $(U(1)_{L_\mu-L_\tau})$ by comparing to neutrino oscillation experiments. Using Super-Kamiokande (DUNE) as an example, we found the (projected) bounds coming from an atmospheric (beam) neutrino experiment. These bounds are shown in Fig. 4.4 and Fig. 4.5. For both, we found our bounds beat previously leading bounds for low dark matter masses and give bounds comparable to leading bounds at high masses.

We also considered time-dependent effects unique to our vector dark matter background. In particular, due to the Earth's rotation, neutrinos in the earth's frame see a vector background that rotates on a daily basis. Since the coupling between neutrinos and the dark matter background is proportional to $\vec{A}_d \cdot \vec{v}_\nu$, this rotation effect would manifest as daily modulations in neutrino oscillations. In our bounds, we averaged over these daily modulations. However, one could look for these daily modulations directly. These daily modulation would be seen as a daily time dependence in the appearance/disappearance events. One would need to have the time-stamped data to see this effect. This would involve working directly with the data from neutrino oscillation experiments and so we leave it for future works. In addition to this time-dependent analysis, bounds could be made more precise with future atmospheric neutrino experiments such as Hyper-Kamiokande, DUNE and by working more directly with experiments like IceCube.

Chapter 4: Conclusion

Ultralight fields make for exciting dark matter candidates. A simple yet efficient misalignment mechanism makes it easy to produce scalar dark matter, while the multitude of potential couplings to the SM combined with the narrow frequency band of the signal and long coherence time, has led to a huge excitement in the experimental community. In this dissertation, we look only at certain aspects of this vibrant area.

In Chapter 2, we show an example model of a very light modulus DM with sizeable couplings to the SM. We achieve this by employing Z_N symmetry, which translates to introducing N copies of the Standard Model. Between the neighboring copies, the value of the scalar is shifted by a $2\pi f/N$, forcing the vacuum potential to be proportional to $\cos N\phi/f$ and parametrically much smaller than naively expected. The scalar has a region in parameter space in which it naturally constitutes the majority of DM while being within reach of the current and proposed experiments.

In Chapter 3, we investigate the future sensitivity of atomic and nuclear clocks to measuring a scalar potential. This approach relies on the fact macroscopic bodies such as earth or sun source the scalar field. This Yukawa potential affects the values of fundamental parameters around these sources. As atomic and nuclear clocks are very sensitive to changes in these parameters, we assess the experimental reach of various scenarios, including earth-based and space-borne setups. We find that they can result in improvements up to 2 orders of magnitude for certain parameters.

In Chapter 4, we discuss the influence of $L_e - L_\mu$, $L_\mu - L_\tau$ vector dark matter on neutrino oscillations and use it to set constraints on the coupling to leptons. The main effect that we consider is the change in the neutrino mass eigenstate due to interaction with dark photons $g\vec{v} \cdot \vec{A}_d \sim g\sqrt{\rho_{\rm DM}}/m_A$. This contribution to the neutrino potential is detectable when it is comparable to $\Delta m_\nu^2/E_\nu$. As the sensitivity improves with higher-energy neutrinos we find that atmospheric neutrinos are the best suited to look for this, improving current bounds by several orders of magnitude.

Appendix A: Chapter 2 supplemental materials

A.1 Finite Temperature Effects

In this appendix we obtain the contribution to the potential of the modulus from finite temperature effects. For temperatures $T \gtrsim M$, the leading contribution arises from the free energy contribution of the vector-like fermion Ψ through the dependence of its mass on the value of the modulus, as given in Eq. (2.5). This contribution is represented by the one-loop diagram shown in Fig. A.1.

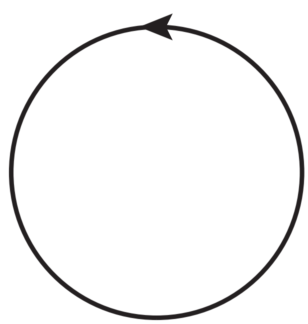

Figure A.1: Diagram representing the leading contribution to the potential of the modulus for temperatures $T \gtrsim M$.

The form of this contribution is well-known [147, 148] and is given by the integral

$$F_f = \frac{2T^4}{\pi^2} \int_0^\infty dx x^2 \ln\left(1 + \exp\left\{-\sqrt{x^2 + \left(\frac{M_N}{T}\right)^2}\right\}\right) \tag{A.1}$$

We can extract the effect on the potential of the modulus by Taylor expanding the potential around $M_N = M$ and keeping the correction of order $O(\epsilon)$,

$$V_T(\varphi, T) \supset -\epsilon M \frac{dF_f}{dM} \cos \frac{\varphi}{f}. \tag{A.2}$$

This leads to

$$-\epsilon M \frac{dF_f}{dM} \cos \frac{\varphi}{f} \approx \begin{cases} \frac{\epsilon M^2}{6} T^2 \cos \frac{\varphi}{f} & T > M \\ \\ \frac{4\epsilon M^{\frac{5}{2}} T^{\frac{3}{2}}}{(2\pi)^{\frac{3}{2}}} e^{-\frac{M}{T}} \cos \frac{\varphi}{f} & T \lesssim M \end{cases}. \tag{A.3}$$

Another type of contribution arises from the dependence of the free energy of the universe on the hypercharge gauge coupling, which in turn is a function of the VEV of the modulus,

$$g'^2(\varphi) \supset \frac{\epsilon g'^4}{\pi^2} \int_0^1 dx \frac{x(1-x)}{1 + \left(\frac{T}{M}\right)^2 x(1-x)} \cos \frac{\varphi}{f}. \tag{A.4}$$

From the above expression we can determine the dependence of this effect on the temperature,

$$g'^2(\varphi) \supset \begin{cases} \frac{\epsilon g'^4}{\pi^2} \left(\frac{M}{T}\right)^2 \cos \frac{\varphi}{f} & T \gg M \\ \\ \frac{\epsilon g'^4}{6\pi^2} \cos \frac{\varphi}{f} & T \ll M \end{cases}. \tag{A.5}$$

The leading finite temperature contributions to the free energy of the universe that involve the hypercharge gauge coupling arise at two loops. The problem therefore reduces to computing these two loop diagrams. There are three types of diagrams labelled by a, b and c that contribute at this order,

$$V_T(\varphi, T) = \frac{2\epsilon\alpha q_F^2 u(\frac{T}{M})}{3\pi\cos^2\theta_W}\left(\sum_i F_a^i + F_b + F_c\right)\cos\left(\frac{\varphi}{f}\right) , \tag{A.6}$$

where

$$u(y) = \int_0^1 dx \frac{6x(1-x)}{1+y^2x(1-x)} . \tag{A.7}$$

The diagrams that give rise to F_a^i, F_b and F_c are shown in Fig. A.2. Here the index i runs over all quark and lepton flavors. Using the methods of thermal field theory [147, 148] the first diagram, which represents the correction to the free energy from diagrams involving the SM fermions, can be evaluated

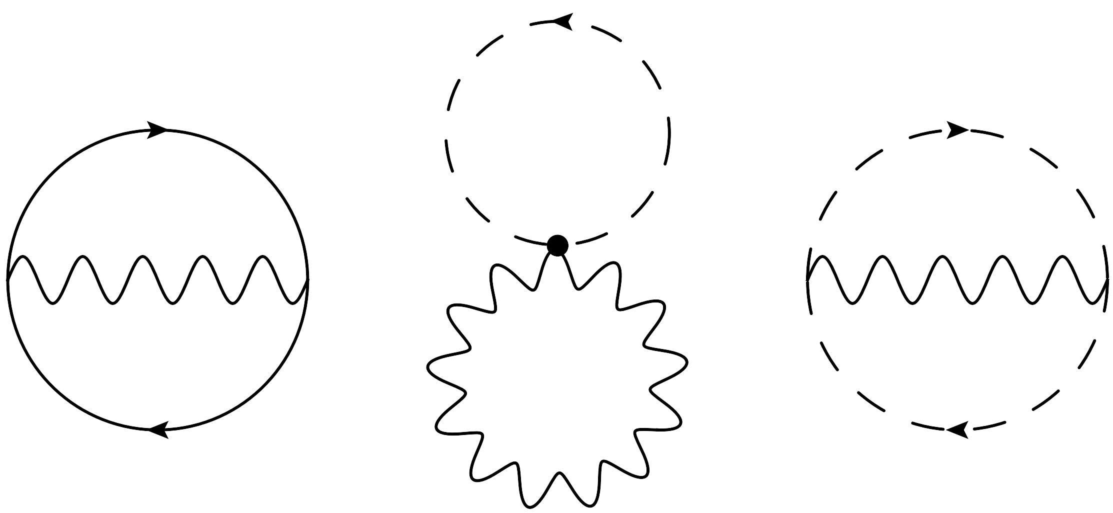

Figure A.2: Diagrams contributing to the effective potential. The first diagram on the left corresponds to the term F_a^i, the next to F_b and the last to F_c as defined in Eq. (A.6).

as

$$F_a^i = -\frac{g'^2 q_i^2}{2} \sum\!\!\!\!\!\!\!\int_{\{P,R\}Q} \frac{Tr\{\tilde{\gamma}_\mu(-i\not{P}+m_i)\tilde{\gamma}_\mu(-i\not{R}+m_i)\}}{Q^2(P^2+m_i^2)(R^2+m_i^2)} \times \\ \times\, \delta^{(4)}(P+Q-R) \tag{A.8}$$

where we follow the conventions of [147]. In these conventions the $\tilde{\gamma}_\mu$ represent the Euclidean

Dirac matrices,

$$\tilde{\gamma}_0 \equiv \gamma^0 , \qquad \tilde{\gamma}_k \equiv -i\gamma^k , \qquad k = 1, ..., d . \tag{A.9}$$

The momenta in the loop integrals are in Euclidean space and have components $P = (\omega_n^i, \vec{p})$, where $i = b, f$. The symbol $\SumInt$ refers to integration over the spatial momenta along with summation over the Matsubara frequencies, which are defined as

$$\omega_n^f = 2\pi T(n + \frac{1}{2}) , \qquad \omega_n^b = 2\pi T n \tag{A.10}$$

for fermions and bosons respectively. If the momenta below the symbol $\SumInt$ appear between curly brackets $\{...\}$ it corresponds to summation and integration over fermionic boundary conditions while the absence of the brackets indicate bosonic boundary conditions. After the usual Dirac algebra we can express Eq. (A.8) in terms of known standard integrals [149, 150],

$$\begin{aligned} F_a^i = -\frac{d}{2}(\frac{d}{2}-1)g'^2 q_i^2 \Bigg\{ & 2 \SumInt_{\{P\}} \frac{1}{P^2+m_i^2} \SumInt_Q \frac{1}{Q^2} - \left[\SumInt_{\{P\}} \frac{1}{P^2+m_i^2} \right]^2 \\ & + \frac{4m_i^2}{d-2} \SumInt_{\{P,R\}} \frac{1}{(P-R)^2(P^2+m_i^2)(R^2+m_i^2)} \Bigg\} , \end{aligned} \tag{A.11}$$

where $d = 4 - 2\epsilon$. In the $T/m \to \infty$ limit the last integral vanishes [150]. The remaining integrals are well known,

$$\SumInt_Q \frac{1}{Q^2} = \frac{T^2}{12} \qquad \text{and} \qquad \SumInt_{\{P\}} \frac{1}{P^2} = -\frac{T^2}{24}. \tag{A.12}$$

Putting these together we arrive at the result in the high temperature/low mass limit,

$$F_a^i \approx \frac{5\pi\alpha q_i^2}{72\cos^2\theta_W} T^4 , \tag{A.13}$$

where we have expressed g' in terms of the fine structure constant α and the Weinberg angle θ_W. Since the q_i represent the hypercharges of the SM fermions and the heavy fermion Ψ from our sector, after including all the contributing particles we obtain a factor of $\sum_i q_i^2 = 6$.

The second and the third diagrams represent contributions to the free energy from the Higgs doublet. We focus on the high temperature/low mass limit prior to electroweak symmetry breaking. The contribution to the amplitude from the second diagram can be written as the product of the amplitude of two independent one loop diagrams,

$$F_b = \frac{g'^2}{2} g^\mu_\mu \sum\!\!\!\!\!\!\int_P \frac{1}{P^2 + m^2} \sum\!\!\!\!\!\!\int_Q \frac{1}{Q^2} \, . \tag{A.14}$$

In the $T/m \to \infty$ limit we obtain,

$$F_b \approx \frac{\pi \alpha}{18 \cos^2 \theta_W} T^4 \, . \tag{A.15}$$

Finally, the third diagram has a form very similar to the first (A.11), except that now all the integrals are bosonic,

$$\begin{aligned} F_c &= \frac{g'^2}{4} \sum\!\!\!\!\!\!\int_{P,Q,R} \frac{(P+R)^2}{(P^2+m^2)(R^2+m^2)Q^2} \delta^4(R - P - Q) \\ &\approx \frac{\pi \alpha}{48 \cos^2 \theta_W} T^4 \, . \end{aligned} \tag{A.16}$$

Now, using Eqs. (A.3) and (A.6) we put all the pieces together and see that for $T \gg M$, the temperature dependent contribution simplifies to,

$$V_T(\varphi, T) = \left(\frac{71 \epsilon \alpha^2}{36 \cos^4 \theta_W} + \frac{\epsilon}{6} \right) T^2 M^2 \cos\left(\frac{\varphi}{f}\right) . \tag{A.17}$$

When the temperature falls below $T \sim M$, the contribution given by Eq. (A.3) becomes exponentially suppressed while the correction to the gauge coupling from Eq. (A.5) becomes independent of temperature. Additionally, the vector-like fermion Ψ of our sector no longer contributes to the Eq. (A.13), resulting in $\sum_i q_i^2 = 5$. Therefore, when the temperature enters the range $M \gtrsim T \gtrsim 100$ GeV, the potential takes the form

$$V_T(\varphi, T) = \left(\frac{61\epsilon\alpha^2 q_F^2}{216\cos^4\theta_W} T^4 + \frac{4\epsilon M^{\frac{5}{2}} T^{\frac{3}{2}}}{(2\pi)^{\frac{3}{2}}} e^{-\frac{M}{T}} \right) \cos\left(\frac{\varphi}{f}\right). \tag{A.18}$$

After electroweak symmetry breaking, we can neglect the contribution from the Z boson as it is suppressed almost immediately. To get the contribution from photons we multiply the temperature dependent part in Eq. (A.6) by $\cos^4\theta_W$, which effectively replaces the hypercharge gauge coupling g' by e

$$V_T(\varphi, T) = \epsilon\alpha^2 q_F^2 q_{eff}^2(T) T^4 \cos\left(\frac{\varphi}{f}\right). \tag{A.19}$$

Here $q_{eff}^2(T)$ is a coefficient that changes with the number of species that contribute to the temperature dependent potential. As the universe cools down the number of species that contribute to the potential drops as heavier fields go out of the bath. This in turn, increases the relative strength of Hubble friction. However, this effect is partially compensated for by the rise in the temperature when heavy fields exit the thermal bath.

Therefore, the thermal potential does not change qualitatively until the temperature drops below the mass of the lightest charged particle, the electron, so that $T \lesssim m_e$. However, in order for this effect to play any role in the evolution of the modulus φ, the thermal part $V_T(\varphi, T)$ has to be significant at this point in time, which requires

$$\eta \gtrsim \eta_0, \tag{A.20}$$

where η_0 was defined in Eq. (2.36). On the top of that, $V_T(\varphi, T)$ has to dominate over $V_0(\varphi)$ at $T \sim m_e$. Hence, we have to satisfy

$$T_s \lesssim 1\text{MeV} \qquad \text{and} \qquad \eta \gtrsim \eta_0 \tag{A.21}$$

If we additionally require that these conditions overlap with the parameter space not excluded by experiments, we conclude that for $M \gtrsim 1$ TeV no solutions exist that satisfy the above criteria simultaneously. It therefore suffices to consider the high temperature limit of the temperature dependent potential.

A.2 Form of the Potential at the Onset of Oscillations

In section 2.3 we argued that in the case when N is even and we are in the underdamped scenario, $\eta > 1$, the energy density is well approximated by Eq. (2.41). This formula assumes that field only begins the final stage of oscillations once the finite temperature contributions to the potential are small, so that that the potential is well approximated by its zero temperature form. In order to verify that this condition holds, we will show that for most of the range of parameters considered in Fig. 2.4, the height difference between the the central maximum and the closest minimum is already within 10% of its final value at the time that the oscillations begin. Recall that the potential is proportional to the sum of two cosines

$$\begin{aligned} V(\varphi, T) &\propto \frac{N^2 m^2(T)}{m_\phi^2} \cos\left(\frac{\varphi}{f}\right) + \cos\left(\frac{N\varphi}{f}\right) \\ &= \frac{N^2 T^4}{T_{tr}^4} \cos\left(\frac{\varphi}{f}\right) + \cos\left(\frac{N\varphi}{f}\right) \end{aligned} \tag{A.22}$$

where $m^2(T)$ is defined in Eq. (2.24) and T_{tr} is the temperature at which $V_0(\varphi)$ and $V_T(\varphi, T)$ have quadratic terms of the same magnitude at $\varphi = \pi f$,

$$T_{tr} = \left(\frac{216 \cos^4 \theta_W}{61\alpha^2}\right)^{1/4} \frac{\sqrt{m_\phi f}}{\epsilon^{1/4}} = \sqrt{6} T_s \eta^{-1/4}. \tag{A.23}$$

Naively, oscillations will begin at a temperature $\tilde{T}$ when

$$\tilde{m}^2 \equiv m_\phi^2 - m^2(\tilde{T}) = 9H^2 \tag{A.24}$$

This equation defines $\tilde{m}$, the effective mass at temperature $\tilde{T}$. Eq. (A.24) may be rewritten as,

$$\frac{T_{tr}^4}{\tilde{T}^4} = \frac{m_\phi^2}{m^2(\tilde{T})} = 1 + 9\frac{H^2}{m^2(\tilde{T})} = 1 + \frac{36}{\eta}, \tag{A.25}$$

At temperature $\tilde{T}$, Hubble friction is sufficiently small for the field ϕ to roll down. However, due to the small gradient near the top of the potential, the moment it reaches the bottom of the potential is delayed by approximately [103]

$$\Delta t = \frac{2}{3m_\phi} \log\frac{1}{x} = t_s \log\frac{1}{x}, \tag{A.26}$$

where $x = 1 - \frac{N\phi}{\pi f}$ is a measure of how close to the maximum the field is when oscillations about the zero-temperature minimum begin and t_s is the time at which oscillations would start in the overdamped scenario. The value of x can be obtained from Eq. (2.39) as

$$x = \frac{N}{\sqrt{3}} \sqrt{\frac{m(T_{osc})}{m_\phi} \left(\frac{T_s}{T_o}\right)^{\frac{3}{2}}} \ . \tag{A.27}$$

Before moving on, it is important to point out that the Eq. (A.26) provides a good qualitative explanation of the ϕ evolution, but does not lead to Eq. (2.41), which is purely empirical. Now, with Eq. (A.26) we see that the time at which oscillations effectively start is

$$t_{eff} = \tilde{t} + t_s \log \frac{1}{x}, \tag{A.28}$$

where $\tilde{t}$ is a time when $T = \tilde{T}$. Using the fact that this transition always occurs during the radiation dominated epoch, when $T \propto t^{-1/2}$, we can write

$$\frac{T_s^2}{T_{eff}^2} = \frac{T_s^2}{\tilde{T}^2} + \log \frac{1}{x}. \tag{A.29}$$

Then, with help from Eq. (A.23) and Eq. (A.25), we can write

$$\frac{T_{eff}^4}{T_{tr}^4} = \frac{\eta}{36} \left(\sqrt{1 + \frac{\eta}{36}} + \log \frac{1}{x}\right)^{-2} . \tag{A.30}$$

The ratio T_{eff}^4 / T_{tr}^4 determines the shape of the potential in Eq. (A.22) at $T = T_{eff}$. Eq. (A.30) relates this ratio to the parameter η. Using these equations we can determine the ratio of the height difference between the central maximum and the closest minimum at $T = T_{eff}$ relative to the same height difference at zero temperature,

$$\begin{aligned}\frac{\Delta h}{h} &= \frac{V(\pi f, T_{eff}) - V(\pi f + \pi f/N, T_{eff})}{V(\pi f, 0) - V(\pi f + \pi f/N, 0)} = \\ &= 1 - (1 - \cos\frac{\pi}{N})\frac{N^2 T_{eff}^4}{2T_{tr}^4} = \\ &= 1 - (1 - \cos\frac{\pi}{N})\frac{N^2\eta}{72}\left(\sqrt{1+\frac{\eta}{36}} + \log\frac{1}{x}\right)^{-2} .\end{aligned} \tag{A.31}$$

Since the lowest value of $\log\frac{1}{x}$ for both $N = 6$ and $N = 10$ is $\log\frac{1}{x} \approx 5$, in order to satisfy $\Delta h/h > 0.9$ we need $\eta \ll 70$. This condition is easily fulfilled for $N = 6$ as $\eta \lesssim 40$. However, for $N = 10$ it is satisfied only for smaller values of the mass of the modulus, $m_\phi \lesssim 10^{-12}$ eV. Nevertheless, as evident from the numerical simulations presented in Fig. 2.4, Eq. (2.52) continues to give a good approximation to the actual result even when this condition is not satisfied.

A.3 Parametric Resonance

One may worry that decays of ϕ into photons may deplete the abundance of dark matter, particularly if the decay rate is enhanced by parametric resonance. In this appendix we consider this question. We find that in the region of parameter space of interest, the condition for parametric resonance is not satisfied. Therefore these decays are slow on cosmological time scales and the abundance of dark matter is not affected.

The Lagrangian for the coupling of ϕ to photons can be written as

$$\mathcal{L} = -\frac{1}{4g^2(\phi)}F^2 \quad \text{where} \quad \frac{1}{g^2(\phi)} = \frac{1}{e^2} + \frac{\epsilon}{6\pi^2}\frac{\phi}{f}. \tag{A.32}$$

The resulting equation of motion for the photon is given by

$$g^2(\phi)\partial_\mu\{g^{-2}(\phi)\}F^{\mu\nu} + \Box A^\nu - \partial^\nu\partial_\mu A^\mu = 0\ . \tag{A.33}$$

Working in the gauge where $A_0, \partial_\mu A^\mu = 0$ this becomes,

$$\Box A^\nu = -e^2\frac{\epsilon}{6\pi^2}\frac{\dot{\phi}}{f}\partial_0 A^\nu. \tag{A.34}$$

This leads to the modified dispersion relation,

$$(\omega^2 - k^2) = \frac{\epsilon e^2}{6\pi^2}\frac{\dot{\phi}\omega}{f}. \tag{A.35}$$

Because the plasma mass of the photon is large at the time of the phase transition, we are interested in parametric resonance at times when $\phi/f \ll 1$. Perturbatively expanding the time-dependent dispersion relation, we obtain

$$k = \omega - \delta k \qquad \text{where} \qquad \delta k = \frac{\epsilon e^2}{12\pi^2}\frac{\dot{\phi}}{f}. \tag{A.36}$$

When the ϕ condensate decays, the resulting photons have the frequency $\omega = m_\phi/2$. In phase space, the photons are emitted into a thin shell centered around $m_\phi/2$ with width $2\delta k$. The occupation number of photons $\tilde{n}_\gamma^k$ with momentum k can be related to the number density of photons n_γ as

$$\tilde{n}_\gamma^k = \frac{n_\gamma}{4\pi k^2 2\delta k}. \tag{A.37}$$

The integrated Boltzmann equation for the production of photons from the decay of the ϕ condensate in the Bose enhanced regime ($\tilde{n}_\gamma^k \gg 1$) is given by,

$$\frac{d}{dt}(a^3 n_\gamma) = 2a^3\Gamma(1 + 2\tilde{n}_\gamma^k)n_\phi \approx 4a^3\Gamma\tilde{n}_\gamma^k n_\phi = a^3\frac{\Gamma n_\phi}{2\pi k^2 \delta k}n_\gamma \tag{A.38}$$

where Γ denotes the decay rate of the condensate into photons at zero background photon density. This decay rate Γ can be estimated as

$$\Gamma \sim \left(\frac{e^2\epsilon}{6\pi^2}\right)^2 \frac{m_\phi^3}{f^2}. \tag{A.39}$$

For all of the benchmark points in Table 2.2, the lifetime is greater than 10^{75} years. This is much greater than the age of the universe. Therefore, in the absence of parametric resonance, decays of ϕ can safely be neglected.

The parametrically-resonant decay rate can be easily read off from Eq. (A.38) as

$$\Gamma_{res} = \frac{\Gamma n_\phi}{2\pi k^2 \delta k} = \frac{2e^2\epsilon m_\phi}{3\pi^3}\frac{\phi}{f}, \tag{A.40}$$

where we have used $n_\phi = m_\phi \phi^2$ and $\dot{\phi}/\phi = m_\phi$. In an expanding universe the proper momentum is redshifting as $k = k_{comoving}/a$. This means that the radius of the thin momentum shell is shrinking at the rate of kH. Since the momentum shell has a finite width $2\delta k$, it takes time $t_k = 2\delta k/(kH)$ for an emitted photon to redshift outside the momentum shell. In order to avoid Bose enhancement of decays in the expanding universe, this time scale t_k has to be parametrically smaller than the decay rate Γ_{res} at the time of decay,

$$\frac{2\delta k}{kH} \ll \frac{1}{\Gamma_{res}}. \tag{A.41}$$

At early times prior to photon decoupling, the photon has a plasma mass which is larger than m_ϕ. Consequently, decays of ϕ into photons are kinematically forbidden until after decoupling. This means that the condition in Eq. (A.41) only has to be satisfied at times after $T_{decoupling} \approx 0.3$ eV to avoid parametric resonance. Since decoupling happens during matter domination, the Hubble expansion at these times can be related to the field ϕ as

$$H = \sqrt{\rho_m}/(3M_{pl}) = m_\phi \phi/(3M_{pl}\sqrt{r}), \tag{A.42}$$

where r is the fraction of dark matter constituted by ϕ. Then, the condition to avoid parametric resonance becomes,

$$\frac{2\sqrt{r}\epsilon^2 e^4}{3\pi^5}\frac{M_{pl}\phi}{f^2} \ll 1. \tag{A.43}$$

This condition is easily satisfied because the amplitude of the field ϕ has already undergone significant damping by the time of recombination.

Appendix B: Chapter 3 supplemental materials

B.1 Effect of Uncertainty in the Earth's Gravitational Potential on Anomalous Redshift Measurements

Fifth force searches based on anomalous redshift measurements require a knowledge of the general relativistic contribution to the redshift to the corresponding level of accuracy. Therefore uncertainties in our knowledge of the earth's gravitational field can limit the precision of the determination of the anomalous redshift. In this respect anomalous redshift measurements differ from direct fifth force searches or differential redshift measurements, for which the effect of the uncertainties in the earth's gravitational field is small because they compare the motion of two bodies of different compositions or two different clocks at the same physical location. In the neighborhood of the earth, the gravitational potential is determined from the precisely measured orbits of many different satellites under the assumption that they are acted on only by the gravitational force. However, as emphasized throughout this paper, models which give rise to position dependence of fundamental parameters also predict a fifth force. This fifth force will affect the orbit of satellites and will therefore affect the inferred value of the gravitational potential. In this appendix, we systematically take this effect into account and show that the corrections to our formulas are small.

Anomalous redshift experiments employ a clock placed on a satellite in orbit around the earth. The frequency of this clock is measured at different locations and compared against the frequency of an identical clock on earth. The anomalous redshift $\tilde{\beta}_A$ inferred from these experiments is related to the frequency change of the clock as,

$$\frac{\Delta f}{f} = (1 + \tilde{\beta}_A)\Delta\tilde{U}_{\text{infer}} \ , \tag{B.1}$$

Here $\tilde{U}_{\text{infer}}$ is the inferred value of the difference in the gravitational potential as opposed to its actual value ΔU_{GR}. In the class of theories we are exploring, this observed change in frequency actually arises from two separate contributions, one from general relativity and the other from the location dependence of fundamental constants. Together, these read

$$\frac{\Delta f}{f} = \Delta U_{\text{GR}} + \beta_A \Delta U_{\text{GR}} \ , \tag{B.2}$$

where the first term is the difference predicted by general relativity while the second term is what was calculated in the text, see e.g. Eq. (3.27). To translate the experimental bound on $\tilde{\beta}_A$ to a constraint on β_A, we need to relate $\tilde{U}_{\text{infer}}$ to U_{GR}.

The gravitational potential is inferred from the motion of satellites. The acceleration of a satellite in the earth's gravitational field is given by,

$$a = \frac{GM}{r^2}\left(1 + \alpha_{\mathbf{E}}\alpha_{\mathbf{S}}\right) = \frac{\Delta U_{\text{infer}}}{r}, \tag{B.3}$$

where $\alpha_{\mathbf{E}}$ and $\alpha_{\mathbf{S}}$ represent the values of $\alpha_{\mathbf{X}}$ for the earth and satellite respectively, where $\alpha_{\mathbf{X}}$ is as defined in Eq. (3.4). For simplicity we have taken the mass of the ultralight scalar to be zero, since incorporating a non-zero mass for the modulus would require a detailed understanding of the orbits of the satellites employed.

Using the relationship $\Delta U_{\rm GR} = GM/r$ and Eqs. (B.1), (B.2) and (B.3), we find that

$$\tilde{\beta}_A \approx \beta_A - \alpha_{\mathbf{E}}\alpha_{\mathbf{S}}. \tag{B.4}$$

From Eq. (3.32) we have

$$\frac{\beta_A}{\alpha_{\mathbf{E}}} = \left[(K_\alpha^A + 2)d_e - K_\mu^A(d_{m_e} - d_g) + K_q^A(d_{\hat{m}} - d_g) + d_{m_e}\right] . \tag{B.5}$$

Then the inferred anomalous redshift $\tilde{\beta}_A$ is proportional to the difference

$$\tilde{\beta}_A \propto F(K_X^A, d_x) - \alpha_{\mathbf{S}} , \tag{B.6}$$

where $F(K_X^A, d_x)$ is the term on the right hand side of Eq. (B.5). From the expression for $\alpha_{\mathbf{S}}$ in Eqs. (3.4) and (3.6), we see that this difference is the sum of a term proportional to d_e, a term proportional to $(d_{m_e} - d_g)$ and a term proportional to $(d_{\hat{m}} - d_g)$. As we now explain, this is exactly as expected. Recall that experiments cannot distinguish an EP preserving dilaton from general relativity in the non-relativistic limit. Setting the couplings to their values in the dilaton limit, $d_g = d_{m_e} = d_{\hat{m}}$ and $d_e = 0$, we find that $\tilde{\beta}_A = 0$ as expected. This constitutes a powerful cross check of our results.

From Eq. (3.6) we see that the parameters $Q_{\hat{m}}$, Q_e and Q_{m_e} are all much less than one.

This allows us to approximate

$$\frac{\tilde{\beta}_A}{\alpha_{\mathbf{E}}} \approx \left[(K_\alpha^A + 2) d_e + (1 - K_\mu^A)(d_{m_e} - d_g) + K_q^A (d_{\hat{m}} - d_g) \right] . \tag{B.7}$$

Comparing the right hand sides of Eqs. (B.7) and (B.5), we see that the difference between the two is just d_g. While the actual anomalous redshift scales with d_g as $\beta_A/\alpha_{\mathbf{E}} \sim (K_\mu^A - K_q^A) d_g$, the inferred anomalous redshift scales as $\tilde{\beta}_A/\alpha_{\mathbf{E}} \sim (K_\mu^A - K_q^A - 1) d_g$. Thus the errors arising from neglecting the effect of the fifth force on the motion of the satellite are small provided that either d_g is negligible or $|K_\mu^A + K_q^A| \gg 1$. For the clocks used in the experiments we have considered, the second condition is satisfied.

Bibliography

[1] D. Antypas et al. New Horizons: Scalar and Vector Ultralight Dark Matter. 3 2022.

[2] Joel Bergé, Philippe Brax, Gilles Métris, Martin Pernot-Borràs, Pierre Touboul, and Jean-Philippe Uzan. MICROSCOPE Mission: First Constraints on the Violation of the Weak Equivalence Principle by a Light Scalar Dilaton. Phys. Rev. Lett., 120(14):141101, 2018.

[3] G. L. Smith, C. D. Hoyle, J. H. Gundlach, E. G. Adelberger, B. R. Heckel, and H. E. Swanson. Short-range tests of the equivalence principle. Phys. Rev. D, 61:022001, Dec 1999.

[4] S. Schlamminger, K.-Y. Choi, T. A. Wagner, J. H. Gundlach, and E. G. Adelberger. Test of the equivalence principle using a rotating torsion balance. Phys. Rev. Lett., 100:041101, Jan 2008.

[5] A. Hees, J. Guéna, M. Abgrall, S. Bize, and P. Wolf. Searching for an oscillating massive scalar field as a dark matter candidate using atomic hyperfine frequency comparisons. Phys. Rev. Lett., 117:061301, Aug 2016.

[6] Colin J. Kennedy, Eric Oelker, John M. Robinson, Tobias Bothwell, Dhruv Kedar, William R. Milner, G. Edward Marti, Andrei Derevianko, and Jun Ye. Precision Metrology Meets Cosmology: Improved Constraints on Ultralight Dark Matter from Atom-Cavity Frequency Comparisons. Phys. Rev. Lett., 125(20):201302, 2020.

[7] Yousef Abou El-Neaj et al. AEDGE: Atomic Experiment for Dark Matter and Gravity Exploration in Space. 2019.

[8] L. Badurina et al. AION: An Atom Interferometer Observatory and Network. 2019.

[9] Jon Coleman. Matter-wave Atomic Gradiometer InterferometricSensor (MAGIS-100) at Fermilab. PoS, ICHEP2018:021, 2019.

[10] Asimina Arvanitaki, Junwu Huang, and Ken Van Tilburg. Searching for dilaton dark matter with atomic clocks. Phys. Rev. D, 91:015015, Jan 2015.

[11] T. A. Wagner, S. Schlamminger, J. H. Gundlach, and E. G. Adelberger. Torsion-balance tests of the weak equivalence principle. Class. Quant. Grav., 29:184002, 2012.

[12] Pierre Touboul et al. MICROSCOPE Mission: First Results of a Space Test of the Equivalence Principle. Phys. Rev. Lett., 119(23):231101, 2017.

[13] V. B. Braginskii and V. I. Panov. Verification of equivalence of inertial and gravitational masses. Zh. Eksp. Teor. Fiz., 61:873–879, 1971.

[14] Yu-Dai Tsai, Joshua Eby, and Marianna S. Safronova. SpaceQ - Direct Detection of Ultralight Dark Matter with Space Quantum Sensors. 12 2021.

[15] R. Lange, N. Huntemann, J. M. Rahm, C. Sanner, H. Shao, B. Lipphardt, Chr. Tamm, S. Weyers, and E. Peik. Improved limits for violations of local position invariance from atomic clock comparisons. Phys. Rev. Lett., 126(1):011102, 2021.

[16] Andrei Derevianko, Kurt Gibble, Leo Hollberg, Nathan R. Newbury, Chris Oates, Marianna S. Safronova, Laura C. Sinclair, and Nan Yu. Fundamental Physics with a State-of-the-Art Optical Clock in Space. 12 2021.

[17] K. Abe et al. Test of Lorentz invariance with atmospheric neutrinos. Phys. Rev. D, 91(5):052003, 2015.

[18] K. Abe et al. Limits on sterile neutrino mixing using atmospheric neutrinos in Super-Kamiokande. Phys. Rev. D, 91:052019, 2015.

[19] B. Abi et al. Prospects for beyond the Standard Model physics searches at the Deep Underground Neutrino Experiment. Eur. Phys. J. C, 81(4):322, 2021.

[20] Joe Zhiyu Chen, Isabel M. Oldengott, Giovanni Pierobon, and Yvonne Y. Y. Wong. Weaker yet again: mass spectrum-consistent cosmological constraints on the neutrino lifetime. Eur. Phys. J. C, 82(7):640, 2022.

[21] Masha Baryakhtar, Robert Lasenby, and Mae Teo. Black Hole Superradiance Signatures of Ultralight Vectors. Phys. Rev. D, 96(3):035019, 2017.

[22] Mark B. Wise and Yue Zhang. Lepton Flavorful Fifth Force and Depth-dependent Neutrino Matter Interactions. JHEP, 06:053, 2018.

[23] Pilar Coloma, M. C. Gonzalez-Garcia, and Michele Maltoni. Neutrino oscillation constraints on U(1)' models: from non-standard interactions to long-range forces. JHEP, 01:114, 2021. [Erratum: JHEP 11, 115 (2022)].

[24] Jeff A. Dror. Discovering leptonic forces using nonconserved currents. Phys. Rev. D, 101(9):095013, 2020.

[25] Guo-yuan Huang, Tommy Ohlsson, and Shun Zhou. Observational Constraints on Secret Neutrino Interactions from Big Bang Nucleosynthesis. Phys. Rev. D, 97(7):075009, 2018.

[26] Stephan Schlamminger, K. Y. Choi, T. A. Wagner, J. H. Gundlach, and E. G. Adelberger. Test of the equivalence principle using a rotating torsion balance. Phys. Rev. Lett., 100:041101, 2008.

[27] Majid Ekhterachian, Anson Hook, Soubhik Kumar, and Yuhsin Tsai. Bounds on gauge bosons coupled to nonconserved currents. Phys. Rev. D, 104(3):035034, 2021.

[28] Jeff A. Dror, Ranjan Laha, and Toby Opferkuch. Probing muonic forces with neutron star binaries. Phys. Rev. D, 102(2):023005, 2020.

[29] Georges Aad et al. Observation of a new particle in the search for the Standard Model Higgs boson with the ATLAS detector at the LHC. Phys. Lett. B, 716:1–29, 2012.

[30] Serguei Chatrchyan et al. Observation of a New Boson at a Mass of 125 GeV with the CMS Experiment at the LHC. Phys. Lett. B, 716:30–61, 2012.

[31] N. Aghanim et al. Planck 2018 results. VI. Cosmological parameters. 7 2018.

[32] David J. E. Marsh. Axion Cosmology. Phys. Rept., 643:1–79, 2016.

[33] Andrei D. Linde. Inflation and Axion Cosmology. Phys. Lett., B201:437–439, 1988.

[34] Walter D. Goldberger and Mark B. Wise. Modulus stabilization with bulk fields. Phys. Rev. Lett., 83:4922–4925, 1999.

[35] Asimina Arvanitaki, Savas Dimopoulos, Sergei Dubovsky, Nemanja Kaloper, and John March-Russell. String Axiverse. Phys. Rev. D, 81:123530, 2010.

[36] Zackaria Chacko and Rashmish K. Mishra. Effective Theory of a Light Dilaton. Phys. Rev. D, 87(11):115006, 2013.

[37] Francesco Coradeschi, Paolo Lodone, Duccio Pappadopulo, Riccardo Rattazzi, and Lorenzo Vitale. A naturally light dilaton. JHEP, 11:057, 2013.

[38] Gordon Kane, Kuver Sinha, and Scott Watson. Cosmological Moduli and the Post-Inflationary Universe: A Critical Review. Int. J. Mod. Phys. D, 24(08):1530022, 2015.

[39] Thibault Damour and John F. Donoghue. Equivalence principle violations and couplings of a light dilaton. Phys. Rev. D, 82:084033, Oct 2010.

[40] Thibault Damour and John F. Donoghue. Phenomenology of the Equivalence Principle with Light Scalars. Class. Quant. Grav., 27:202001, 2010.

[41] Dawid Brzeminski, Zackaria Chacko, Abhish Dev, and Anson Hook. Time-varying fine structure constant from naturally ultralight dark matter. Phys. Rev. D, 104(7):075019, 2021.

[42] Thibault Damour. Theoretical Aspects of the Equivalence Principle. Class. Quant. Grav., 29:184001, 2012.

[43] Andrei Khmelnitsky and Valery Rubakov. Pulsar timing signal from ultralight scalar dark matter. JCAP, 02:019, 2014.

[44] Y.V. Stadnik and V.V. Flambaum. Searching for dark matter and variation of fundamental constants with laser and maser interferometry. Phys. Rev. Lett., 114:161301, 2015.

[45] Asimina Arvanitaki, Junwu Huang, and Ken Van Tilburg. Searching for dilaton dark matter with atomic clocks. Phys. Rev. D, 91(1):015015, 2015.

[46] Asimina Arvanitaki, Savas Dimopoulos, and Ken Van Tilburg. Sound of Dark Matter: Searching for Light Scalars with Resonant-Mass Detectors. Phys. Rev. Lett., 116(3):031102, 2016.

[47] Peter W. Graham, Igor G. Irastorza, Steven K. Lamoreaux, Axel Lindner, and Karl A. van Bibber. Experimental Searches for the Axion and Axion-Like Particles. Ann. Rev. Nucl. Part. Sci., 65:485–514, 2015.

[48] Peter W. Graham, David E. Kaplan, Jeremy Mardon, Surjeet Rajendran, and William A. Terrano. Dark Matter Direct Detection with Accelerometers. Phys. Rev. D, 93(7):075029, 2016.

[49] Y.V. Stadnik and V.V. Flambaum. Enhanced effects of variation of the fundamental constants in laser interferometers and application to dark matter detection. Phys. Rev. A, 93(6):063630, 2016.

[50] Cédric Delaunay, Roee Ozeri, Gilad Perez, and Yotam Soreq. Probing Atomic Higgs-like Forces at the Precision Frontier. Phys. Rev. D, 96(9):093001, 2017.

[51] Asher Berlin. Neutrino Oscillations as a Probe of Light Scalar Dark Matter. Phys. Rev. Lett., 117(23):231801, 2016.

[52] Andrew A. Geraci and Andrei Derevianko. Sensitivity of atom interferometry to ultralight scalar field dark matter. Phys. Rev. Lett., 117(26):261301, 2016.

[53] Gordan Krnjaic, Pedro A.N. Machado, and Lina Necib. Distorted neutrino oscillations from time varying cosmic fields. Phys. Rev. D, 97(7):075017, 2018.

[54] Benjamin M. Roberts, Geoffrey Blewitt, Conner Dailey, Mac Murphy, Maxim Pospelov, Alex Rollings, Jeff Sherman, Wyatt Williams, and Andrei Derevianko. Search for domain wall dark matter with atomic clocks on board global positioning system satellites. Nature Commun., 8(1):1195, 2017.

[55] Asimina Arvanitaki, Savas Dimopoulos, and Ken Van Tilburg. Resonant absorption of bosonic dark matter in molecules. Phys. Rev. X, 8(4):041001, 2018.

[56] William DeRocco and Anson Hook. Axion interferometry. Phys. Rev. D, 98(3):035021, 2018.

[57] Andrew A. Geraci, Colin Bradley, Dongfeng Gao, Jonathan Weinstein, and Andrei Derevianko. Searching for Ultralight Dark Matter with Optical Cavities. Phys. Rev. Lett., 123(3):031304, 2019.

[58] Igor G. Irastorza and Javier Redondo. New experimental approaches in the search for axion-like particles. Prog. Part. Nucl. Phys., 102:89–159, 2018.

[59] Daniel Carney, Anson Hook, Zhen Liu, Jacob M. Taylor, and Yue Zhao. Ultralight Dark Matter Detection with Mechanical Quantum Sensors. 8 2019.

[60] Huai-Ke Guo, Keith Riles, Feng-Wei Yang, and Yue Zhao. Searching for Dark Photon Dark Matter in LIGO O1 Data. Commun. Phys., 2:155, 2019.

[61] H. Grote and Y.V. Stadnik. Novel signatures of dark matter in laser-interferometric gravitational-wave detectors. Phys. Rev. Res., 1(3):033187, 2019.

[62] Abhish Dev, Pedro A.N. Machado, and Pablo Martínez-Miravé. Signatures of Ultralight Dark Matter in Neutrino Oscillation Experiments. 7 2020.

[63] Yevgeny V. Stadnik. New bounds on macroscopic scalar-field topological defects from non-transient signatures due to environmental dependence and spatial variations of the fundamental constants. Phys. Rev. D, 102:115016, 2020.

[64] Y. V. Stadnik and V. V. Flambaum. Enhanced effects of variation of the fundamental constants in laser interferometers and application to dark-matter detection. Phys. Rev. A, 93:063630, Jun 2016.

[65] Matías M. Reynoso and Oscar A. Sampayo. Propagation of high-energy neutrinos in a background of ultralight scalar dark matter. Astropart. Phys., 82:10–20, 2016.

[66] Vedran Brdar, Joachim Kopp, Jia Liu, Pascal Prass, and Xiao-Ping Wang. Fuzzy dark matter and nonstandard neutrino interactions. Phys. Rev. D, 97(4):043001, 2018.

[67] Hooman Davoudiasl, Gopolang Mohlabeng, and Matthew Sullivan. Galactic Dark Matter Population as the Source of Neutrino Masses. Phys. Rev. D, 98(2):021301, 2018.

[68] Jiajun Liao, Danny Marfatia, and Kerry Whisnant. Light scalar dark matter at neutrino oscillation experiments. JHEP, 04:136, 2018.

[69] Francesco Capozzi, Ian M. Shoemaker, and Luca Vecchi. Neutrino Oscillations in Dark Backgrounds. JCAP, 07:004, 2018.

[70] Guo-Yuan Huang and Newton Nath. Neutrinophilic Axion-Like Dark Matter. Eur. Phys. J. C, 78(11):922, 2018.

[71] Yasaman Farzan. Ultra-light scalar saving the 3 + 1 neutrino scheme from the cosmological bounds. Phys. Lett. B, 797:134911, 2019.

[72] James M. Cline. Viable secret neutrino interactions with ultralight dark matter. Phys. Lett. B, 802:135182, 2020.

[73] Marta Losada, Yosef Nir, Gilad Perez, and Yogev Shpilman. Probing scalar dark matter oscillations with neutrino oscillations. JHEP, 04:030, 2022.

[74] Guo-yuan Huang and Newton Nath. Neutrino meets ultralight dark matter: $0\nu\beta\beta$ decay and cosmology. JCAP, 05(05):034, 2022.

[75] Eung Jin Chun. Neutrino Transition in Dark Matter. 12 2021.

[76] Marta Losada, Yosef Nir, Gilad Perez, Inbar Savoray, and Yogev Shpilman. Parametric resonance in neutrino oscillations induced by ultra-light dark matter and implications for KamLAND and JUNO. 5 2022.

[77] Abhish Dev, Gordan Krnjaic, Pedro Machado, and Harikrishnan Ramani. Constraining Feeble Neutrino Interactions with Ultralight Dark Matter. 5 2022.

[78] E. G. Adelberger, J. H. Gundlach, B. R. Heckel, S. Hoedl, and S. Schlamminger. Torsion balance experiments: A low-energy frontier of particle physics. Prog. Part. Nucl. Phys., 62:102–134, 2009.

[79] J. O. Dickey et al. Lunar Laser Ranging: A Continuing Legacy of the Apollo Program. Science, 265:482–490, 1994.

[80] James G. Williams, Slava G. Turyshev, and Dale H. Boggs. Progress in lunar laser ranging tests of relativistic gravity. Phys. Rev. Lett., 93:261101, 2004.

[81] S. M. Ransom et al. A millisecond pulsar in a stellar triple system. Nature, 505:520, 2014.

[82] Anne M. Archibald, Nina V. Gusinskaia, Jason W. T. Hessels, Adam T. Deller, David L. Kaplan, Duncan R. Lorimer, Ryan S. Lynch, Scott M. Ransom, and Ingrid H. Stairs. Universality of free fall from the orbital motion of a pulsar in a stellar triple system. Nature, 559(7712):73–76, 2018.

[83] Sebastian Fray, Cristina Alvarez Diez, Theodor W. Hansch, and Martin Weitz. Atomic interferometer with amplitude gratings of light and its applications to atom based tests of the equivalence principle. Phys. Rev. Lett., 93:240404, 2004.

[84] Lin Zhou et al. Test of Equivalence Principle at 10^{-8} Level by a Dual-species Double-diffraction Raman Atom Interferometer. Phys. Rev. Lett., 115(1):013004, 2015.

[85] Lin Zhou et al. Joint mass-and-energy test of the equivalence principle at the 10^{-10} level using atoms with specified mass and internal energy. Phys. Rev. A, 104(2):022822, 2021.

[86] Dennis Schlippert, Jonas Hartwig, Henning Albers, Logan L. Richardson, Christian Schubert, Albert Roura, Wolfgang P. Schleich, Wolfgang Ertmer, and Ernst M. Rasel. Quantum Test of the Universality of Free Fall. Phys. Rev. Lett., 112:203002, 2014.

[87] M. G. Tarallo, T. Mazzoni, N. Poli, D. V. Sutyrin, X. Zhang, and G. M. Tino. Test of Einstein Equivalence Principle for 0-spin and half-integer-spin atoms: Search for spin-gravity coupling effects. Phys. Rev. Lett., 113:023005, 2014.

[88] Dawid Brzeminski, Zackaria Chacko, Abhish Dev, Ina Flood, and Anson Hook. Searching for a fifth force with atomic and nuclear clocks. Phys. Rev. D, 106(9):095031, 2022.

[89] Ann E. Nelson and Jakub Scholtz. Dark Light, Dark Matter and the Misalignment Mechanism. Phys. Rev. D, 84:103501, 2011.

[90] Peter W. Graham, Jeremy Mardon, and Surjeet Rajendran. Vector Dark Matter from Inflationary Fluctuations. Phys. Rev. D, 93(10):103520, 2016.

[91] Prateek Agrawal, Naoya Kitajima, Matthew Reece, Toyokazu Sekiguchi, and Fuminobu Takahashi. Relic Abundance of Dark Photon Dark Matter. Phys. Lett. B, 801:135136, 2020.

[92] Aaron Pierce, Keith Riles, and Yue Zhao. Searching for Dark Photon Dark Matter with Gravitational Wave Detectors. Phys. Rev. Lett., 121(6):061102, 2018.

[93] Marco Fabbrichesi, Emidio Gabrielli, and Gaia Lanfranchi. The Dark Photon. 5 2020.

[94] Dawid Brzeminski, Saurav Das, Anson Hook, and Clayton Ristow. Constraining Vector Dark Matter with neutrino experiments. JHEP, 08:181, 2023.

[95] Anson Hook. Solving the hierarchy problem discretely. Phys. Rev. Lett., 120:261802, Jun 2018.

[96] Asimina Arvanitaki, Peter W. Graham, Jason M. Hogan, Surjeet Rajendran, and Ken Van Tilburg. Search for light scalar dark matter with atomic gravitational wave detectors. Phys. Rev. D, 97:075020, Apr 2018.

[97] Ken Van Tilburg, Nathan Leefer, Lykourgos Bougas, and Dmitry Budker. Search for ultralight scalar dark matter with atomic spectroscopy. Phys. Rev. Lett., 115:011802, Jun 2015.

[98] L. Baggio, M. Bignotto, M. Bonaldi, M. Cerdonio, L. Conti, P. Falferi, N. Liguori, A. Marin, R. Mezzena, A. Ortolan, S. Poggi, G. A. Prodi, F. Salemi, G. Soranzo, L. Taffarello, G. Vedovato, A. Vinante, S. Vitale, and J. P. Zendri. 3-mode detection for widening the bandwidth of resonant gravitational wave detectors. Phys. Rev. Lett., 94:241101, Jun 2005.

[99] Sander M. Vermeulen et al. Direct limits for scalar field dark matter from a gravitational-wave detector. 3 2021.

[100] P G Thirolf, B Seiferle, and L von der Wense. The 229-thorium isomer: doorway to the road from the atomic clock to the nuclear clock. Journal of Physics B: Atomic, Molecular and Optical Physics, 52(20):203001, sep 2019.

[101] Y.V. Stadnik and V.V. Flambaum. Can dark matter induce cosmological evolution of the fundamental constants of Nature? Phys. Rev. Lett., 115(20):201301, 2015.

[102] Sergey Sibiryakov, Philip Sorensen, and Tien-Tien Yu. BBN constraints on universally-coupled ultralight scalar dark matter. 6 2020.

[103] D. H. Lyth. Axions and inflation: Vacuum fluctuations. Phys. Rev. D, 45:3394–3404, May 1992.

[104] Asimina Arvanitaki, Savas Dimopoulos, Marios Galanis, Luis Lehner, Jedidiah O. Thompson, and Ken Van Tilburg. Large-misalignment mechanism for the formation of compact axion structures: Signatures from the QCD axion to fuzzy dark matter. Phys. Rev. D, 101(8):083014, 2020.

[105] Asimina Arvanitaki, Savas Dimopoulos, Marios Galanis, Luis Lehner, Jedidiah O. Thompson, and Ken Van Tilburg. Large-misalignment mechanism for the formation of compact axion structures: Signatures from the QCD axion to fuzzy dark matter. Phys. Rev. D, 101(8):083014, 2020.

[106] Junwu Huang, Amalia Madden, Davide Racco, and Mario Reig. Maximal axion misalignment from a minimal model. 6 2020.

[107] Luca Visinelli and Paolo Gondolo. Dark Matter Axions Revisited. Phys. Rev. D, 80:035024, 2009.

[108] Andrew D. Ludlow, Martin M. Boyd, Jun Ye, E. Peik, and P. O. Schmidt. Optical atomic clocks. Rev. Mod. Phys., 87:637–701, Jun 2015.

[109] W. F. McGrew et al. Atomic clock performance enabling geodesy below the centimetre level. Nature, 564(7734):87–90, 2018.

[110] G. Edward Marti, Ross B. Hutson, Akihisa Goban, Sara L. Campbell, Nicola Poli, and Jun Ye. Imaging optical frequencies with $100\ \mu\mathrm{Hz}$ precision and $1.1\ \mu\mathrm{m}$ resolution. Phys. Rev. Lett., 120:103201, Mar 2018.

[111] Tobias Bothwell, Dhruv Kedar, Eric Oelker, John M Robinson, Sarah L Bromley, Weston L Tew, Jun Ye, and Colin J Kennedy. JILA SrI optical lattice clock with uncertainty of 2.0×10^{-18}. Metrologia, 56(6):065004, oct 2019.

[112] M. S. Safronova, D. Budker, D. DeMille, Derek F. Jackson Kimball, A. Derevianko, and C. W. Clark. Search for New Physics with Atoms and Molecules. Rev. Mod. Phys., 90(2):025008, 2018.

[113] V. V. Flambaum and E. V. Shuryak. How changing physical constants and violation of local position invariance may occur? AIP Conf. Proc., 995(1):1–11, 2008.

[114] Douglas J. Shaw. Detecting seasonal changes in the fundamental constants. 2 2007.

[115] John D. Barrow and Douglas J. Shaw. Varying Alpha: New Constraints from Seasonal Variations. Phys. Rev. D, 78:067304, 2008.

[116] Thomas Dent. Eotvos bounds on couplings of fundamental parameters to gravity. Phys. Rev. Lett., 101:041102, 2008.

[117] Jean-Philippe Uzan. Varying Constants, Gravitation and Cosmology. Living Rev. Rel., 14:2, 2011.

[118] Justin Khoury and Amanda Weltman. Chameleon fields: Awaiting surprises for tests of gravity in space. Phys. Rev. Lett., 93:171104, 2004.

[119] Justin Khoury and Amanda Weltman. Chameleon cosmology. Phys. Rev. D, 69:044026, 2004.

[120] Baruch Feldman and Ann E. Nelson. New regions for a chameleon to hide. JHEP, 08:002, 2006.

[121] David F. Mota and Douglas J. Shaw. Strongly coupled chameleon fields: New horizons in scalar field theory. Phys. Rev. Lett., 97:151102, 2006.

[122] Philippe Brax, Clare Burrage, and Anne-Christine Davis. Laboratory constraints. Int. J. Mod. Phys. D, 27(15):1848009, 2018.

[123] Jeremy Sakstein. Astrophysical tests of screened modified gravity. Int. J. Mod. Phys. D, 27(15):1848008, 2018.

[124] Nikita Blinov, Sebastian A.R. Ellis, and Anson Hook. Consequences of Fine-Tuning for Fifth Force Searches. JHEP, 11:029, 2018.

[125] R. F. C. Vessot and M. W. Levine. A test of the equivalence principle using a space-borne clock. General Relativity and Gravitation, 10:181204, 1979.

[126] P. Delva et al. Gravitational Redshift Test Using Eccentric Galileo Satellites. Phys. Rev. Lett., 121(23):231101, 2018.

[127] Vladimir Schkolnik et al. Optical Atomic Clock aboard an Earth-orbiting Space Station (OACESS): Enhancing searches for physics beyond the standard model in space. 4 2022.

[128] E. G. Adelberger, Blayne R. Heckel, and A. E. Nelson. Tests of the gravitational inverse square law. Ann. Rev. Nucl. Part. Sci., 53:77–121, 2003.

[129] N. Leefer, C. T. M. Weber, A. Cingöz, J. R. Torgerson, and D. Budker. New limits on variation of the fine-structure constant using atomic dysprosium. Phys. Rev. Lett., 111:060801, Aug 2013.

[130] N. Leefer, A. Gerhardus, D. Budker, V. V. Flambaum, and Y. V. Stadnik. Search for the effect of massive bodies on atomic spectra and constraints on Yukawa-type interactions of scalar particles. Phys. Rev. Lett., 117(27):271601, 2016.

[131] E. Peik, T. Schumm, M. S. Safronova, A. Pálffy, J. Weitenberg, and P. G. Thirolf. Nuclear clocks for testing fundamental physics. Quantum Sci. Technol., 6(3):034002, 2021.

[132] V. V. Flambaum and V. A. Dzuba. Search for variation of the fundamental constants in atomic, molecular and nuclear spectra. Can. J. Phys., 87:25–33, 2009.

[133] L. Wolfenstein. Neutrino Oscillations in Matter. Phys. Rev. D, 17:2369–2374, 1978.

[134] S. P. Mikheyev and A. Yu. Smirnov. Resonance Amplification of Oscillations in Matter and Spectroscopy of Solar Neutrinos. Sov. J. Nucl. Phys., 42:913–917, 1985.

[135] K. Abe et al. Atmospheric neutrino oscillation analysis with external constraints in Super-Kamiokande I-IV. Phys. Rev. D, 97(7):072001, 2018.

[136] Gonzalo Alonso-Álvarez and James M. Cline. Sterile neutrino dark matter catalyzed by a very light dark photon. JCAP, 10:041, 2021.

[137] R. Acciarri et al. Long-Baseline Neutrino Facility (LBNF) and Deep Underground Neutrino Experiment (DUNE): Conceptual Design Report, Volume 2: The Physics Program for DUNE at LBNF. 12 2015.

[138] B. Abi et al. Long-baseline neutrino oscillation physics potential of the DUNE experiment. Eur. Phys. J. C, 80(10):978, 2020.

[139] M. G. Aartsen et al. Measurement of Atmospheric Neutrino Oscillations at 6–56 GeV with IceCube DeepCore. Phys. Rev. Lett., 120(7):071801, 2018.

[140] M. G. Aartsen et al. Search for Nonstandard Neutrino Interactions with IceCube DeepCore. Phys. Rev. D, 97(7):072009, 2018.

[141] K. Abe et al. The Hyper-Kamiokande Experiment - Snowmass LOI. 9 2020.

[142] M. Honda, T. Kajita, K. Kasahara, and S. Midorikawa. Improvement of low energy atmospheric neutrino flux calculation using the JAM nuclear interaction model. Phys. Rev. D, 83:123001, 2011.

[143] A. M. Dziewonski and D. L. Anderson. Preliminary reference earth model. Phys. Earth Planet. Interiors, 25:297–356, 1981.

[144] Patrick Huber, M. Lindner, and W. Winter. Simulation of long-baseline neutrino oscillation experiments with GLoBES (General Long Baseline Experiment Simulator). Comput. Phys. Commun., 167:195, 2005.

[145] Patrick Huber, Joachim Kopp, Manfred Lindner, Mark Rolinec, and Walter Winter. New features in the simulation of neutrino oscillation experiments with GLoBES 3.0: General Long Baseline Experiment Simulator. Comput. Phys. Commun., 177:432–438, 2007.

[146] Ivan Esteban, M. C. Gonzalez-Garcia, Alvaro Hernandez-Cabezudo, Michele Maltoni, and Thomas Schwetz. Global analysis of three-flavour neutrino oscillations: synergies and tensions in the determination of θ_{23}, δ_{CP}, and the mass ordering. JHEP, 01:106, 2019.

[147] Mikko Laine and Aleksi Vuorinen. Basics of Thermal Field Theory, volume 925. Springer, 2016.

[148] J.I. Kapusta and Charles Gale. Finite-temperature field theory: Principles and applications. Cambridge Monographs on Mathematical Physics. Cambridge University Press, 2011.

[149] Peter Arnold and Chengxing Zhai. Three-loop free energy for pure gauge qcd. Phys. Rev. D, 50:7603–7623, Dec 1994.

[150] Peter Arnold and Chengxing Zhai. Three-loop free energy for high-temperature qed and qcd with fermions. Phys. Rev. D, 51:1906–1918, Feb 1995.